

MICROCOPY RESOLUTION TEST CHART  
NATIONAL BUREAU OF STANDARDS-1963-A

①

# NAVAL POSTGRADUATE SCHOOL Monterey, California



AD-A161 500

DTIC  
SEL  
NOV 27 1985

## THESIS

EFFECTS OF WAVEGUIDE MODES ON THE  
SCATTERING OF A FINITE TUBULAR CYLINDER

by

Gyoo Pil Chung

September 1985

Thesis Advisor:

Hung-Mon Lee

Approved for public release; distribution is unlimited

DTIC FILE COPY

86 11 13 056

REPORT DOCUMENTATION PAGE		READ INSTRUCTIONS BEFORE COMPLETING FORM
1. REPORT NUMBER	2. GOVT ACCESSION NO. <b>AD-A161500</b>	3. RECIPIENT'S CATALOG NUMBER
4. TITLE (and Subtitle) Effects of Waveguide Modes on the Scattering of a Finite Tubular Cylinder		5. TYPE OF REPORT & PERIOD COVERED Master's Thesis; September 1985
7. AUTHOR(s) Gyoo Pil Chung		6. PERFORMING ORG. REPORT NUMBER
9. PERFORMING ORGANIZATION NAME AND ADDRESS Naval Postgraduate School Monterey, California 93943-5100		8. CONTRACT OR GRANT NUMBER(s)
11. CONTROLLING OFFICE NAME AND ADDRESS Naval Postgraduate School Monterey, California 93943-5100		10. PROGRAM ELEMENT, PROJECT, TASK AREA & WORK UNIT NUMBERS
14. MONITORING AGENCY NAME & ADDRESS (if different from Controlling Office)		12. REPORT DATE September 1985
		13. NUMBER OF PAGES 100
		15. SECURITY CLASS. (of this report) UNCLASSIFIED
		15a. DECLASSIFICATION/DOWNGRADING SCHEDULE
16. DISTRIBUTION STATEMENT (of this Report) Approved for public release; distribution is unlimited.		
17. DISTRIBUTION STATEMENT (of the abstract entered in Block 20, if different from Report)		
18. SUPPLEMENTARY NOTES		
19. KEY WORDS (Continue on reverse side if necessary and identify by block number) Electromagnetic Scattering; Waveguide Mode; Finite Tubular Cylinder; Backscattering Cross Section. <i>f</i>		
20. ABSTRACT (Continue on reverse side if necessary and identify by block number) This thesis is a study of the back scattering of finite tubular cylinders with circular cross-sections and very thin conducting walls. Measurements of several scaled tubular cylinders were taken and the experimental results were compared to theoretical data and to previous results, respectively. This research is part of an ongoing project to investigate the resonant scattering characteristics of targets. The results are expected to find applications in target identification.		

Approved for public release; distribution is unlimited.

Effects of Waveguide Modes on The Scattering of A  
Finite Tubular Cylinder

by

Gyoo Pil Chung  
Lieutenant, R.O.C. Navy  
R.S., Republic of Korea, Naval Academy, 1980

Submitted in partial fulfillment of the  
requirements for the degree of

MASTER OF SCIENCE IN ELECTRICAL ENGINEERING

from the

NAVAL POSTGRADUATE SCHOOL  
September 1985

Author:

*Gyoo Pil Chung*

GYOO PIL CHUNG

Approved by:

*Hung-Inou Lee*

HUNG-INOUEE, THESIS ADVISOR

*M. S. Wang*

M. S. WANG, SECOND READER

Director of Studies, Center for  
Department of Electrical and Computer Engineering

*John D. ...*

John D. ...  
Dean of Science and Engineering

## ABSTRACT

This thesis is a study of the back scattering of finite tubular cylinders with circular cross-sections and very thin conducting walls. Measurements of several scaled tubular cylinders were taken and the experimental results were compared to theoretical data and to previous results, respectively.

This research is part of an ongoing project to investigate the resonant scattering characteristics of targets. The results are expected to find applications in target identification.

Accession For		
NTIS	CRA&I	<input checked="" type="checkbox"/>
DTIC	AD	<input type="checkbox"/>
DA	ASD	<input type="checkbox"/>
By		
Project		
Date		
At		
AI		



## TABLE OF CONTENTS

I.	INTRODUCTION . . . . .	9
	A. RADAR AND TARGET IDENTIFICATION . . . . .	9
	B. PURPOSE OF THE THESIS . . . . .	12
II.	SYSTEM IMPROVEMENTS AND EXPERIMENTAL MEASUREMENTS . . . . .	16
	A. SYSTEM IMPROVEMENT . . . . .	18
	B. THE TARGET . . . . .	22
	C. THE ANECHOIC CHAMBER AND THE TARGET SUPPORT . . . . .	24
	D. MEASURED DATA . . . . .	24
III.	ANALYSIS OF EXPERIMENTAL DATA . . . . .	58
	A. THEORETICAL BACKGROUND . . . . .	58
	B. COMPARISON BETWEEN THEORY AND EXPERIMENT . . . . .	61
	C. COMPARISON BETWEEN NEW AND PREVIOUS RESULTS . . . . .	66
IV.	EFFECTS OF COUPLING BETWEEN THE TARGET AND ITS SUPPORT . . . . .	74
	A. RAPID SPECTRAL DOMAIN FLUCTUATIONS IN THE BROADSIDE DATA . . . . .	74
	E. MEASURED RESULTS WITH VARIOUS SUPPORTS . . . . .	75
	C. CONCLUSIONS . . . . .	97
V.	CONCLUSIONS . . . . .	98
	LIST OF REFERENCES . . . . .	99
	INITIAL DISTRIBUTION LIST . . . . .	100

LIST OF TABLES

I	LIST OF EQUIPMENT . . . . .	19
II	SIGNAL FLOW SYMBOLS FOR FIGURE 2.2 . . . . .	21
III	TARGET SPECIFICATION . . . . .	22
IV	PHYSICAL PARAMETERS OF THE CYLINDERS . . . . .	67
V	INDEX TO PLOTTED DATA FROM THE USE OF DIFFERENT TARGET SUPPORT . . . . .	75

## LIST OF FIGURES

1.1	Target Scattering Configuration . . . . .	13
2.1	IF Frequency Conversion Process . . . . .	17
2.2	Block Diagram of System . . . . .	20
2.3	Target Geometry . . . . .	23
2.4	Chamber and Target Orientations . . . . .	25
2.5	Head-on Cross Section of Cylinder 1 . . . . .	26
2.6	Head-on Cross Section of Cylinder 2 . . . . .	27
2.7	Head-on Cross Section of Cylinder 3 . . . . .	28
2.8	Head-on Cross Section of Cylinder 4 . . . . .	29
2.9	Head-on Cross Section of Cylinder 5 . . . . .	30
2.10	Head-on Cross Section of Cylinder 6 . . . . .	31
2.11	Head-on Cross Section of Cylinder 7 . . . . .	32
2.12	Head-on Cross Section of Cylinder 8 . . . . .	33
2.13	Head-on Phase Shift of Cylinder 1 . . . . .	34
2.14	Head-on Phase Shift of Cylinder 2 . . . . .	35
2.15	Head-on Phase Shift of Cylinder 3 . . . . .	36
2.16	Head-on Phase Shift of Cylinder 4 . . . . .	37
2.17	Head-on Phase Shift of Cylinder 5 . . . . .	38
2.18	Head-on Phase Shift of Cylinder 6 . . . . .	39
2.19	Head-on Phase Shift of Cylinder 7 . . . . .	40
2.20	Head-on Phase Shift of Cylinder 8 . . . . .	41
2.21	Broadside Cross Section of Cylinder 1 . . . . .	42
2.22	Broadside Cross Section of Cylinder 2 . . . . .	43
2.23	Broadside Cross Section of Cylinder 3 . . . . .	44
2.24	Broadside Cross Section of Cylinder 4 . . . . .	45
2.25	Broadside Cross Section of Cylinder 5 . . . . .	46
2.26	Broadside Cross Section of Cylinder 6 . . . . .	47
2.27	Broadside Cross Section of Cylinder 7 . . . . .	48

2.28	Broadside Cross Section of Cylinder 8 . . . . .	49
2.29	Broadside Phase Shift of Cylinder 1 . . . . .	50
2.30	Broadside Phase Shift of Cylinder 2 . . . . .	51
2.31	Broadside Phase Shift of Cylinder 3 . . . . .	52
2.32	Broadside Phase Shift of Cylinder 4 . . . . .	53
2.33	Broadside Phase Shift of Cylinder 5 . . . . .	54
2.34	Broadside Phase Shift of Cylinder 6 . . . . .	55
2.35	Broadside Phase Shift of Cylinder 7 . . . . .	56
2.36	Broadside Phase Shift of Cylinder 8 . . . . .	57
3.1	Theoretical and Measured Head-on Cross Section ( $h/a^- = 6$ ) . . . . .	62
3.2	Theoretical and Measured Head-on Phase ( $h/a^- = 6$ ) . . . . .	63
3.3	Theoretical and Measured Head-on Cross Section ( $h/a^- = 4$ ) . . . . .	64
3.4	Theoretical and Measured Head-on Phase ( $h/a^- = 4$ ) . . . . .	65
3.5	Geometry of The Problem . . . . .	68
3.6	Head-on Cross Section and The $H_m$ Cutoff Frequency, Old Results ( $h/a^+ = 4$ ) . . . . .	70
3.7	Head-on Cross Section and The $H_m$ Cutoff Frequency, Old Results ( $h/a^+ = 6$ ) . . . . .	71
3.8	Head-on Cross Section and The $H_m$ Cutoff Frequency, New Results ( $h/a^- = 4$ ) . . . . .	72
3.9	Head-on Cross Section and The $H_m$ Cutoff Frequency, New Results ( $h/a^- = 6$ ) . . . . .	73
4.1	Various Types of Support . . . . .	76
4.2	Measured Broadside Cross Section ( $h/a^- = 6$ ) . . . . .	77
4.3	Measured Broadside Cross Section ( $h/a^- = 6$ ) . . . . .	78
4.4	Measured Broadside Cross Section ( $h/a^- = 6$ ) . . . . .	79
4.5	Measured Broadside Cross Section ( $h/a^- = 6$ ) . . . . .	80
4.6	Measured Broadside Cross Section ( $h/a^- = 6$ ) . . . . .	81
4.7	Measured Broadside Phase Shift ( $h/a^- = 6$ ) . . . . .	82
4.8	Measured Broadside Phase Shift ( $h/a^- = 6$ ) . . . . .	83
4.9	Measured Broadside Phase Shift ( $h/a^- = 6$ ) . . . . .	84

4.10	Measured Broadside Phase Shift ( $h/a^- = 6$ ) . . . . .	85
4.11	Measured Broadside Phase Shift ( $h/a^- = 6$ ) . . . . .	86
4.12	Measured Broadside Cross Section ( $h/a^- = 4$ ) . . . . .	87
4.13	Measured Broadside Cross Section ( $h/a^- = 4$ ) . . . . .	88
4.14	Measured Broadside Cross Section ( $h/a^- = 4$ ) . . . . .	89
4.15	Measured Broadside Cross Section ( $h/a^- = 4$ ) . . . . .	90
4.16	Measured Broadside Cross Section ( $h/a^- = 4$ ) . . . . .	91
4.17	Measured Broadside Phase Shift ( $h/a^- = 4$ ) . . . . .	92
4.18	Measured Broadside Phase Shift ( $h/a^- = 4$ ) . . . . .	93
4.19	Measured Broadside Phase Shift ( $h/a^- = 4$ ) . . . . .	94
4.20	Measured Broadside Phase Shift ( $h/a^- = 4$ ) . . . . .	95
4.21	Measured Broadside Phase Shift ( $h/a^- = 4$ ) . . . . .	96

## I. INTRODUCTION

### A. RADAR AND TARGET IDENTIFICATION

A radar radiates electromagnetic waves into all directions in space and then listens to the echoes. If an echo is stronger than a pre-set level, the radar announces the presence of a target. A radar, as an active sensor, estimate the target's angular location from the direction its antenna is pointing; can estimate the target distance from the arrival time of the echo; deduce the target's radial velocity from the doppler phase shift of the echo signal and specify if a target is electrically large or small from the strength of the received echo signal. These are the items of information that a search radar derives from the echo. Because of the confusion often associated with it, it should be pointed out that the capability of specifying the electrical size of a target is not generally equivalent to one of specifying the physical size. This can be understood from the following analogy with the naturally equipped human electromagnetic sensor: the eyes. Ignoring the effect of thermal expansion, a light bulb is of identical physical size whether it is on or off; but it is certainly much brighter, i.e., sending the eyes a much stronger signal when it is on than when it is off.

Radars serve to complement human eyes. They extend human senses from the visible frequencies in the HF, microwave, millimeter wave and infrared regions. Even though human senses are extended, considering the amount of information the eyes derive from signals they receive, it is astonishing to realize how little information the current search radar systems are providing. Specifically, target identification

is one desirable capability current search radar sets are lacking. Since search radars are operated exclusively in the microwave frequency and HF regions, only these frequencies will be considered in the following discussions.

Human intelligence makes use of information provided by the eyes to identify objects. Identification of an object is achieved mainly through the recognition of its shape and its color. To provide information about the shape of a target, the eye, as a sensor, must be able to resolve the outlines of the object. The engravings on a coin can easily be resolved at a short distance; the structure with which the atoms build up the coin can not be resolved. The fact that the atomic spacing is smaller than the wavelength of the visible light defies any attempt to resolve the crystalline structure of the coin by a naked eye. The fact that the engravings come with contrasting areas much larger than the visible wavelength renders them easily resolved. Besides this fundamental requirement on the resolution of the outline of an object, a further problem is encountered when the object is moved farther away: In accordance to the Rayleigh's criterion, (see for example the Feynman Lectures on Physics, Vol.I, p.30-6) the engravings can not be resolved when the contrasting areas extend an angle smaller than can be afforded by the resolving power of the eyes as determined from the wavelength involved and the aperture of the pupils. To provide information about the colors of the target, the eye is capable of sensing electromagnetic waves of frequencies ranging over an octave band from approximately 390,000 to 790,000 GHz, extending from red to violet. Thus when copper and brass are shining most intensely at two different frequencies in the visible region separable by the the eye, human beings are able to tell copper from brass.

Since the targets of interest to radar have contrasting areas of linear dimensions on the order of ten meters, the

wavelength required to gain resolution of their outlines is of the order of one centimeter or below, which is close to the millimeter wave region. At these frequencies, it is difficult to achieve such long ranges as are desirable in search radars. A practical system may use a three centimeter wavelength. Assume only horizontal outlines of targets one hundred kilometers away having contrasting areas of one square meter are to be resolved. To satisfy Rayleigh's criterion, a land-based system will employ an array of antennas dispersed over a ground area more than three kilometers in diameter to defend against targets approaching in different directions. Such a huge structure would be difficult, if not impossible, to be assembled on a moving platform. A synthesized aperture would not provide the kind of instant response desired.

Identifying a target according to its color appears less formidable. The color of an object is determined by its response to waves of different frequencies. In HF and microwave frequencies, different targets respond differently at one frequency. In terms of the observed echo signals, different colors appear as echos of different shapes and strengths on the radar screen. The requirement on the radar is clear: it has to be operated over a broad bandwidth so that there are enough differences in target responses that all targets of interest can be resolved. Bandwidth of existing search radar sets seldom achieve 20% of their carrier frequencies even when chirp waveforms are utilized. Expansion of this bandwidth appears to not be a major problem considering the progress in the development of multi-octave band devices with thrusts coming mainly from the electronic warfare area. It is still an unanswered question concerning the choice of the width and the location of the desired frequency band. Such questions can be answered only through research into fundamental properties of the scattering of a target as is done in this thesis.

## B. PURPOSE OF THE THESIS

To explore the possibility of identifying targets through their different responses to excitations of various frequencies and to obtain design parameters to implement such identification techniques, it is essential to understand the physics involved in the scattering of electromagnetic waves by a target. The most important design parameters for such a target identification system are, first of all, the required bandwidth of the system at one frequency and then the frequencies at which implementation of the system are practical. Simple arguments suggest that the operating frequency should be in the resonance region of the targets of interest. In the Rayleigh region, when targets are small compared to the wavelength, all targets will look alike except for their sizes and it will be difficult to separate targets of similar sizes. In the optical region when the operating wavelength is much smaller than the target, scattering characteristics of a target will depend on localized scattering centers whose sizes are in the order of a few wavelengths. The scattered field will depend strongly on the aspect angles and classification becomes very difficult. Current search radars operate mostly in the 500 MHz to 4 GHz frequency range. For most of the targets of interest, either the target itself or part of its structure is in the resonance region for this range of frequencies. The frequencies of HF radars cover either the upper Rayleigh region or the lowest few resonances of most targets. It appears that current technology can be readily applied to implement this target identification scheme.

To find the required bandwidth and the best operating frequency range the electromagnetic scattering of a target in the resonance region has to be studied. Even though the resonant frequencies depend only on the geometry and the

constituent parts of a target, the scattered electromagnetic wave has an electric field which is a vector whose polarization, strength and phase vary with the location of the receiver as shown in Figure 1.1 below:

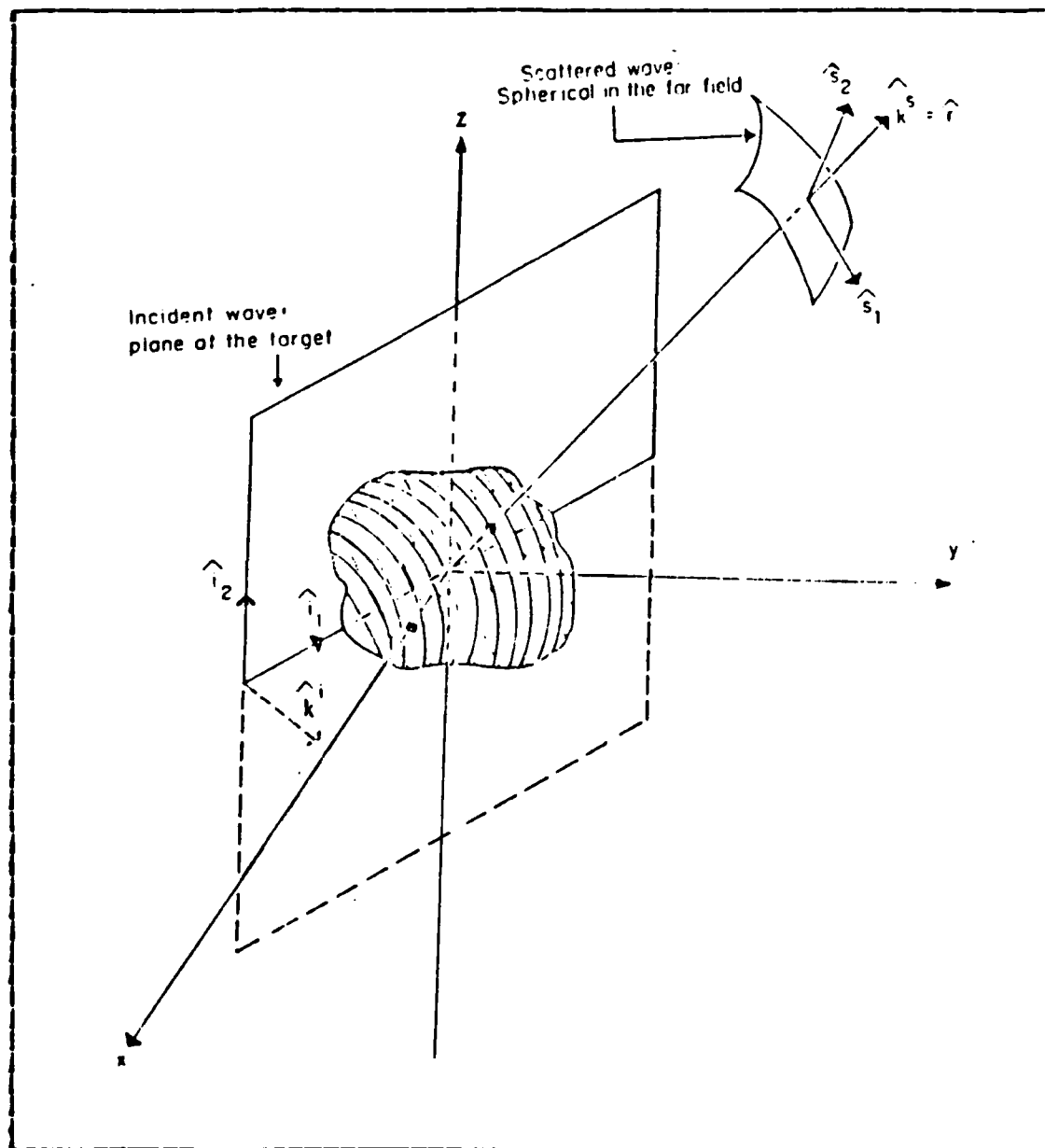


Figure 1.1 Target Scattering Configuration.

Figure 1.1 reveals that this field also varies with the propagating direction and the polarization of the incident wave at the target. Thus studying the scattering phenomenon experimentally is a laborious task. Added to the difficulties is the fact that classes of resonances may not be excited under certain experimental configurations and there is almost no way of knowing it beforehand. Theoretical investigation appears to be a more efficient alternative.

With their complexity, the Maxwell equations seldom render themselves to ready solutions when applied to a finite structure. Only the sphere and the disc of zero-thickness have been solved analytically. These targets have only the radius as their single geometrical parameter. Reitlinger derived an algorithm which calls for the inversion of an infinite set of infinite systems of equations for the solution of the spheroid problem. Because of the difficulties involved in obtaining the coefficients of the systems of equations, no specific result has been reported [Ref. 1]. Recently, Lee carried out a double series expansion for the Green's function on a tubular cylindrical structure of finite length. Analytic expressions for the series expansion coefficients were obtained for both a ring and a cylinder [Ref. 2]. A system of linear equations were derived whose coefficients are linear combinations of less than eight terms of the expansion coefficients of the Green's function [Ref. 3]. Since analytic expressions are available, these coefficients can be computed to desired any accuracy efficiently.

A finite tubular cylinder, similar to a spheroid, has two geometrical parameters which can be varied independently. This property is desirable in the investigation of the effects of changing shapes on resonance characteristics. Such effects will be important in answering the bandwidth problem in target identification. The tubular cylinder

differs from the spheroid in that it separates the space into an internal and an external region which are not sealed off. Since all the targets of practical interest are never completely sealed from the outside, this geometry offers a model for studying the coupling between the internal modes and the external modes of such targets.

There is no justification for a theory except through experimental verification. Comparison between experimental data and theoretical results usually leads to better understanding of the physics involved [Refs. 4,5]. A CW step-frequency range has been developed for measuring the back scattered electric field of a target. The purposes of the thesis work are to improve the scattering range, to obtain accurate experimental data of the back scattered field and to compare measured data to theoretical predictions.

## II. SYSTEM IMPROVEMENTS AND EXPERIMENTAL MEASUREMENTS

The automated CW step-frequency range has been operating since June 1984 when the development of all the software was completed. The system was controlled by an HP - 85 microcomputer. Tests of system stability was carried out by Mario Loric [Ref. 6]. The data obtained by him from 10 GHz to 15 GHz appeared to be good. Those data tended to fluctuate randomly and deteriorated with elapsed time from initial system calibration. Below 10 GHz, the coupling between the transmitting and the receiving antennas was so strong that the back scattering signal from the target could not be detected.

An averaging process was designed by Geller and Haklay [Refs. 7,8]. Repeatable results were obtained by averaging four to five sets of data. This was a laborious process; in the first scan the output frequency of the generator was increased from 10 GHz to 15 GHz at 100 MHz steps when the target was absent. The response gave the background contribution to the received field which included antenna coupling effect and back scattering from the anechoic chamber and the target support. A standard conducting sphere was then used as the target to calibrate the system response at each frequency step in the second scan. The background data were taken again in the third frequency scan. The fourth frequency scan, with the target in place, provided the back scattered field strength and phase from the target. This sequence of procedures was repeated and the results averaged.

As shown in Figure 2.1, the voltage controlled oscillator (VCO) is serving as a local oscillator and is operated at some frequency between 65 MHz to 150 MHz. Its output

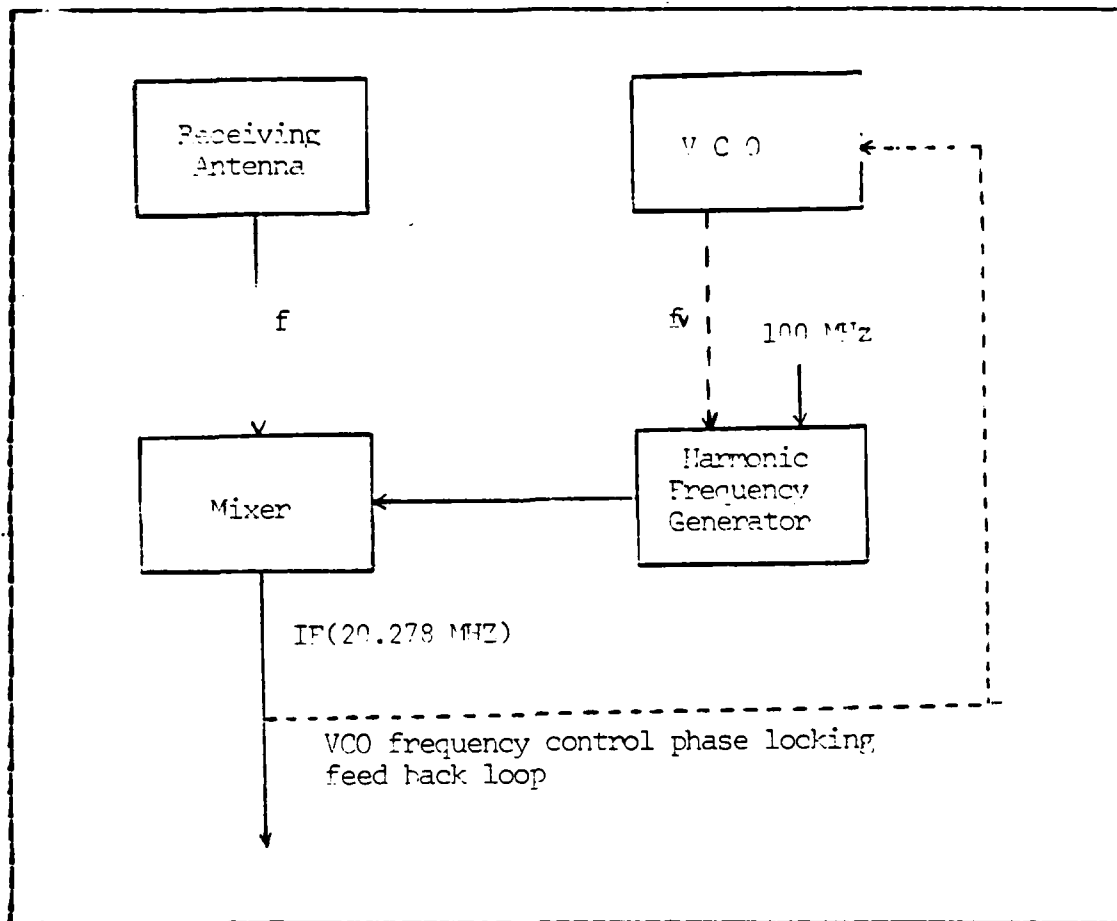


Figure 2.1 IF Frequency Conversion Process.

signal at the frequency  $f$  is fed into the harmonic generator in which signals of frequencies which are integer multiples of  $f$  are generated. These harmonics are combined in the mixer with the input signal at the test frequency  $f$  from the receiving antenna. The signals are filtered and the resultant signal is output from the mixer and fed back to complete a phase lock loop which controls the VCO frequency. The system can be phase locked when the mixer outputs an intermediate frequency (IF) near 20.278 MHz. This is the difference between the test frequency  $f$  and the  $n$ th harmonic frequency  $nf$  where  $n$  is an integer. At a given test

frequency  $f$ , several different  $f_v$ 's and  $n$ 's may combine to yield the same IF value. But due to the non-linearity of the characteristics of the harmonic frequency converter and the mixer, these different  $f_v$  and  $n$  pairs will give rise to different system responses. The random fluctuation in system frequency response was determined to be a result of this effect, called harmonic skipping, of the vector network analyzer. It was decided that the feedback loop of the analyzer be disconnected and the local oscillator frequency be controlled externally so that at one test frequency  $f$ ,  $f_v$  and  $n$  will always be the same. Since this technique was implemented, system repeatability has been improved and no data averaging has been required.

#### A. SYSTEM IMPROVEMENT

A new HP-9836CU workstation was installed to replace the HP-85 microcomputer as the system controller. The software was converted and a data link was set up between the IBM-3033 mainframe computer and this workstation. Experimental data were sent to the mainframe and theoretical results were sent to the workstation for plotting and comparison purposes. The incorporation of the much faster HP-9836CU workstation made it possible to control the local oscillator frequency directly so that the feedback loop could be disconnected. The 100 MHz back panel output from the RF source, an HP-8672A synthesized signal generator, was used to provide the local oscillator signal to replace the VCO in the vector network analyzer. The RF frequencies were chosen at integer multiples of 100 MHz plus the IF frequency. Because of the stability of the RF signal generator, and because the harmonic number was completely determined from this choice of the RF and the local oscillator frequencies, this technique overcame the harmonic

skipping problem. The scan-to-scan repeatability had been good and no data averaging was necessary. Even though the specified IF frequency of the vector network analyzer was 20.278 MHz, the phase was not properly locked at several frequencies between 12.4 GHz and 17.1 GHz. IF frequencies which deviate from 20.278 MHz by a few KHz were chosen and the theoretical back scattered fields from the standard sphere were re-computed so that calibrations at the corresponding RF frequencies could be carried out. Since these particular IF frequencies depended on how the target support was placed, they had to be changed and the theoretical field values re-computed from time to time. These procedures were carried out expediently only after the new computer was installed.

Table I lists the components of the current setup of the automated back scattering data collection system. A functional block diagram is shown in Figure 2.2 and symbols depicting signal flow are given in Table II.

**TABLE I**  
**LIST OF EQUIPMENT**

HP-9836CU	Engineering workstation.
HP-7475A	Plotter.
HP-7245B	Plotter and printer.
HP-8411B	Harmonic frequency converter.
HP-8672A	Synthesized signal generator.
HP-8412E	Phase and Magnitude Display.
HP-3455A	Digital Voltmeter.
HP-3456A	Digital Multimeter.
HP-6227A	Dual DC power supply.
NARDA-5292	Directional coupler.

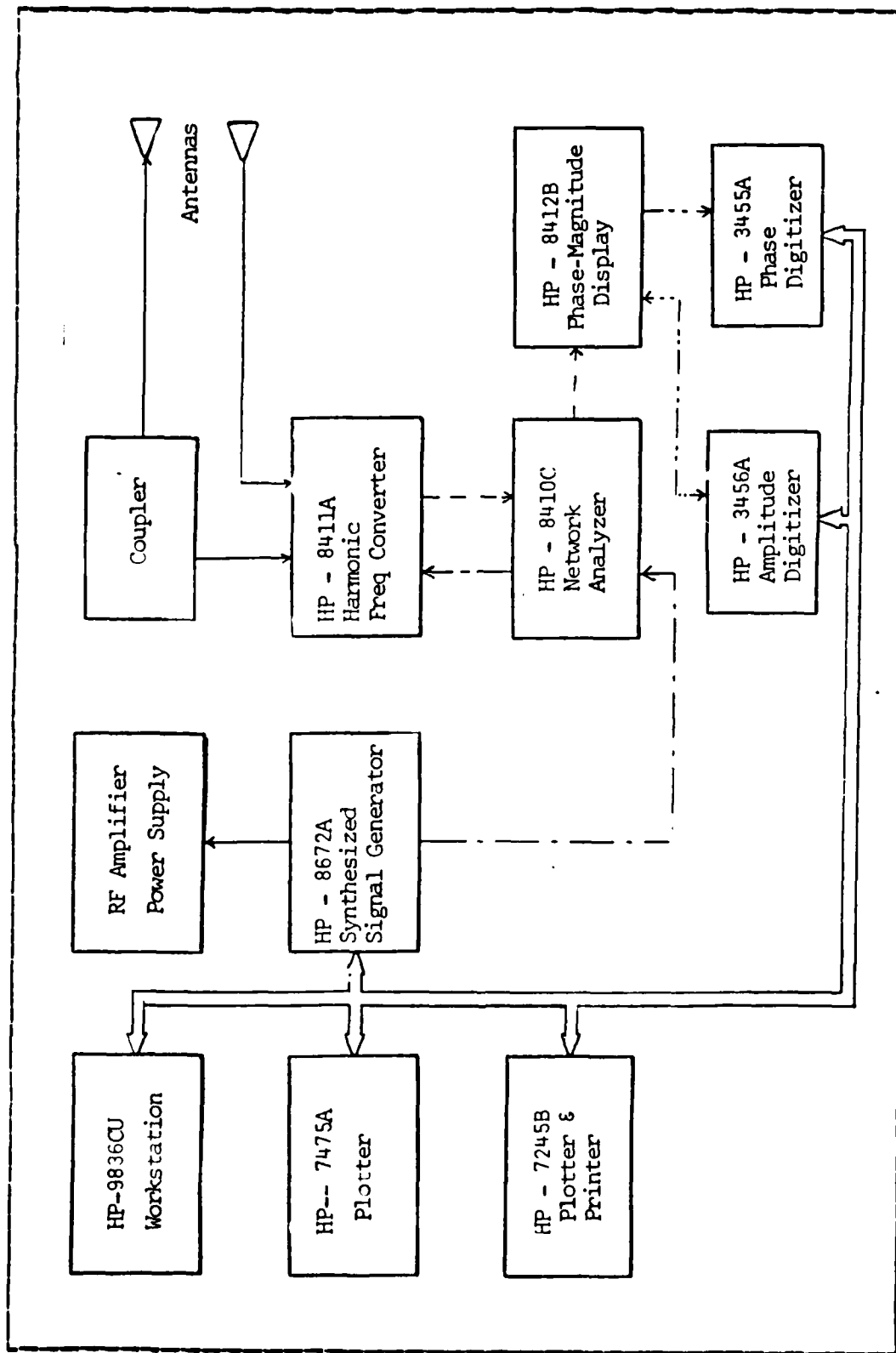
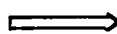


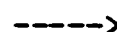



Figure 2.2 Block Diagram of System.

**TABLE II**  
**SIGNAL FLOW SYMBOLS FOR FIGURE 2.2**

	Digital data path.
	RF signal path(10.1 - 17.1 GHz).
	100 MHz local oscillator signal path.
	278 KHz signal path.
	DC.

The automated CW step-frequency back scattering measurement system consists of four parts. As shown in Figure 2.2, they are:

- (1) Digital control and data processing.
- (2) RF generation and amplification.
- (3) RF radiation and receiving.
- (4) Receiver unit.

The HP-9836CU workstation controls the frequency and the output power level of the synthesized signal generator HP-8672A. The output RF signal from the generator is amplified by the 6 GHz - 18 GHz amplifier and fed to the transmitting horn antenna through the directional coupler. The back scattered field of the target is collected by the receiving horn antenna and fed to the test port of the harmonic frequency converter HP-8411A. The portion of the amplified output signal coupled out through the directional coupler is attenuated by 43dB before it is fed to the reference port of the harmonic frequency converter. The harmonic frequency converter and the network analyzer HP-8410C, together with the phase and magnitude display unit HP-8412B function as a phase difference and magnitude ratio meter between the transmitted and the received signals. The phase difference and the magnitude ratio are converted to volts that are measured by the digital voltmeters HP-3455A and HP-3456A. Both the magnitude and the phase of the reflected

signal are digitized by these voltmeters and stored in the microcomputer.

### B. THE TARGET

Table III lists the specifications of all targets used in this experiment [Ref. 9]. They are thin wall brass tubes of various lengths and diameters. The wall thickness of each target is much smaller than the other dimensions of that target and the wavelength of the incident field. A picture of the targets is shown in Figure 2.3.

TABLE III  
TARGET SPECIFICATION

Name	Length(2h: cm)	Diameter(2a: cm)		Ratio
		Inner	Outer	
Cylinder 1	11.09	1.349	1.308	6
Cylinder 2	3.18	1.516	1.588	6
Cylinder 3	7.193	1.199	1.27	6
Cylinder 4	5.349	0.8915	0.9525	6
Cylinder 5	7.396	1.349	1.308	6
Cylinder 6	6.064	1.516	1.588	6
Cylinder 7	4.756	1.199	1.27	4
Cylinder 8	3.566	0.8915	0.9525	4

REPRODUCED AT GOVERNMENT EXPENSE

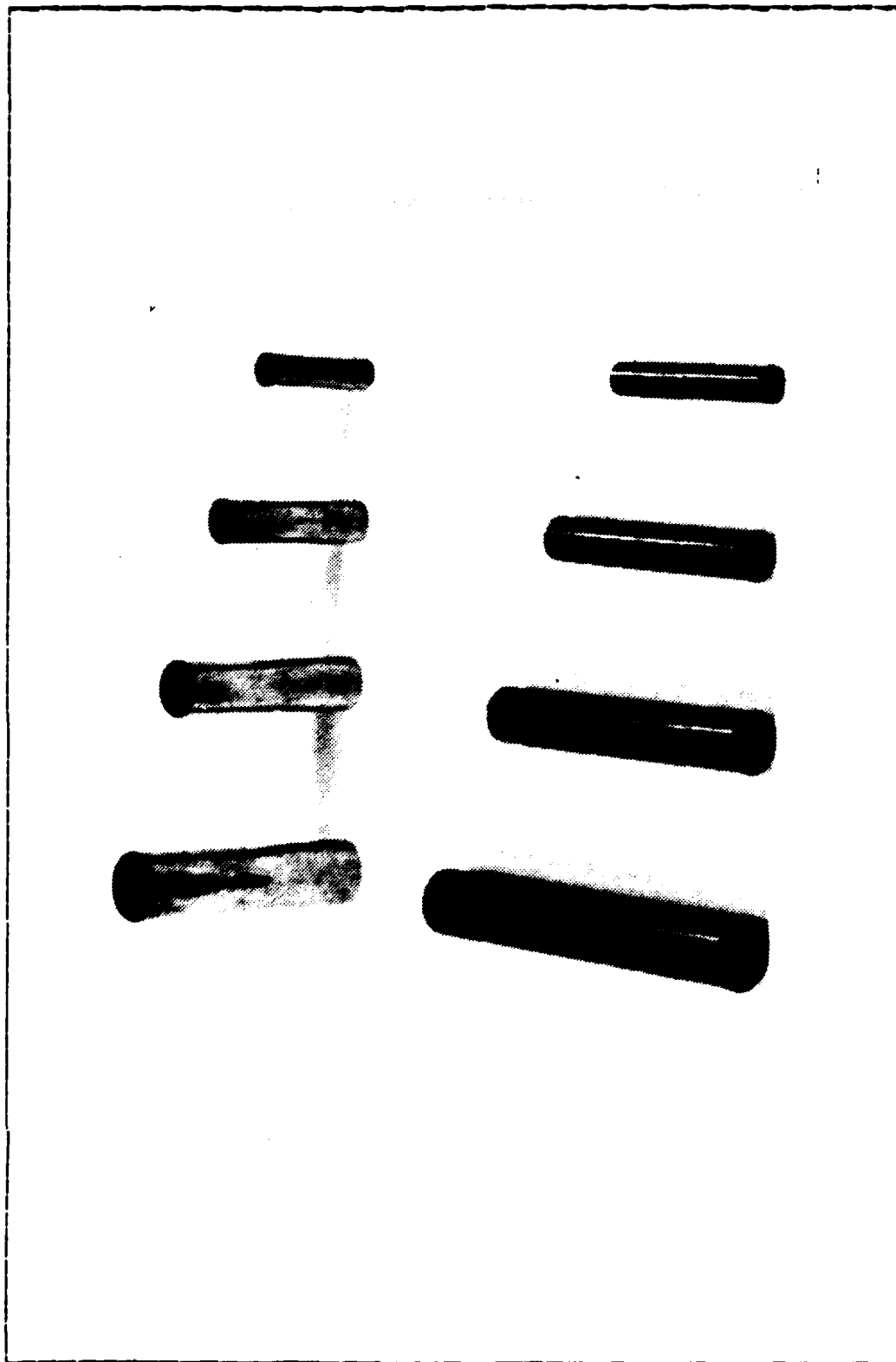


Figure 2.3 Target Geometry.

### C. THE ANECHOIC CHAMBER AND THE TARGET SUPPORT

The anechoic chamber is 20 ft deep with a 10 ft x 10 ft cross section. The chamber is internally lined with RF absorbers so that reflections from walls are minimized. As shown in Figure 2.4, two orientations of the target are tested. They are called the "Head-on" case and the "Broadside" case respectively. The direction of propagation of the incident wave is parallel to the axis of the target in the head-on case and is perpendicular to the axis of the target in the broadside case. Though the horn antennas are arranged bistatically, the distance between the transmitting antenna and the receiving antenna is much shorter than the antenna-target distance and the scattering is considered to be monostatic. Supports of different shapes are designed and tested to determine the effects of their coupling with the target. The results are presented in Chapter IV.

### D. MEASURED DATA

The experimental results obtained by stepping up the frequency of the incident wave at 0.1 GHz intervals from 10.1 GHz to 17.1 GHz, plus the selected IF frequencies, are shown in the following figures. The first 16 figures are the head-on cross sections and phase shifts. The next 16 figures show the broadside cross sections and phase shifts. These data are used for comparison with theoretical values and with previous experimental results in the following chapters.

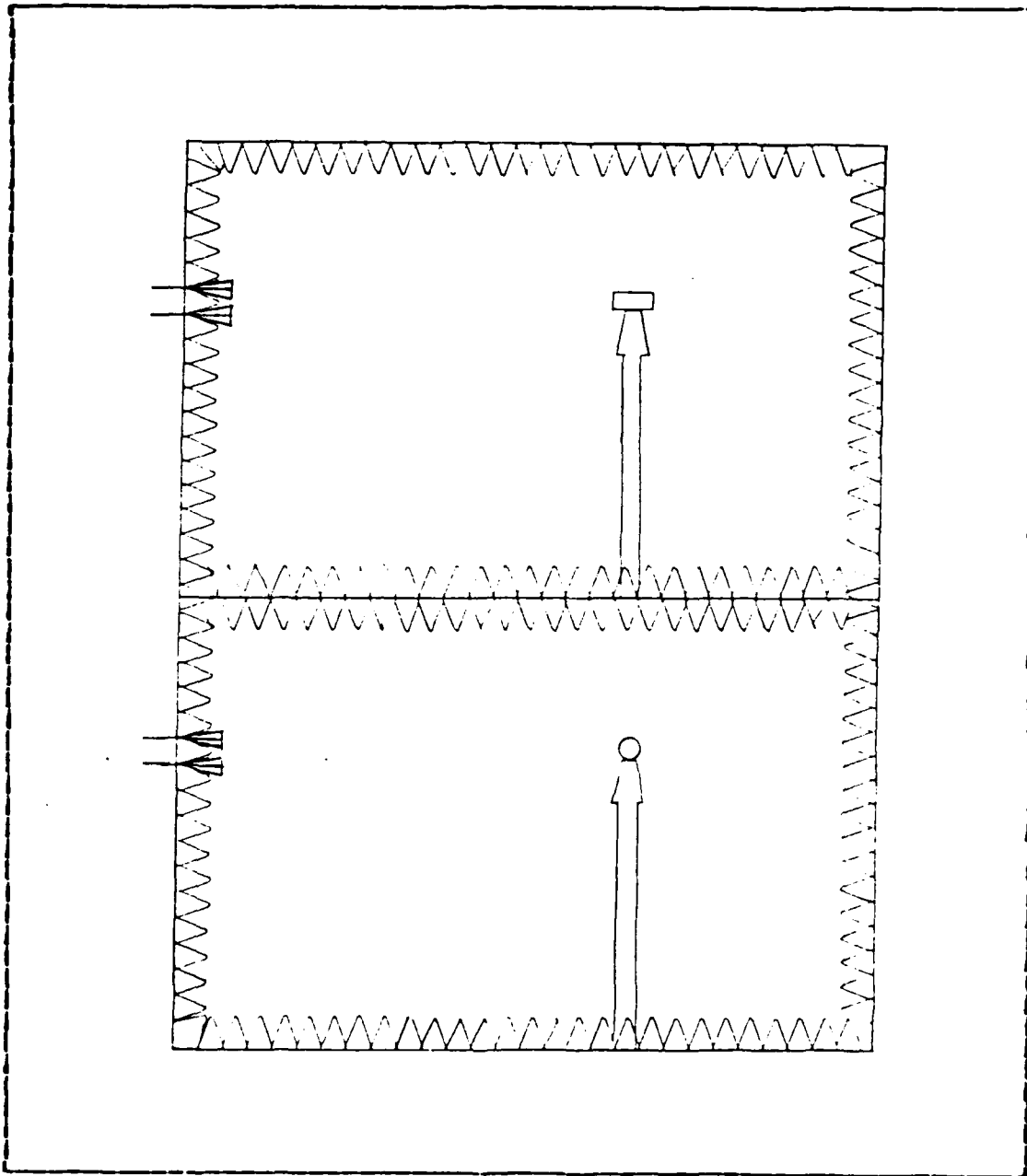


Figure 2.4 Chamber and Target Orientations.

(a) Head-on case (upper figure)

(b) Broadside case (lower figure)

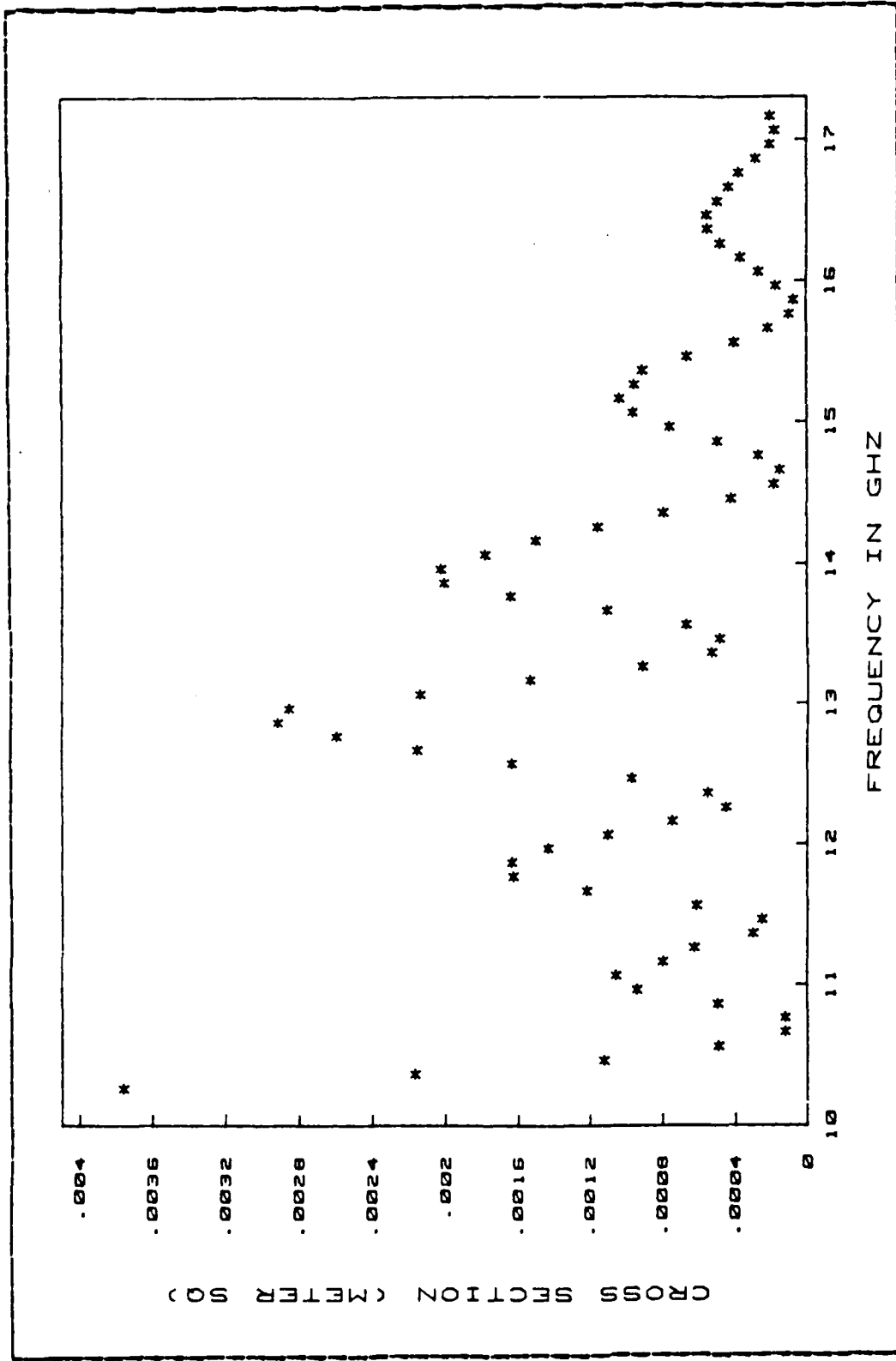


Figure 2.5 Head-on Cross Section of Cylinder 1.

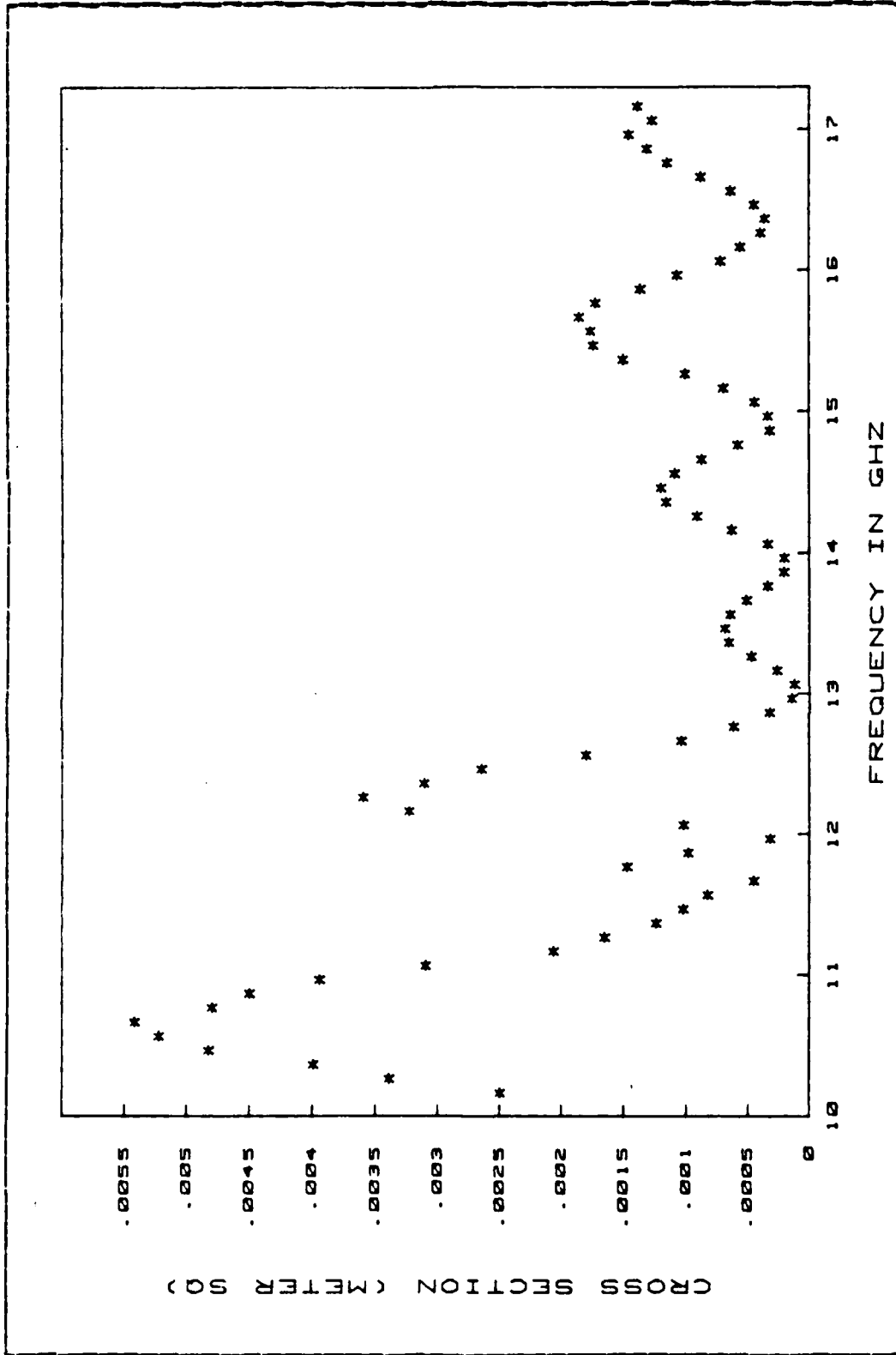


Figure 2-6 Head-on Cross Section of Cylinder 2.

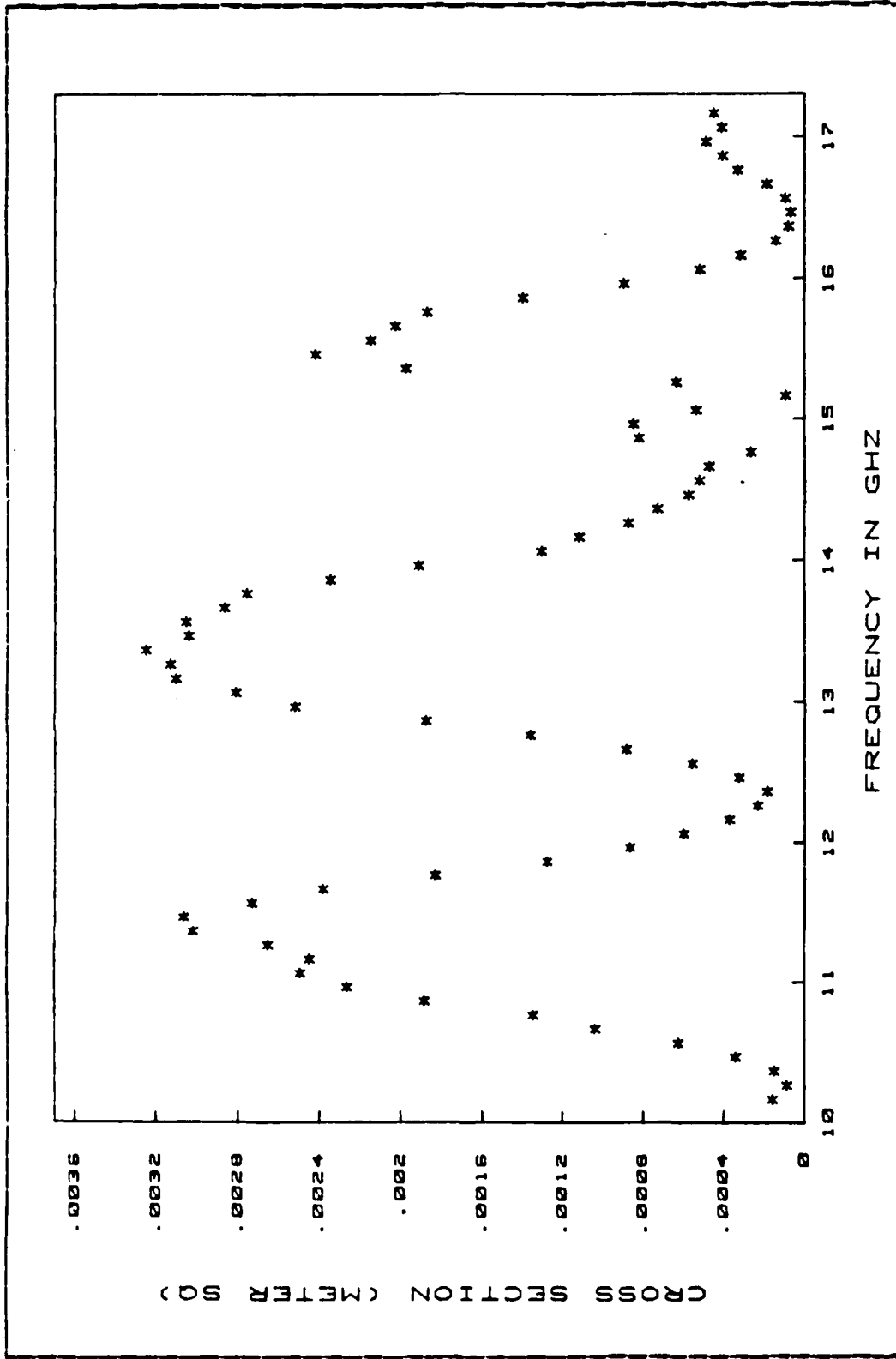


Figure 2.7 Head-on Cross Section of Cylinder 3.

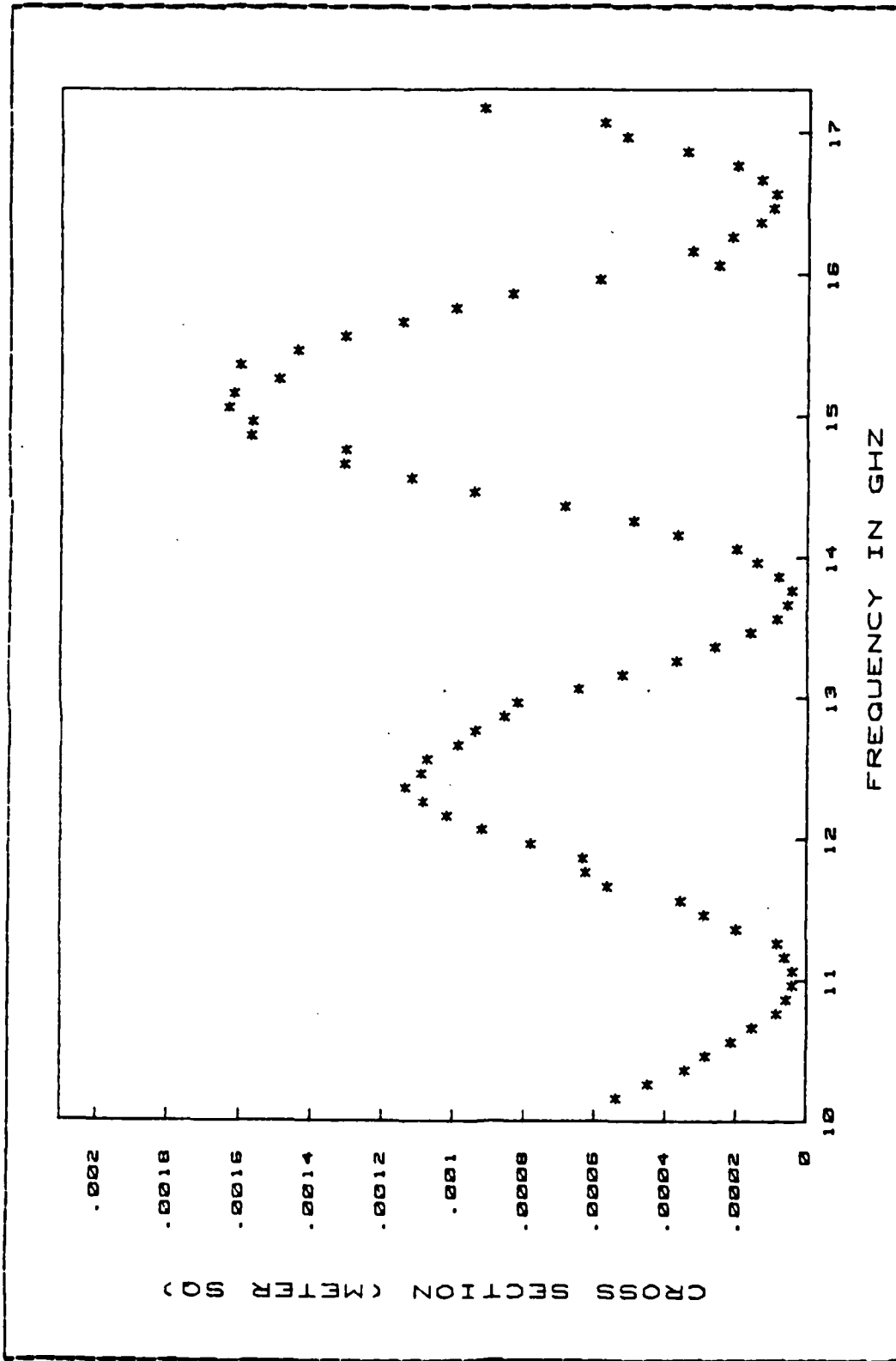


Figure 2.8 Head-on Cross Section of Cylinder 4.

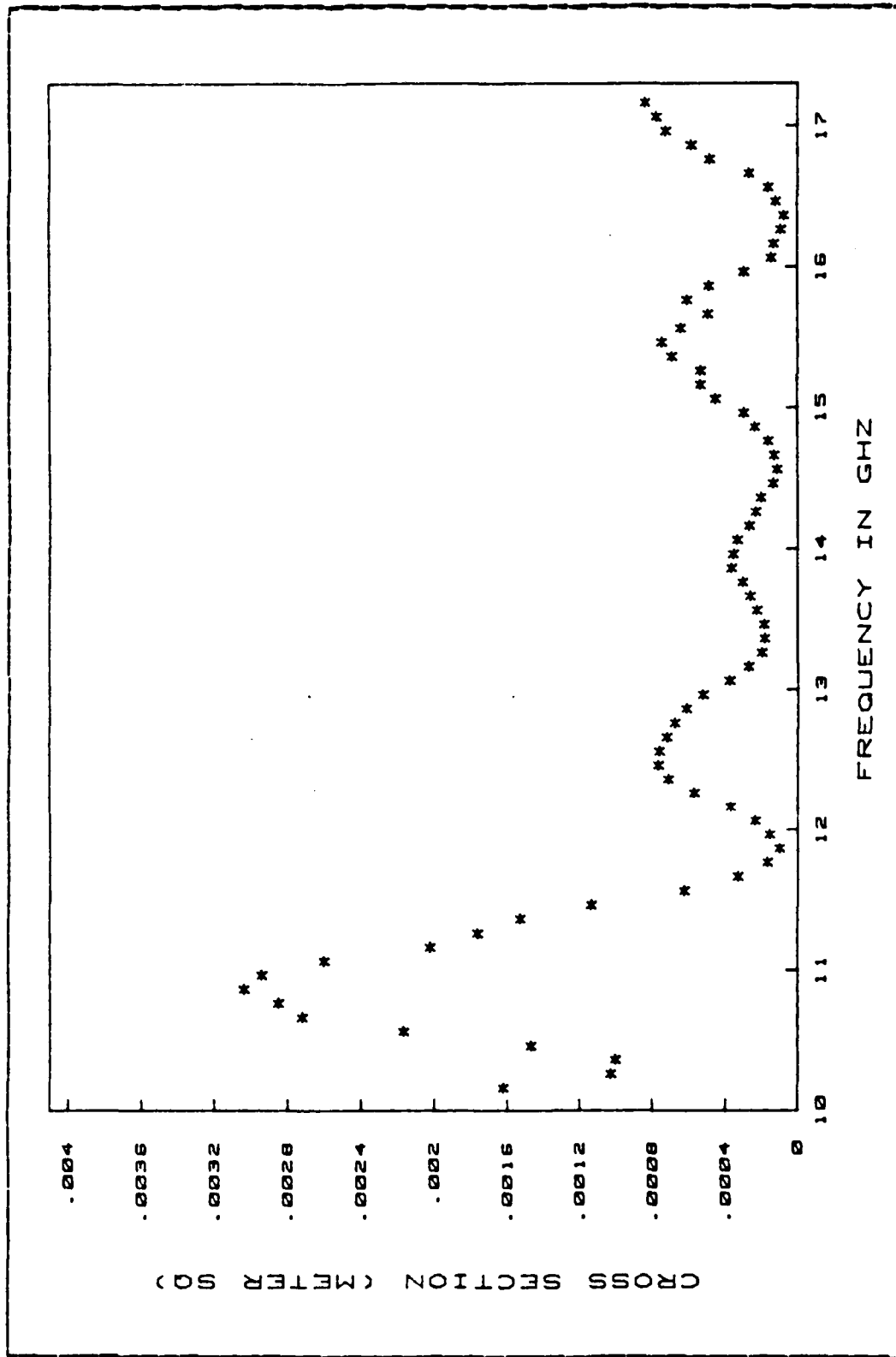


Figure 2.9 Head-on Cross Section of Cylinder 5.

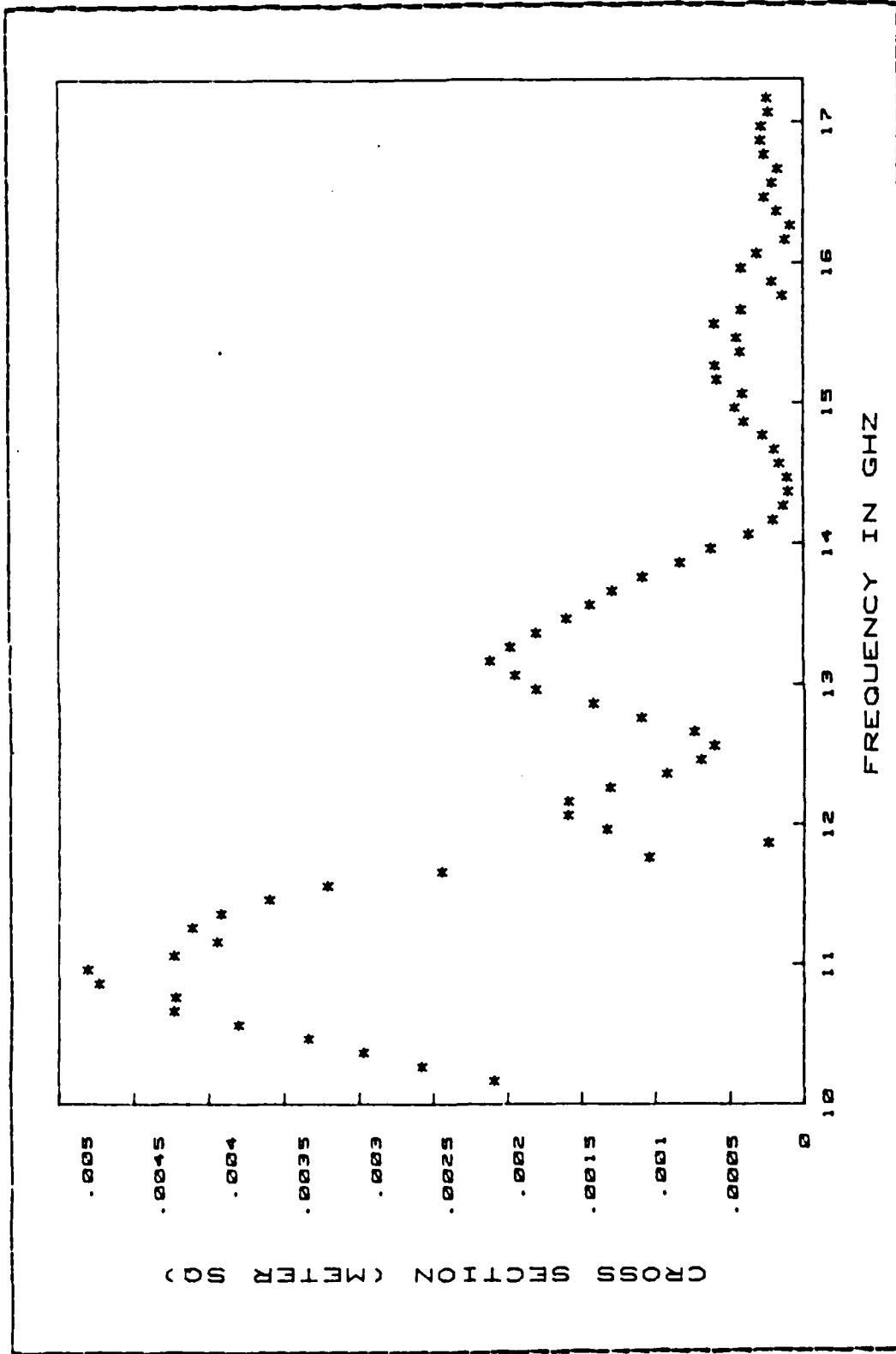


Figure 2.10 Head-on Cross Section of Cylinder 6.

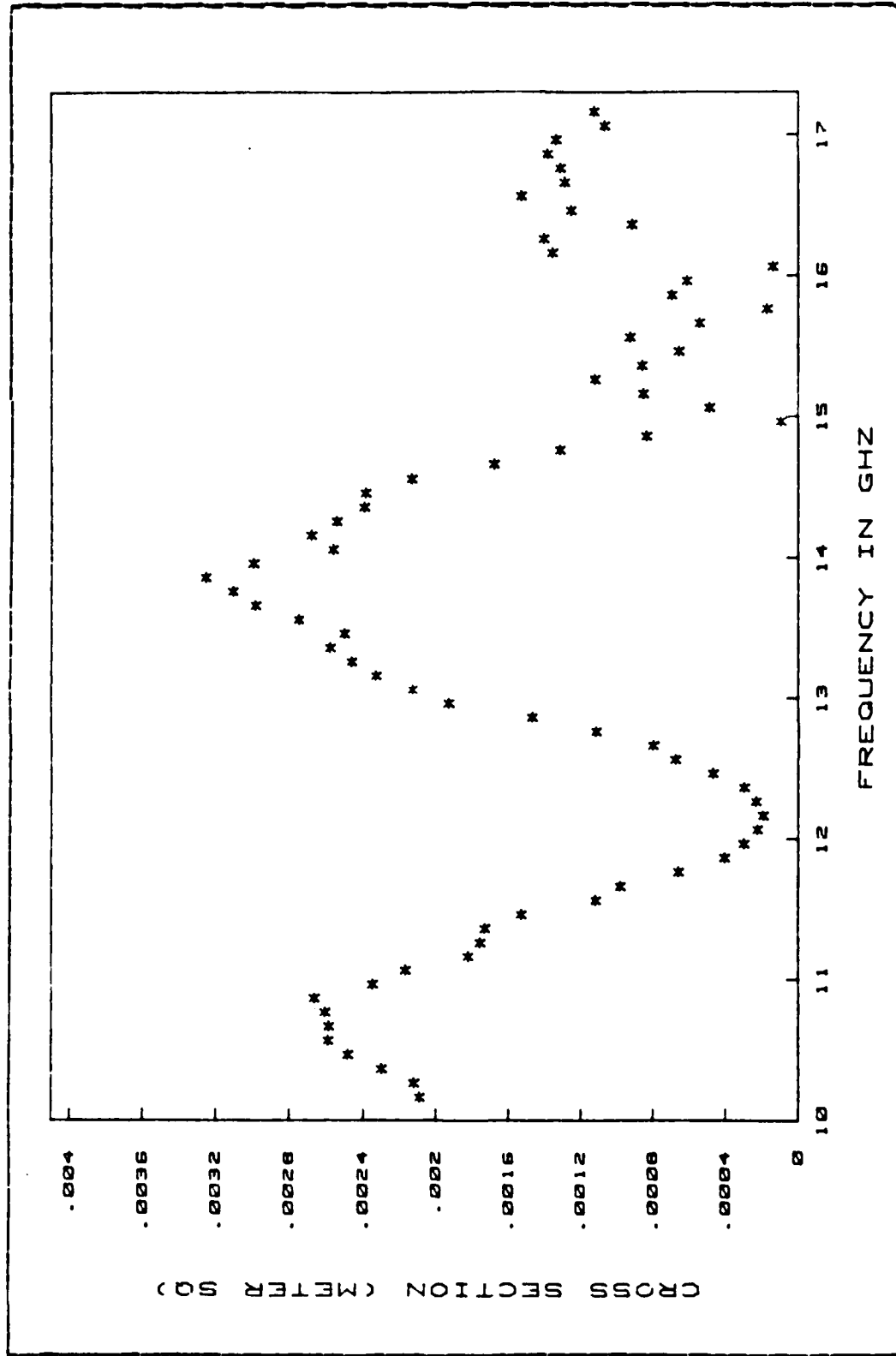


Figure 2.11 Head-on Cross Section of Cylinder 7.

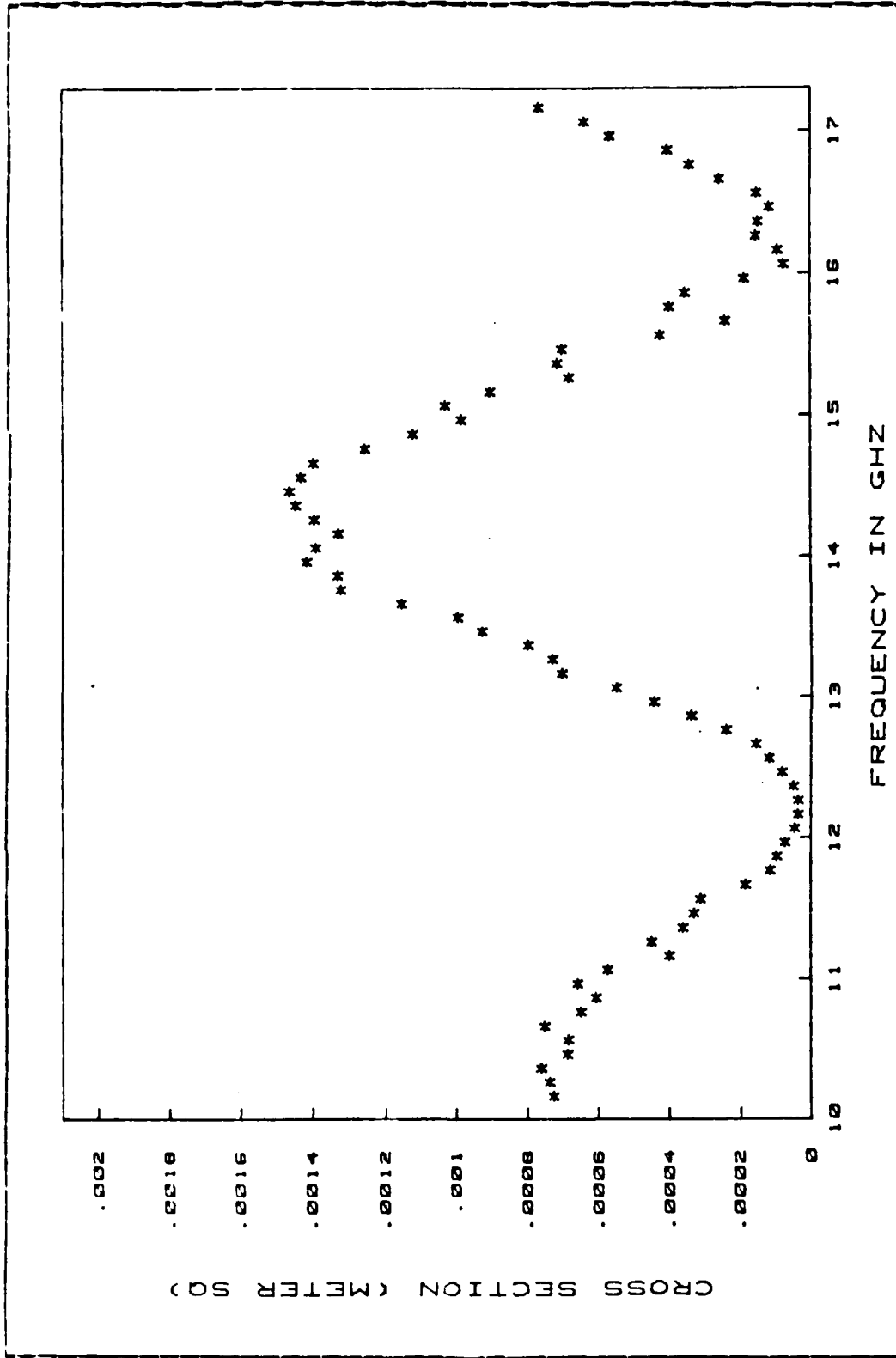


Figure 2.12 Head-on Cross Section of Cylinder 8.

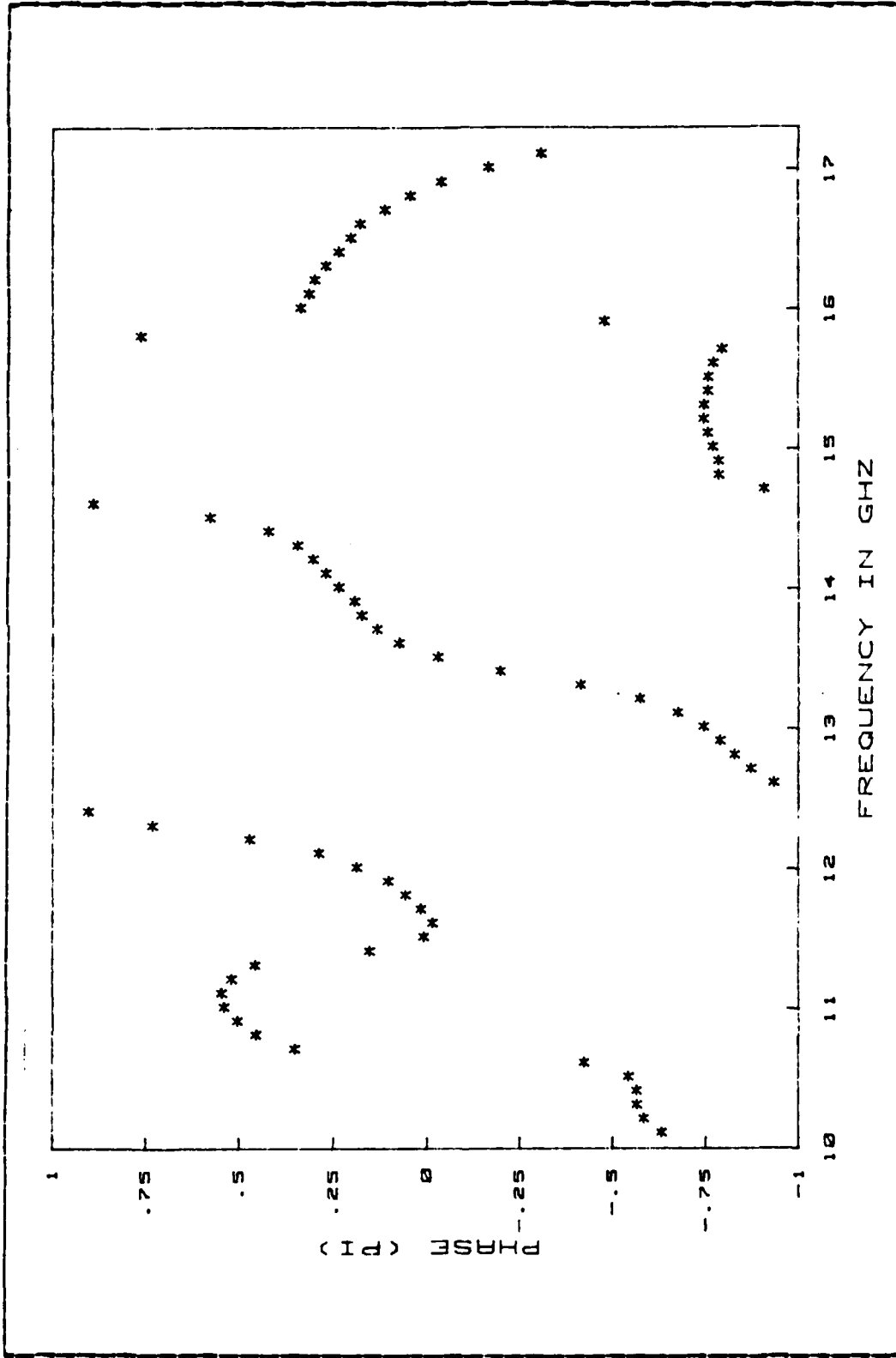


Figure 2.13 Head-on Phase Shift of Cylinder 1.

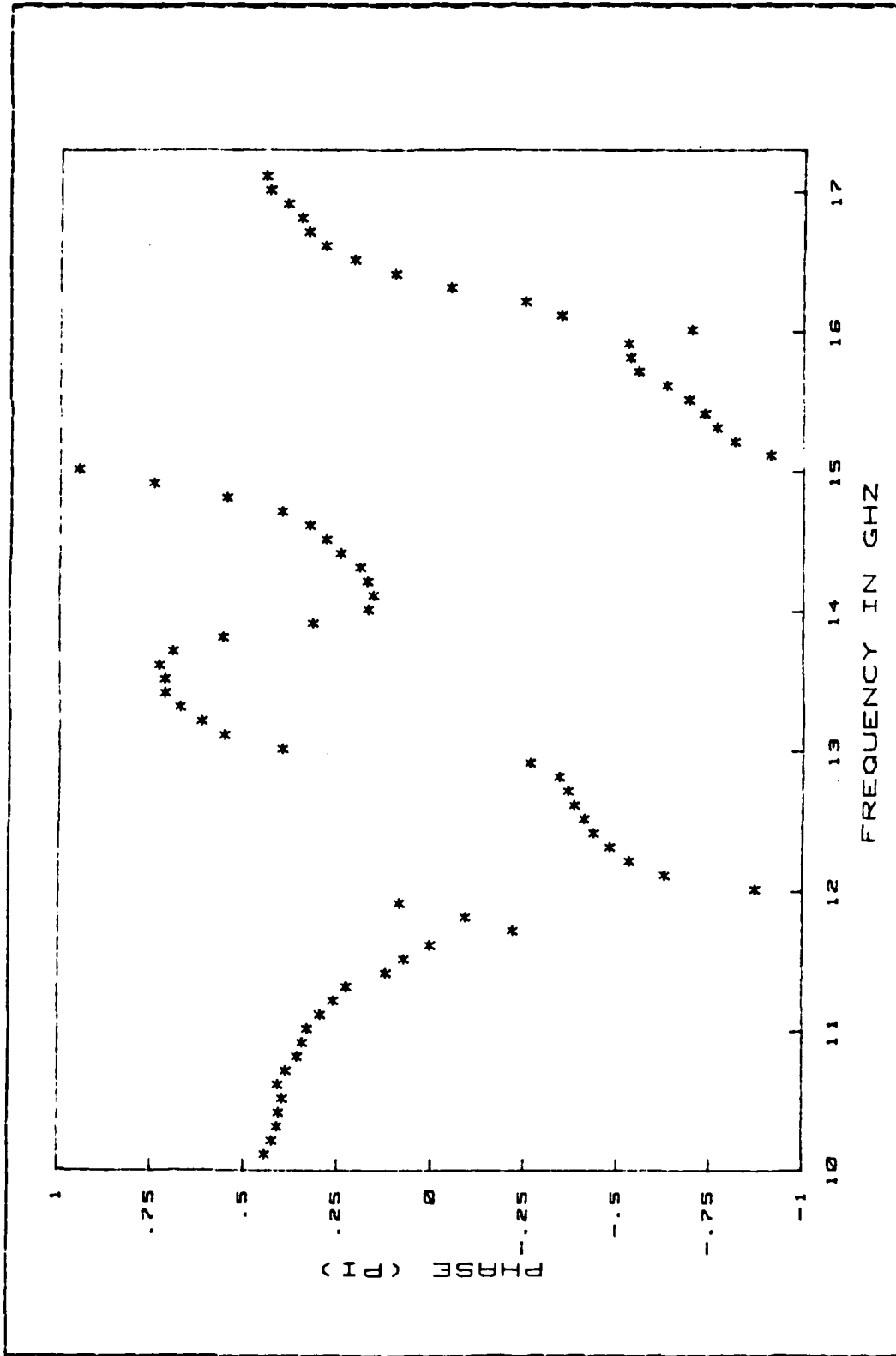


Figure 2.14 Head-on Phase Shift of Cylinder 2.

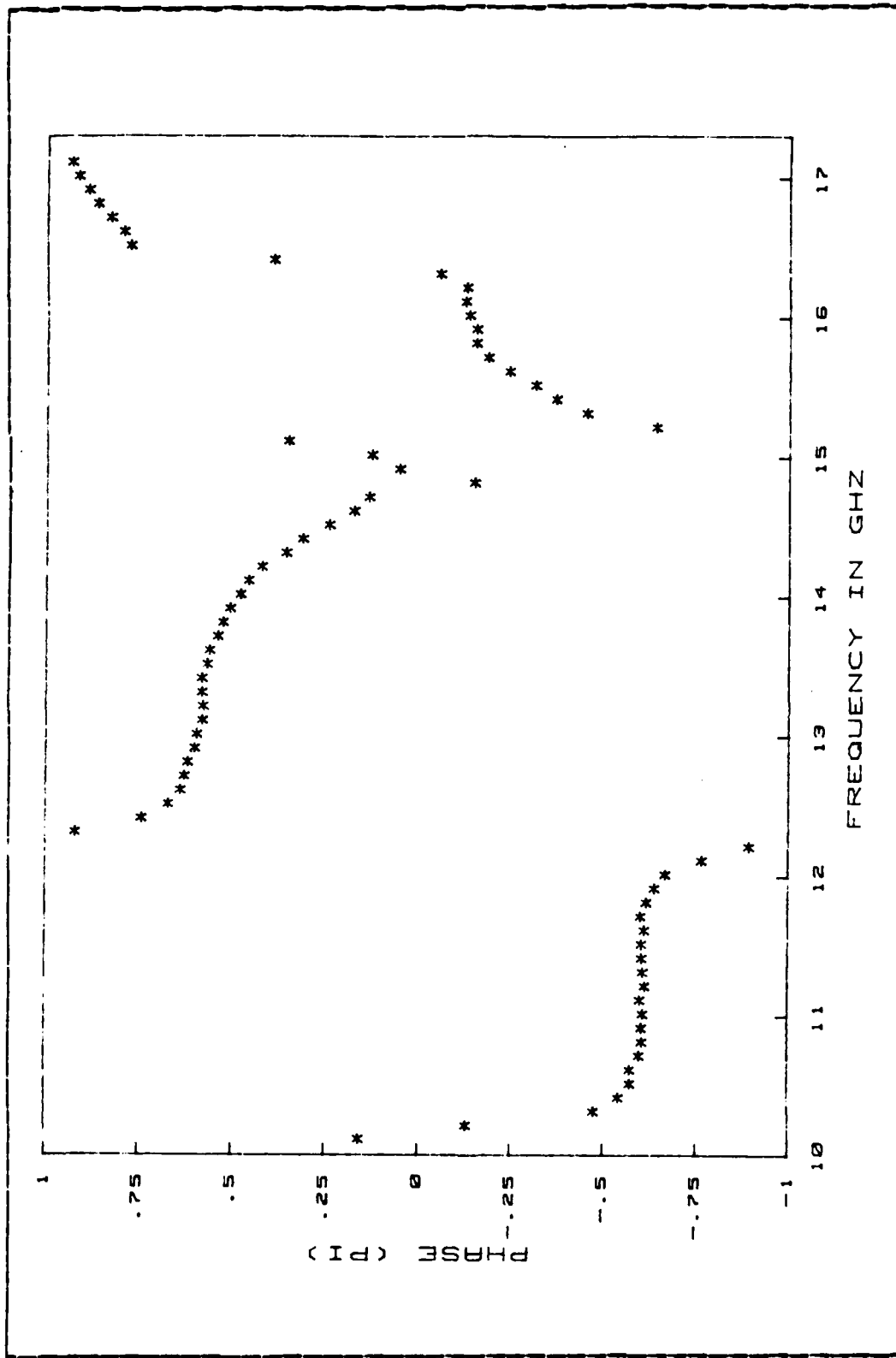


Figure 2.15 Head-on Phase Shift of Cylinder 3.

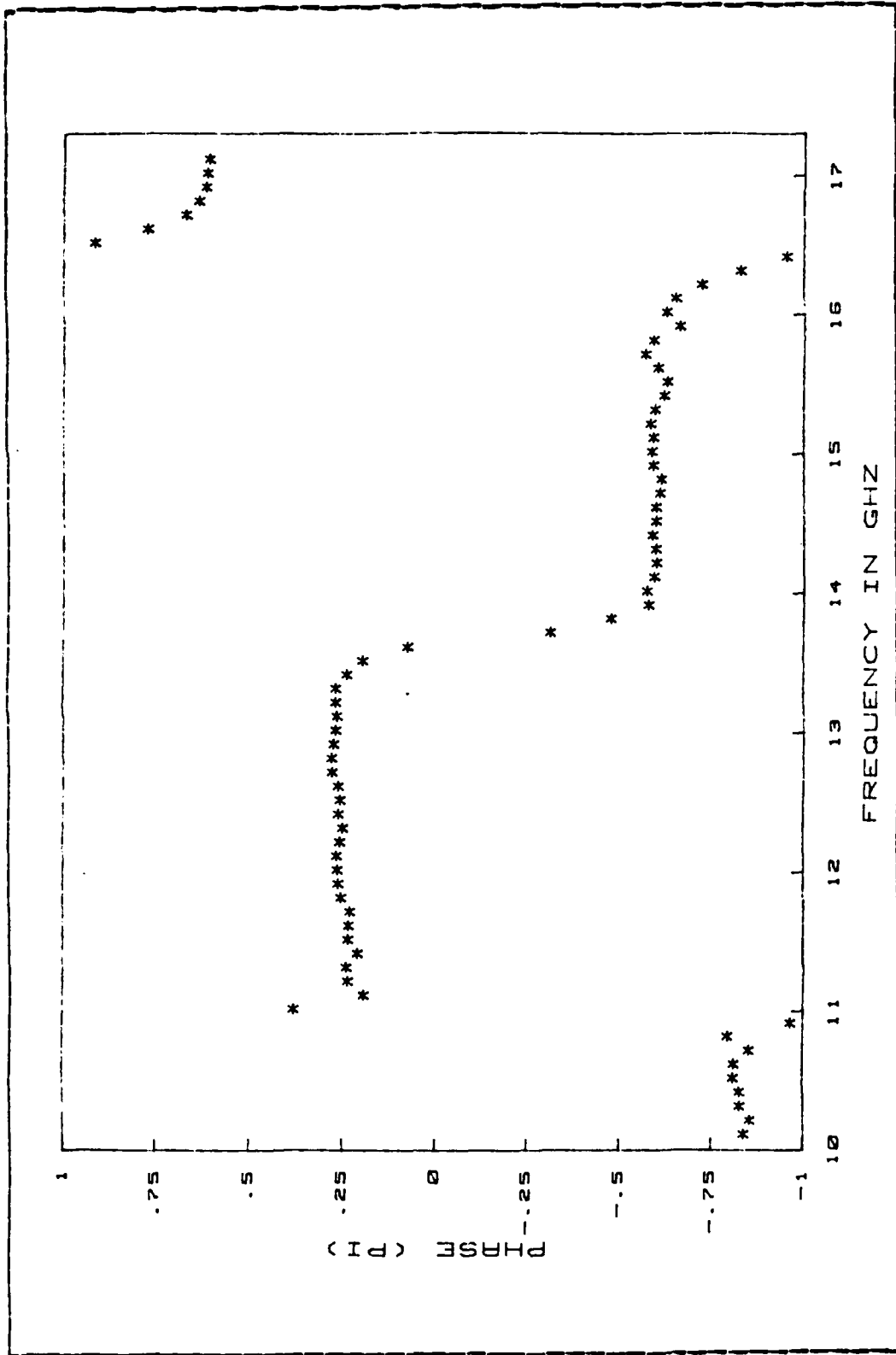


Figure 2.16 Head-on Phase Shift of Cylinder 4.

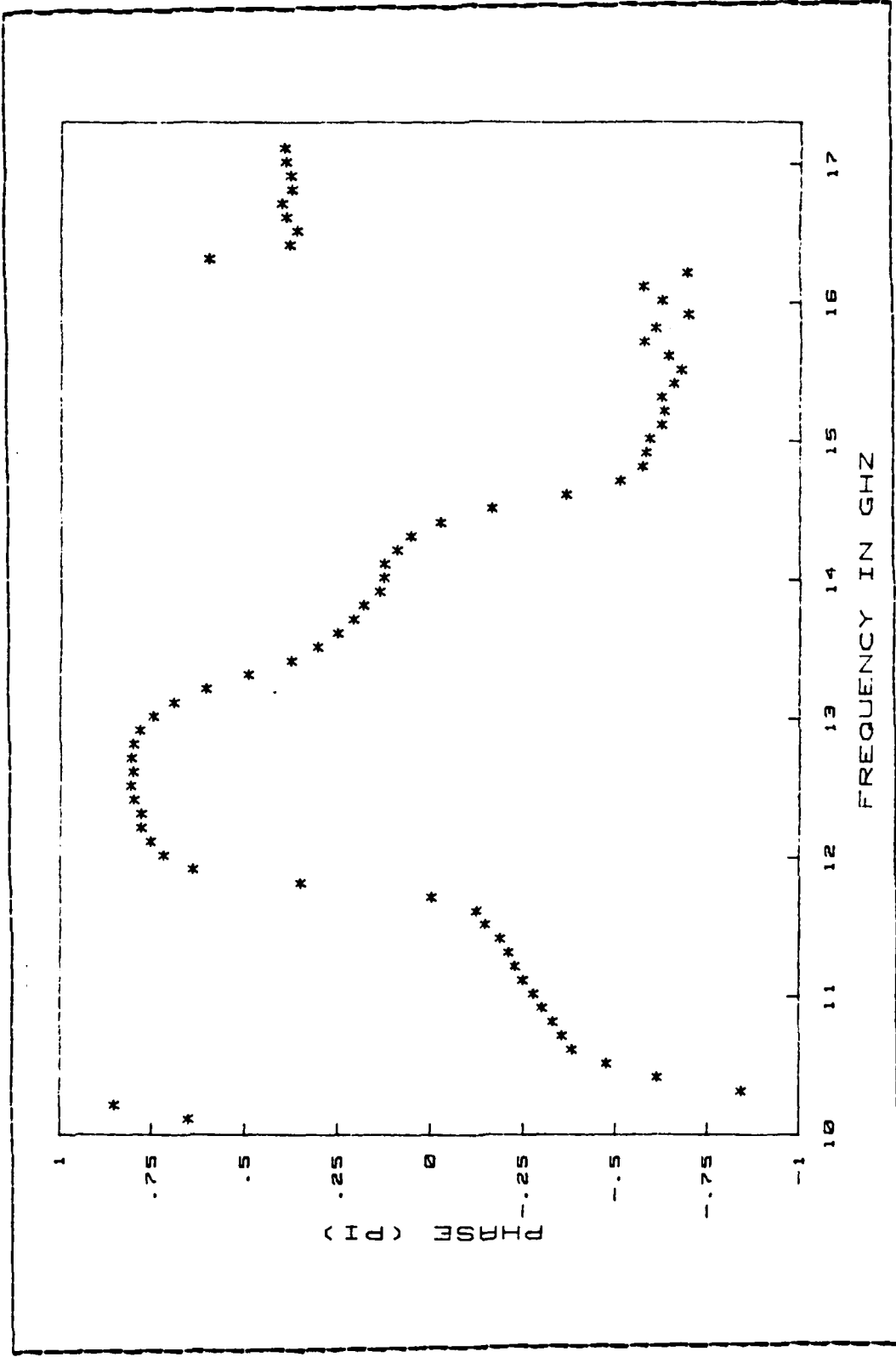


Figure 2.17 Head-on Phase Shift of Cylinder 5.

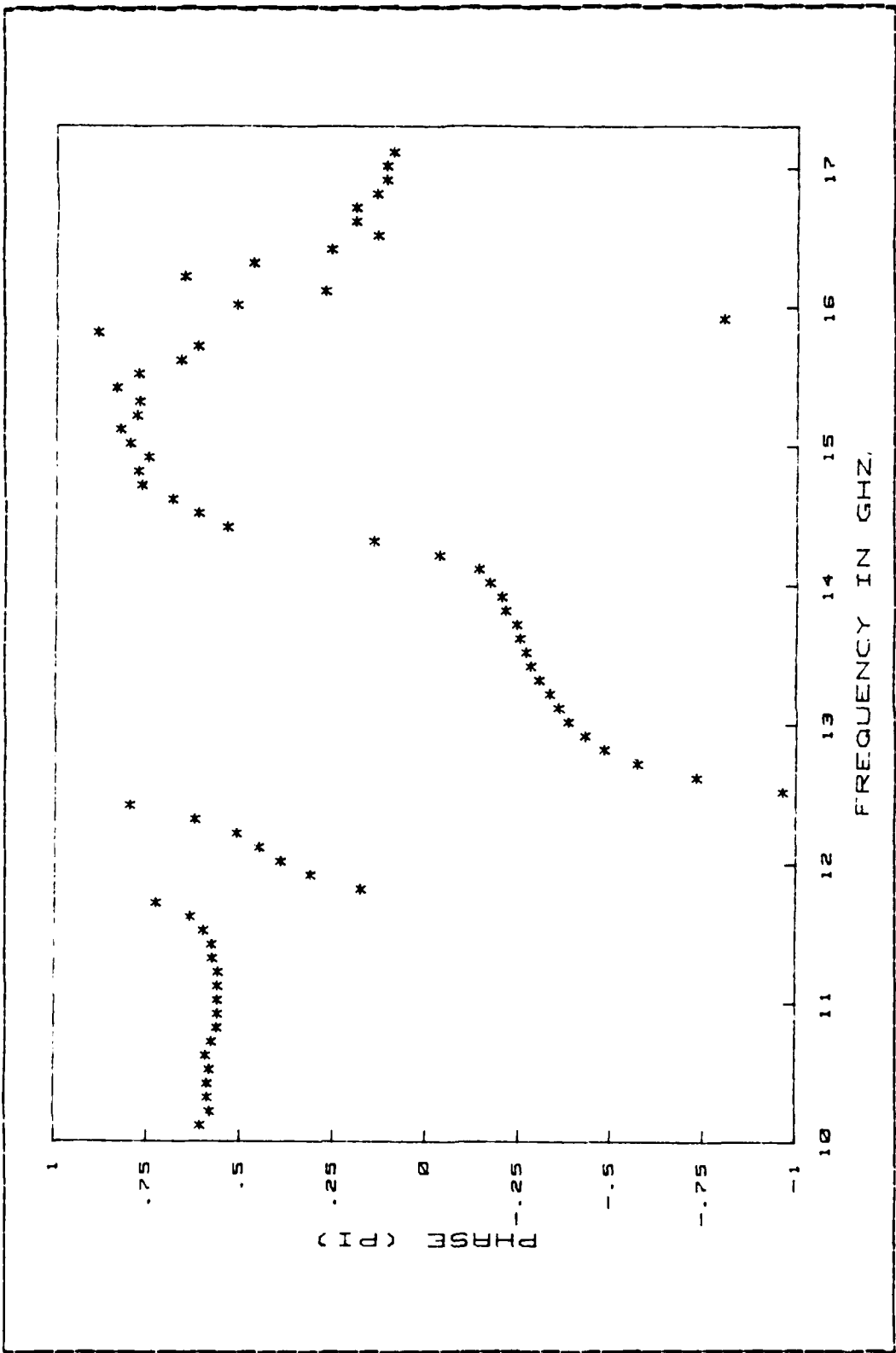


Figure 2.18 Head-on Phase Shift of Cylinder 6.

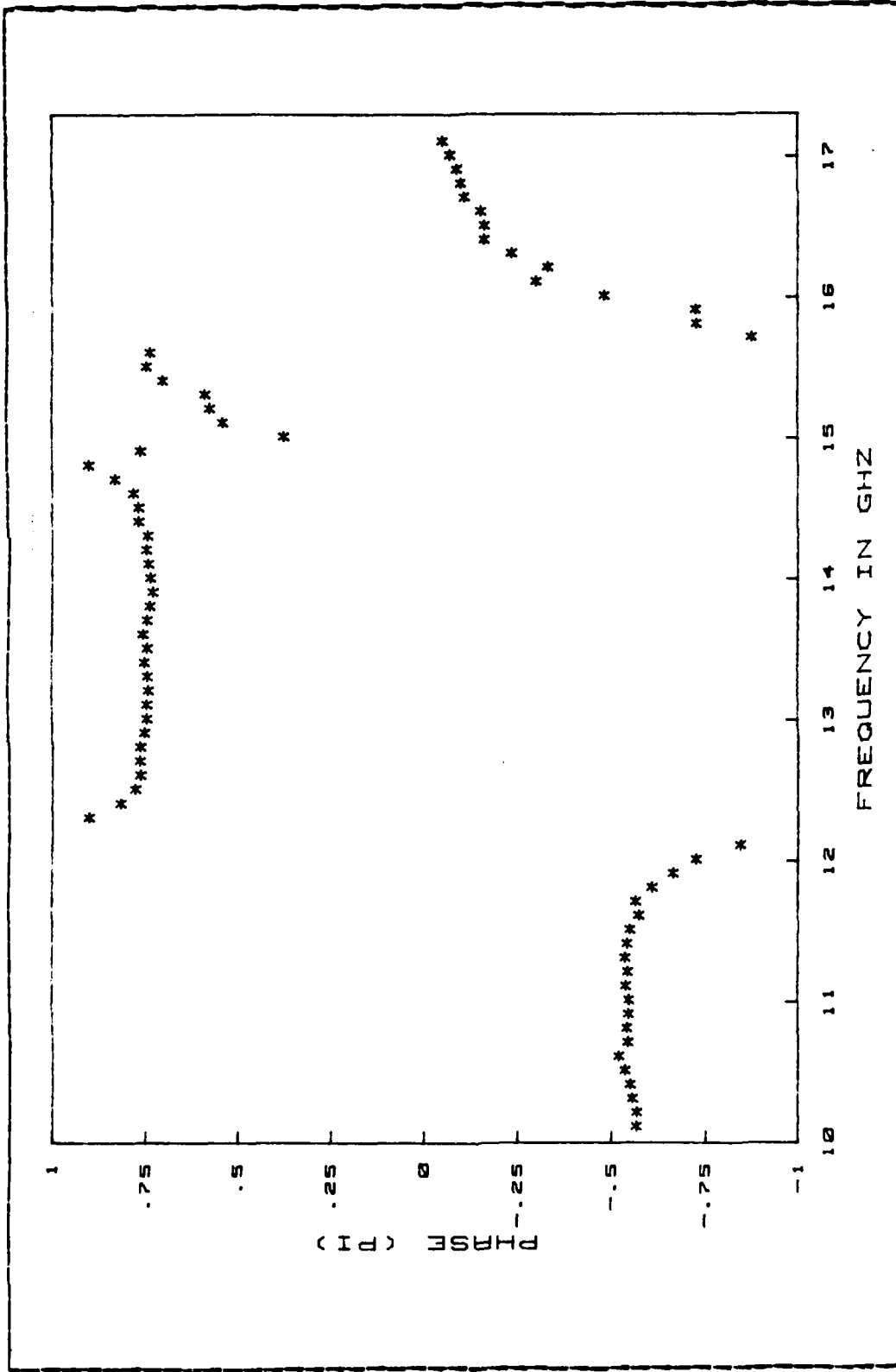


Figure 2.19 Head-on Phase Shift of Cylinder 7.

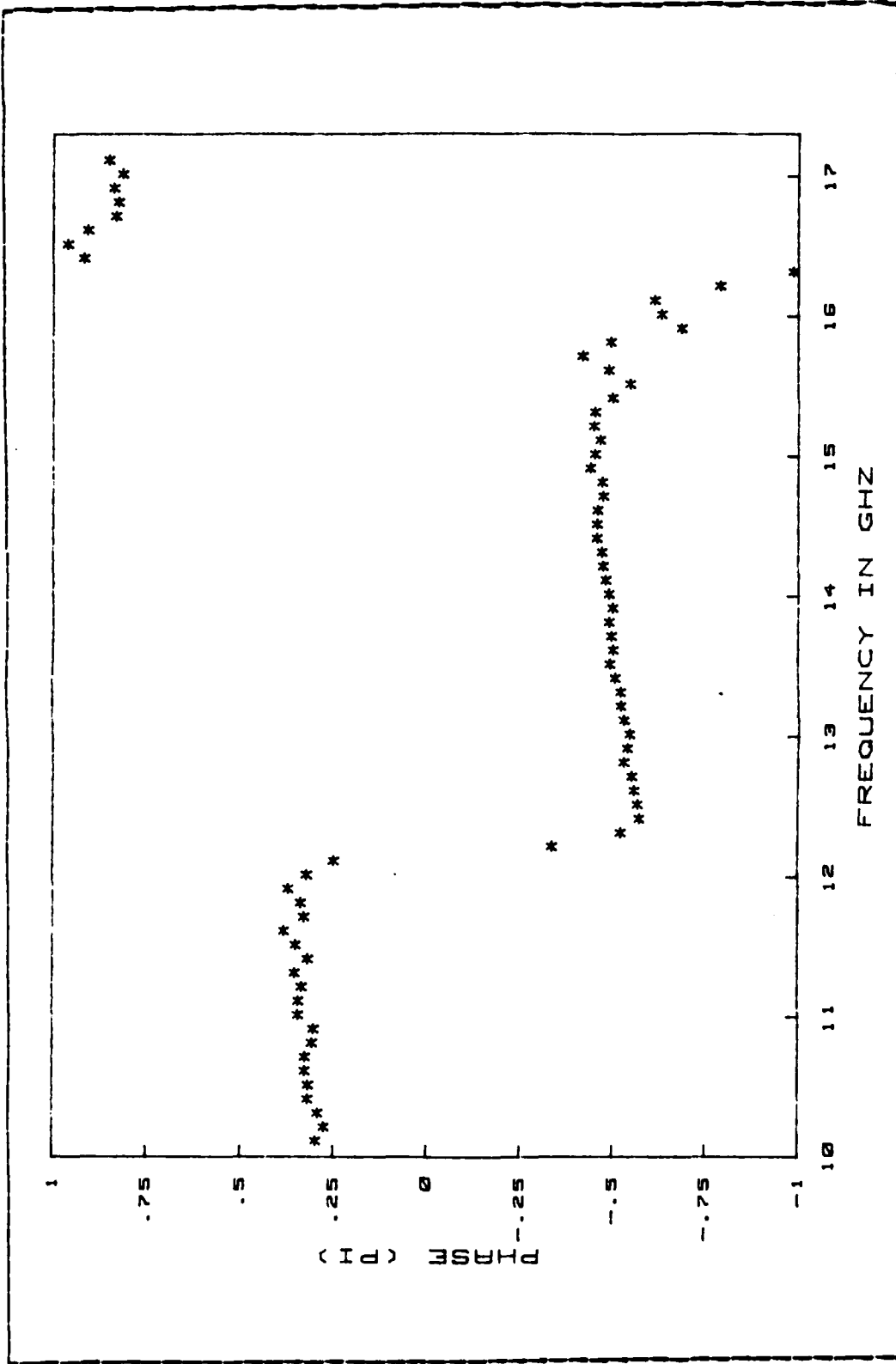


Figure 2.20 Head-on Phase Shift of Cylinder 8.

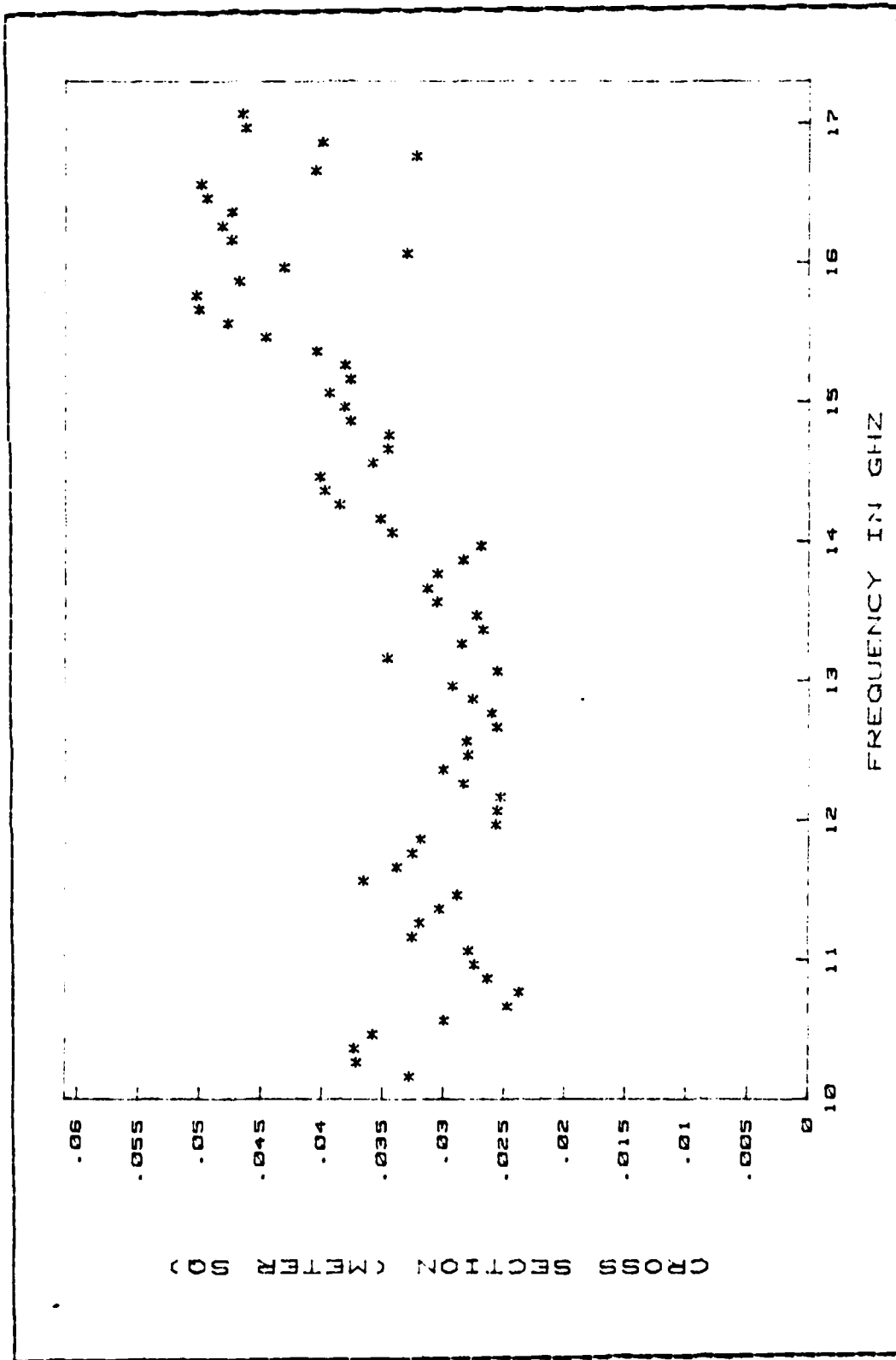


Figure 2.21 Broadside Cross Section of Cylinder 1.

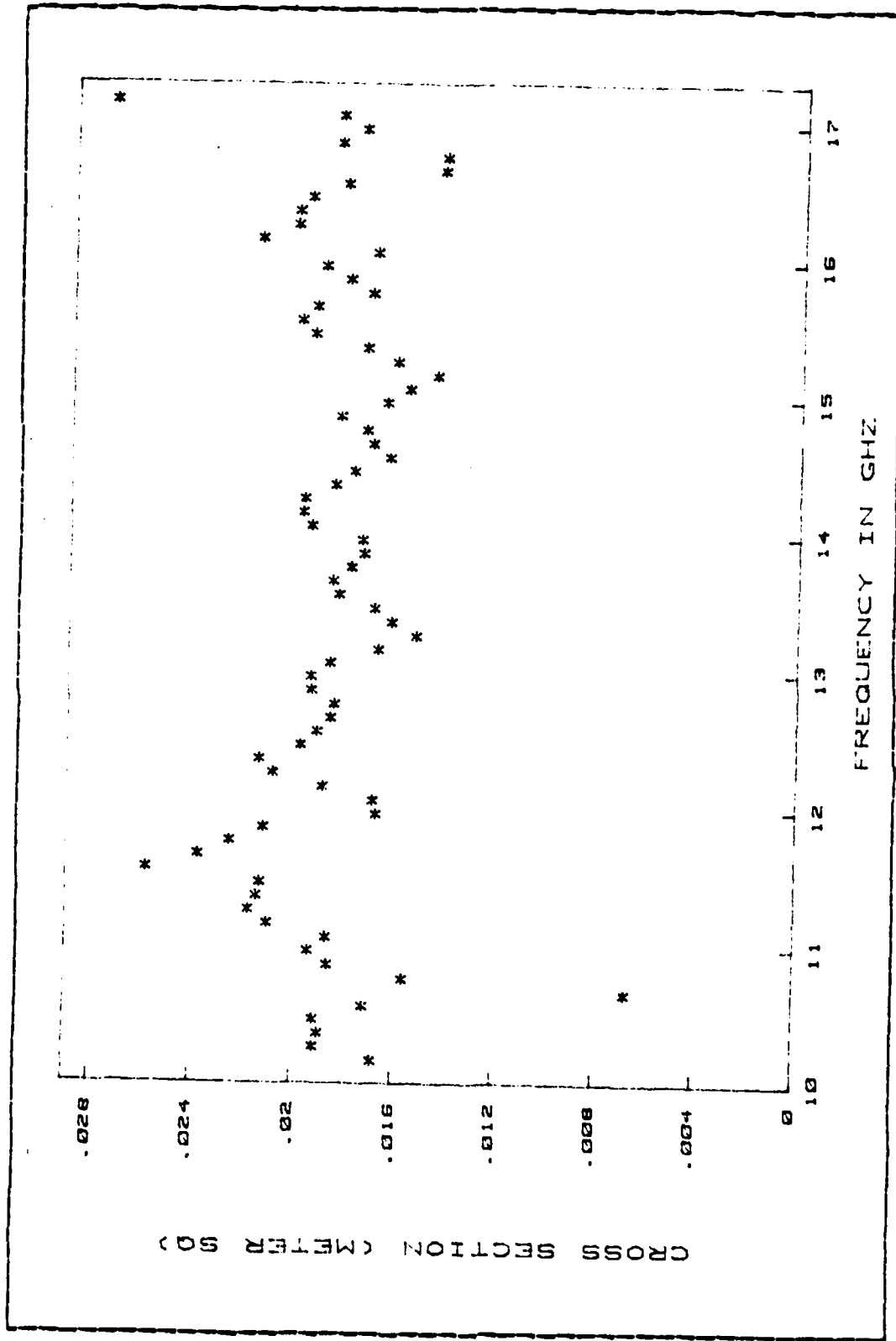


Figure 2.22 Broadside Cross Section of Cylinder 2.

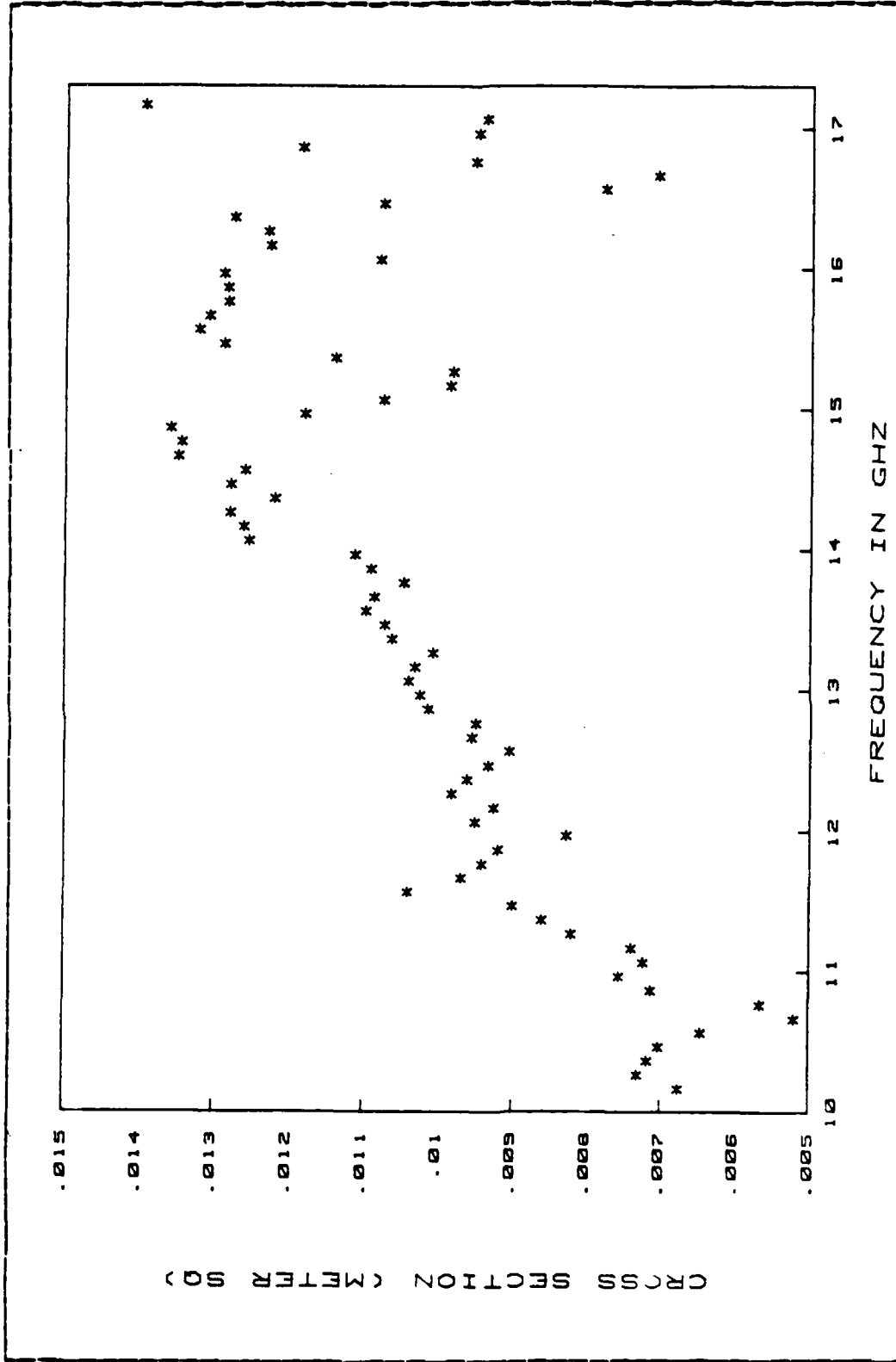


Figure 2.23 Broadside Cross Section of Cylinder 3.

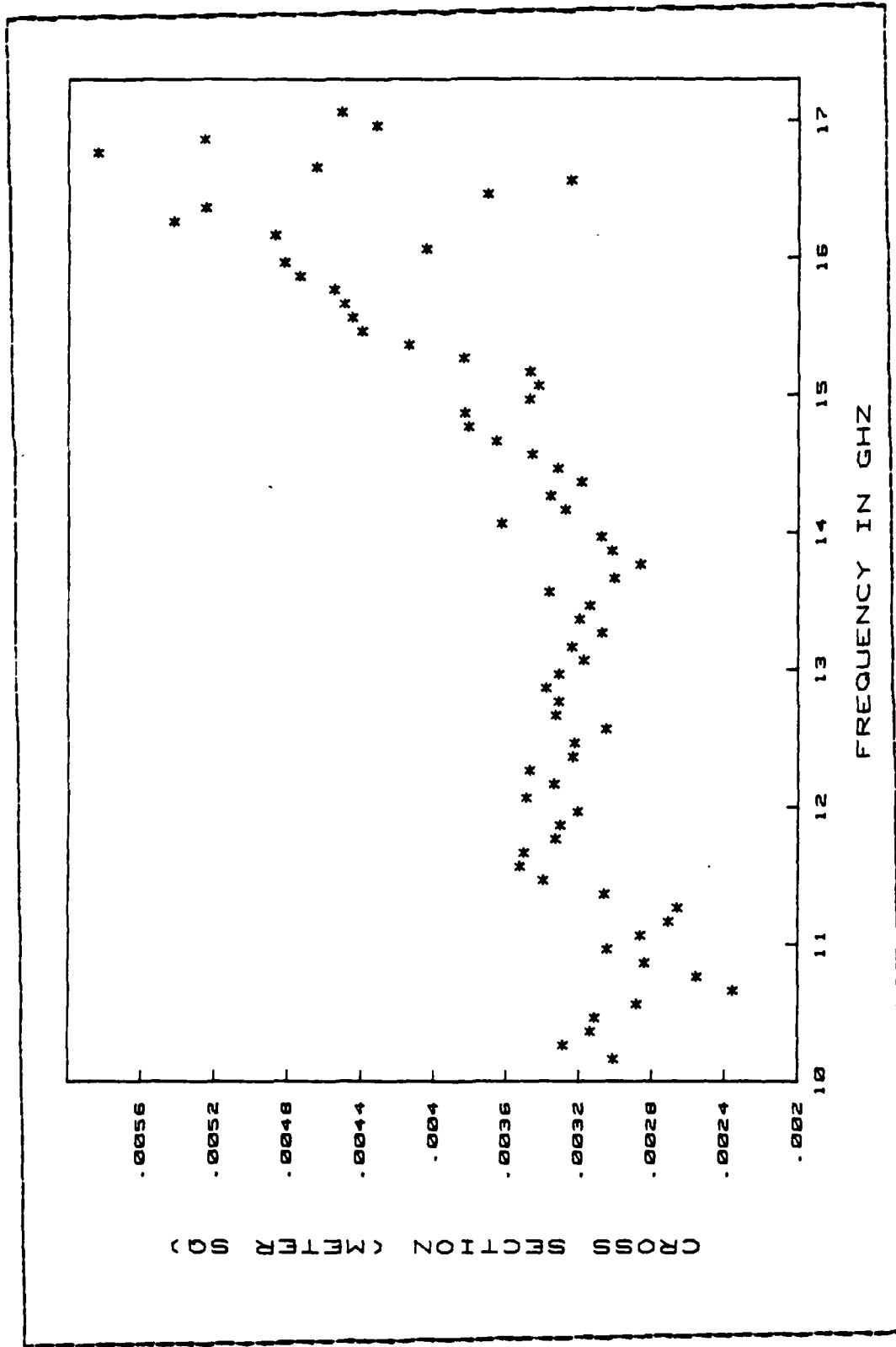


Figure 2.24 Broadside Cross Section of Cylinder 4.

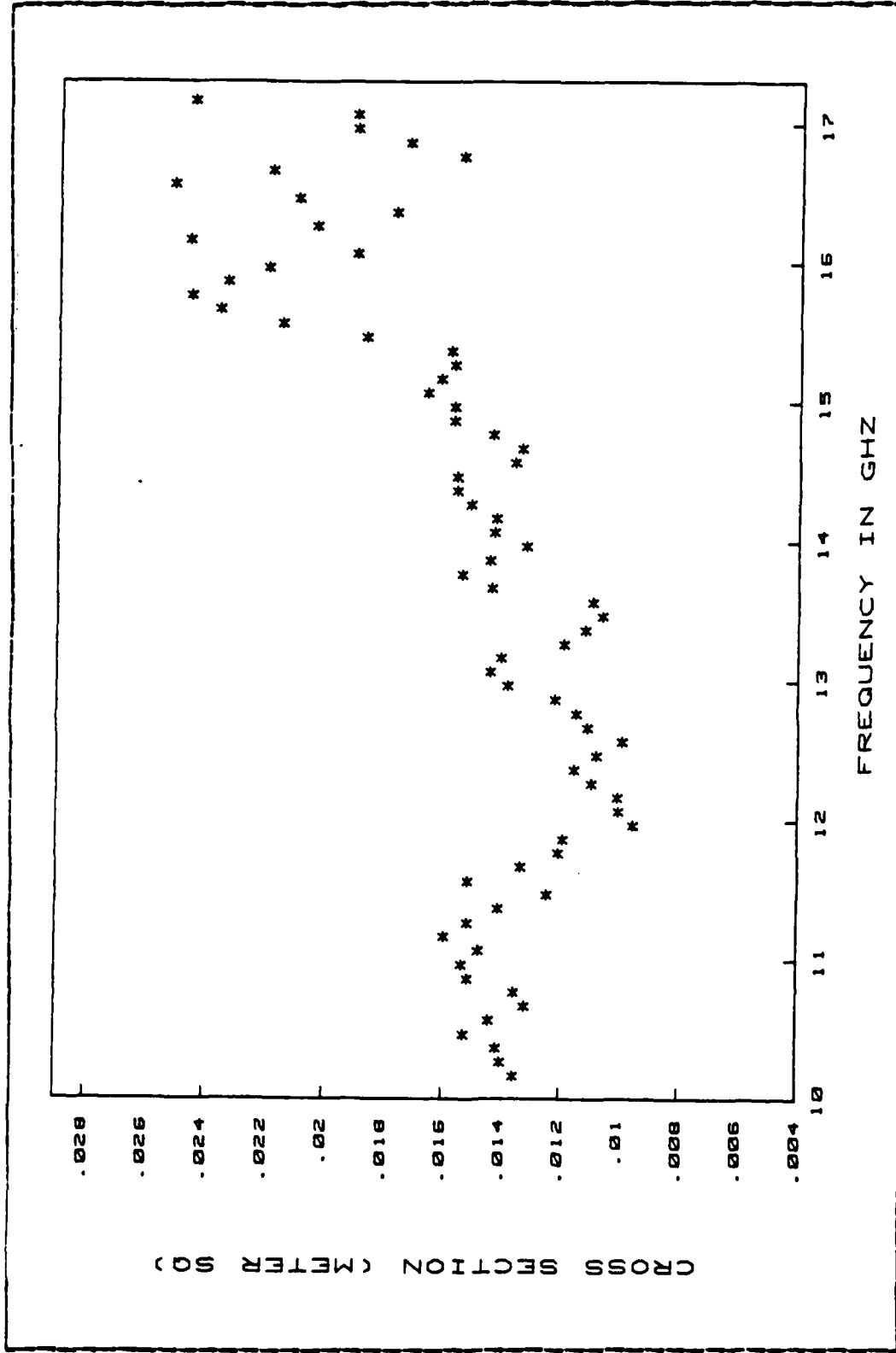


Figure 2.25 Broadside Cross Section of Cylinder 5.

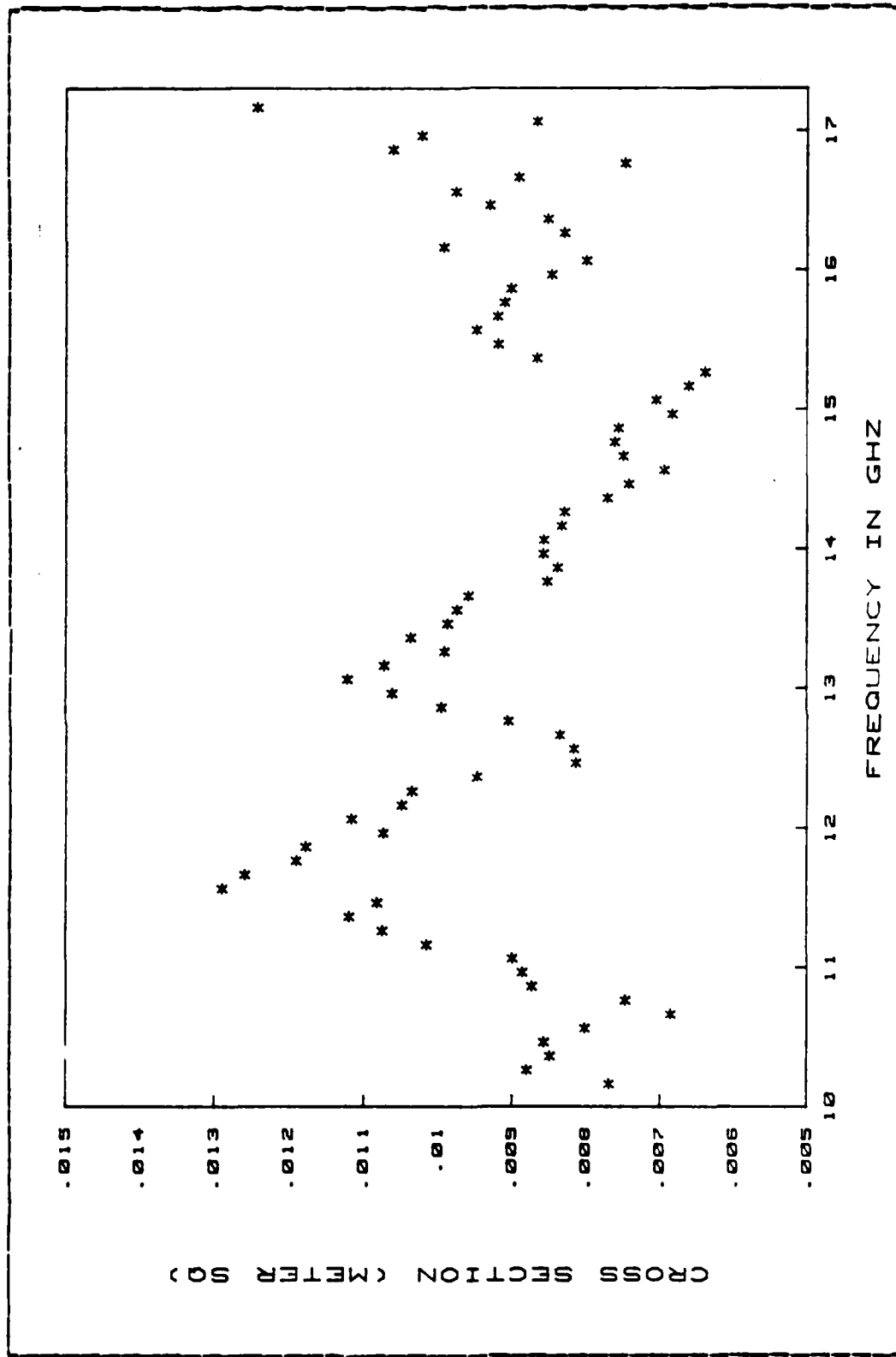


Figure 2.26 Broadside Cross Section of Cylinder 6.

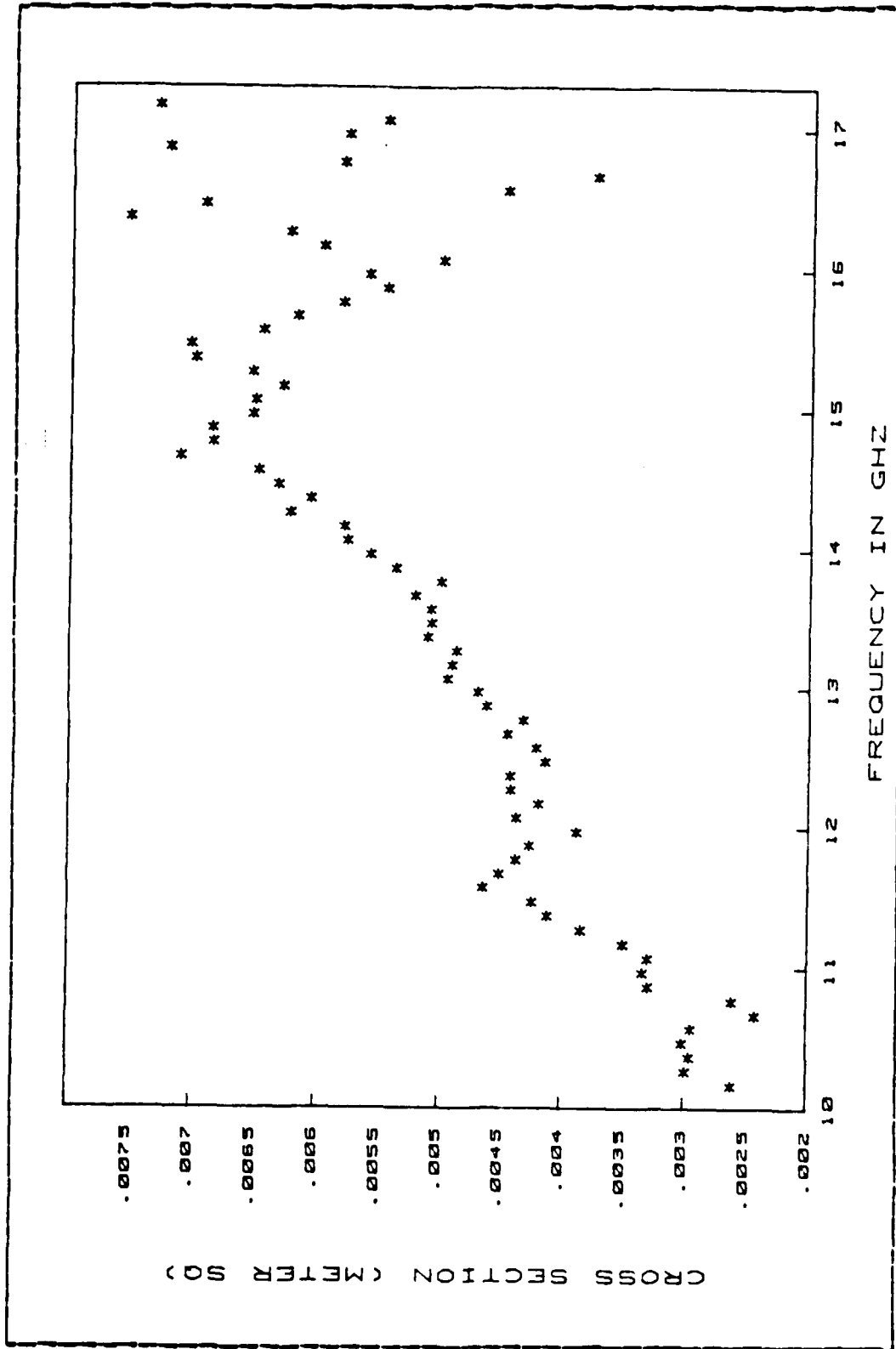


Figure 2-27 Broadside Cross Section of Cylinder 7.

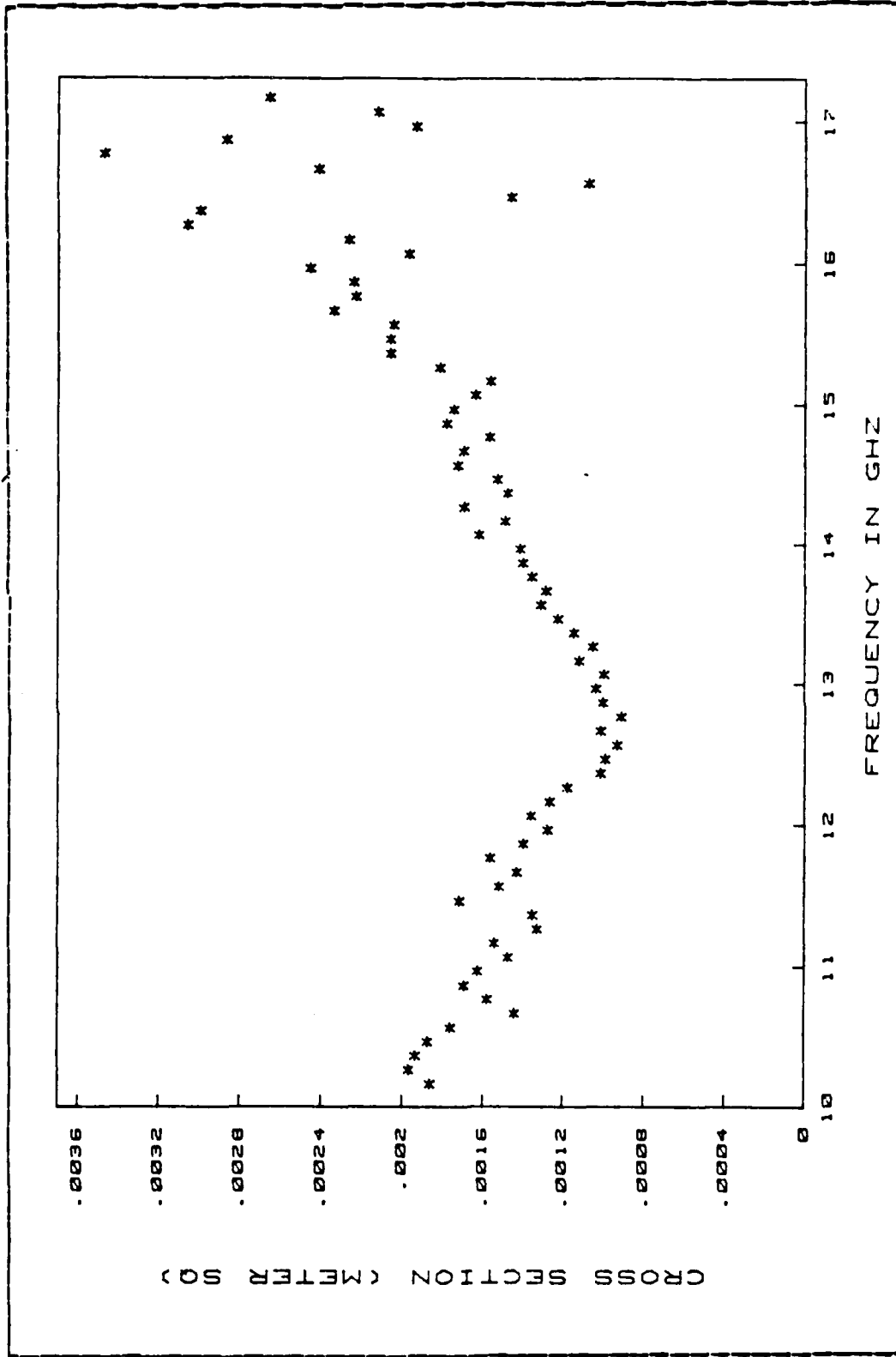


Figure 2.28 Broadside Cross Section of Cylinder 8.

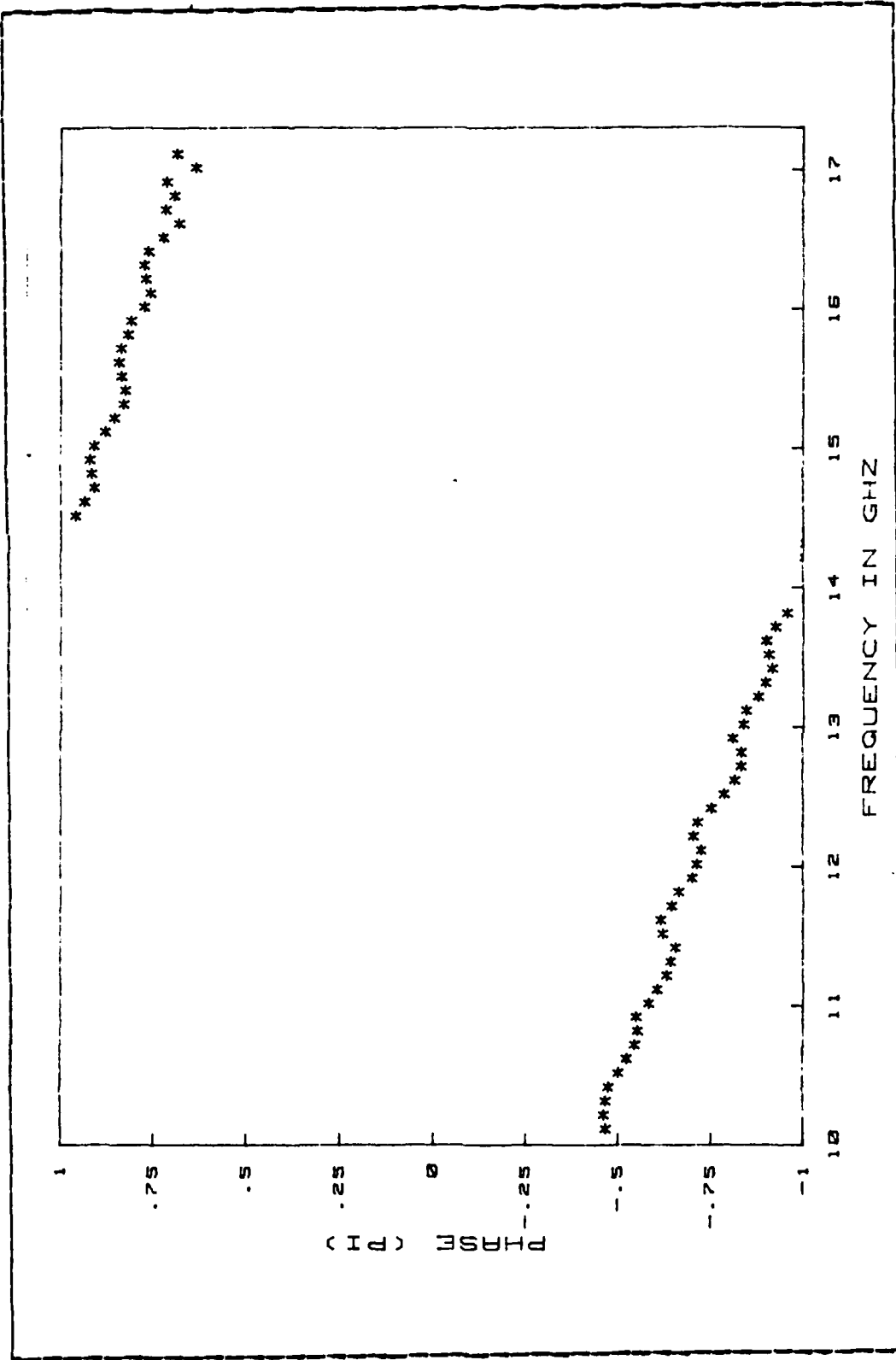


Figure 2.29 Broadside Phase Shift of Cylinder 1.

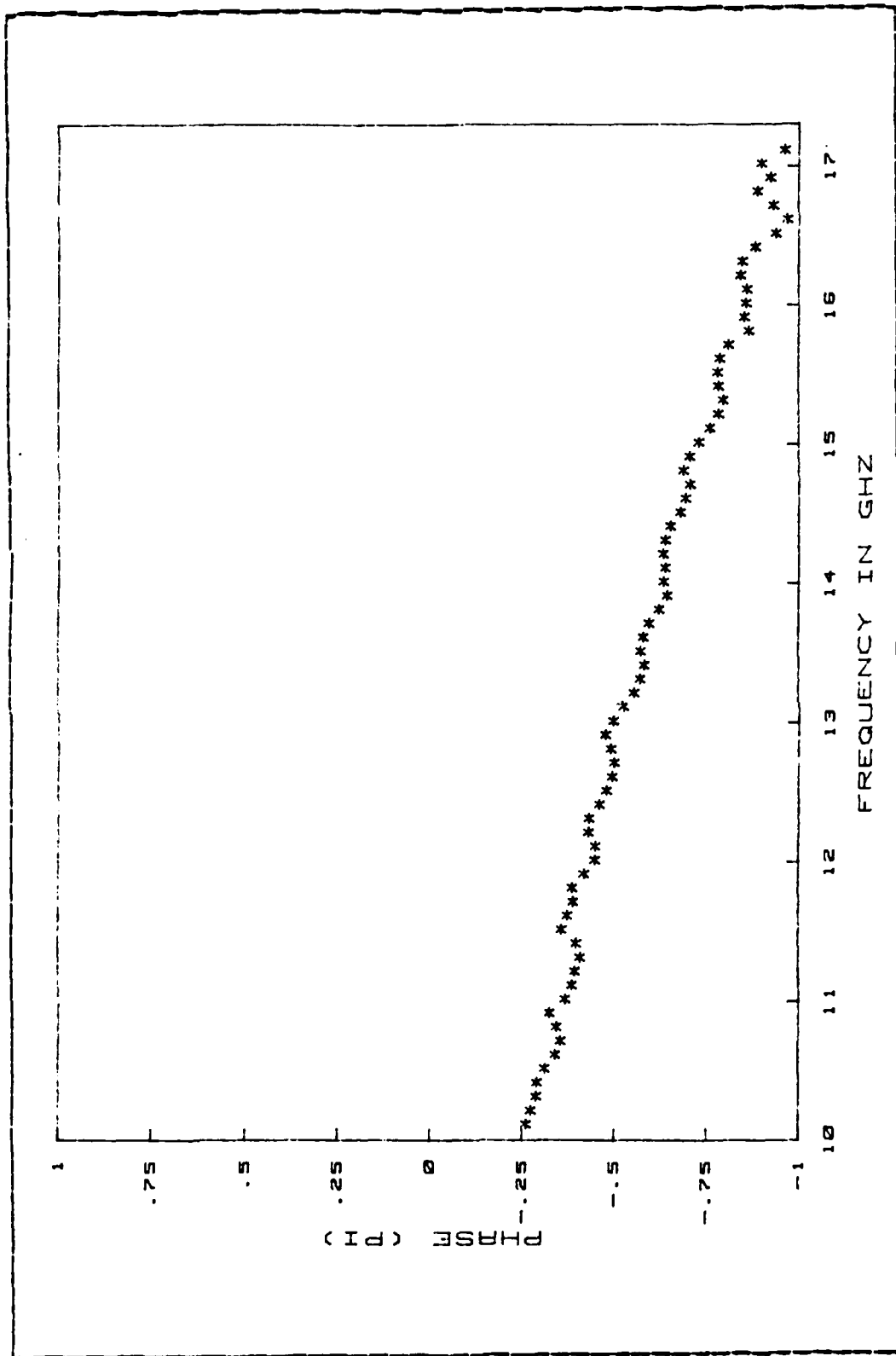


Figure 2.30 Broadside Phase Shift of Cylinder 2.

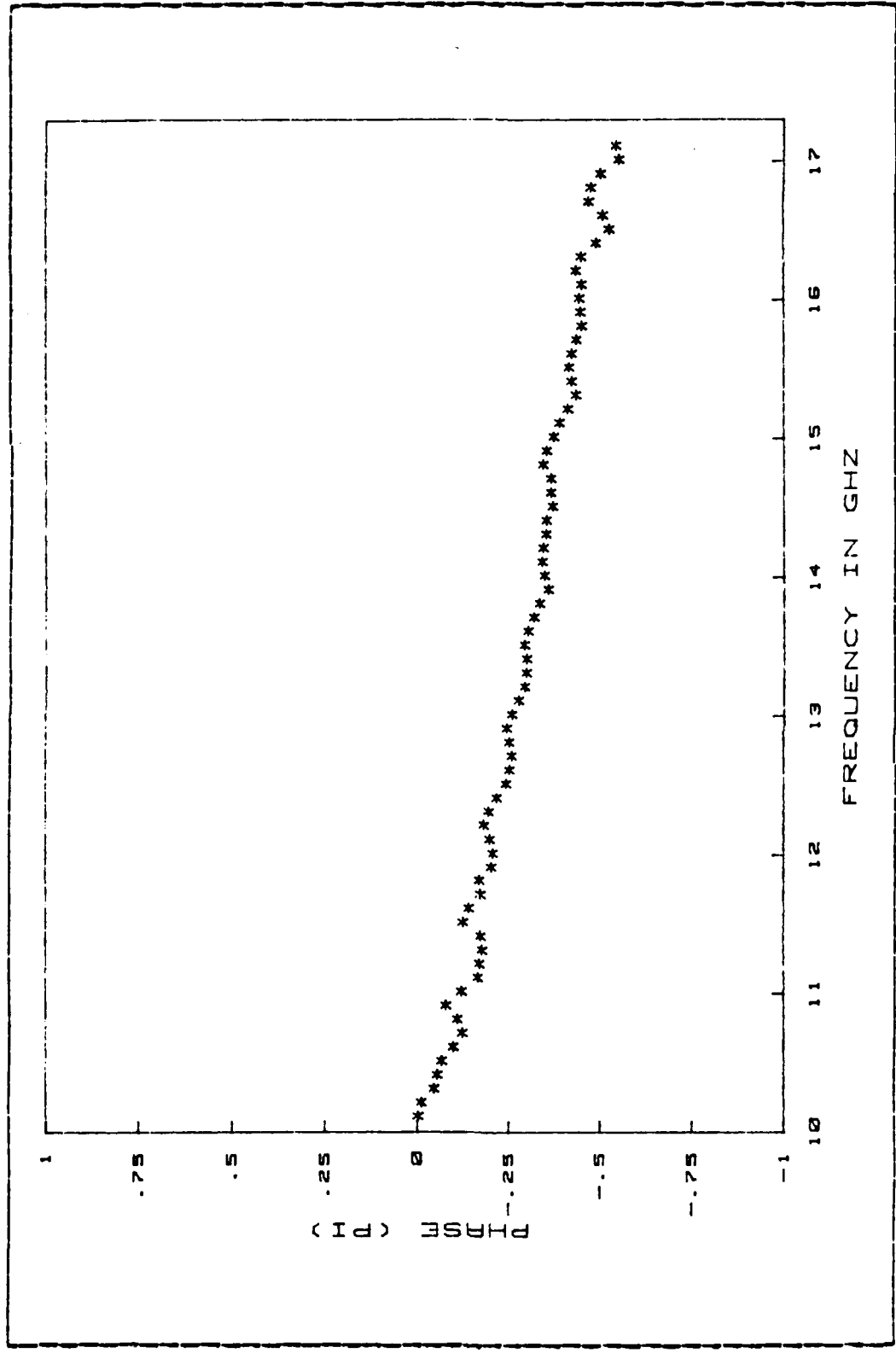


Figure 2.31 Broadside Phase Shift of Cylinder 3.

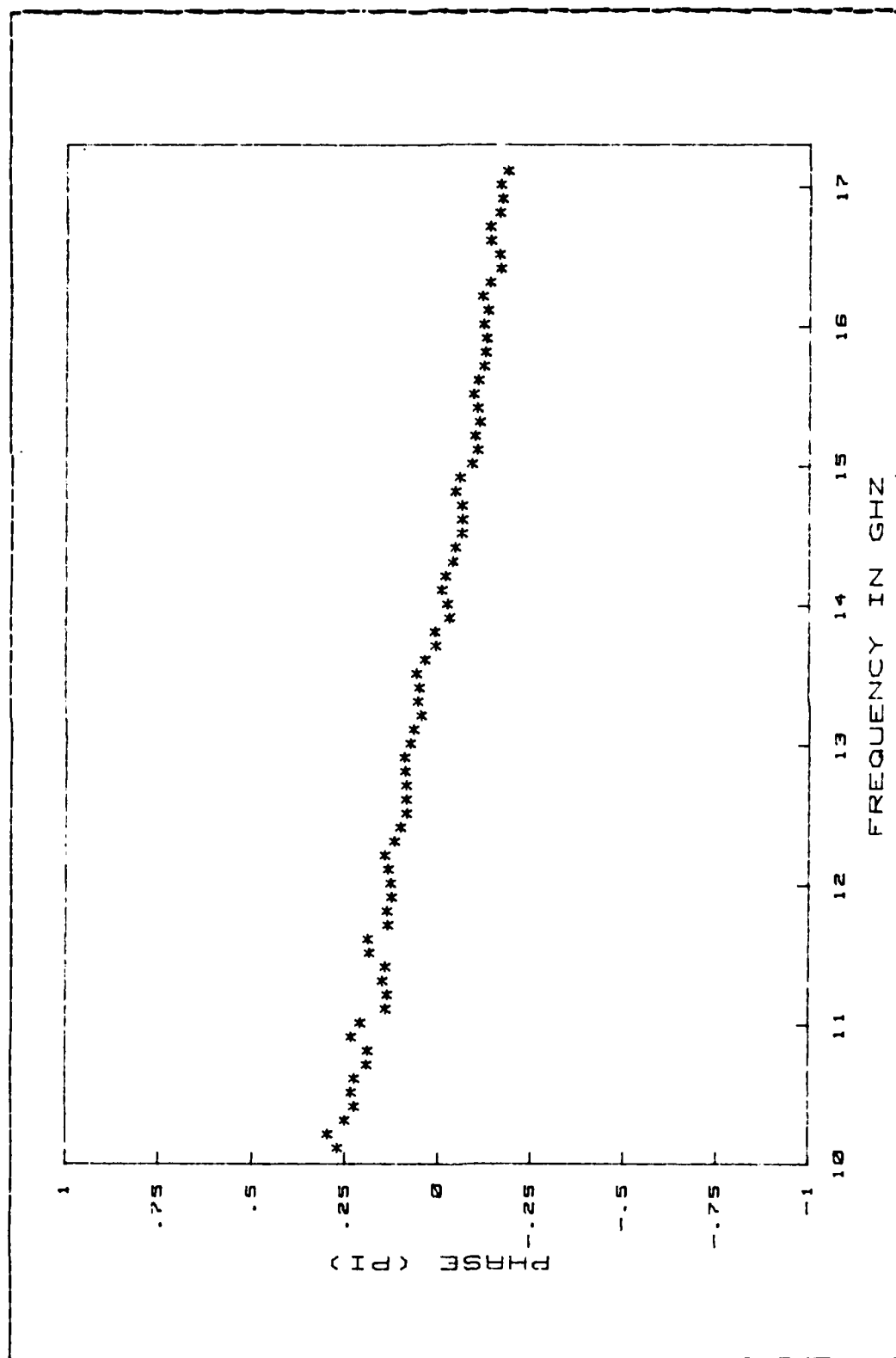


Figure 2.32 Broadside Phase Shift of Cylinder 4.

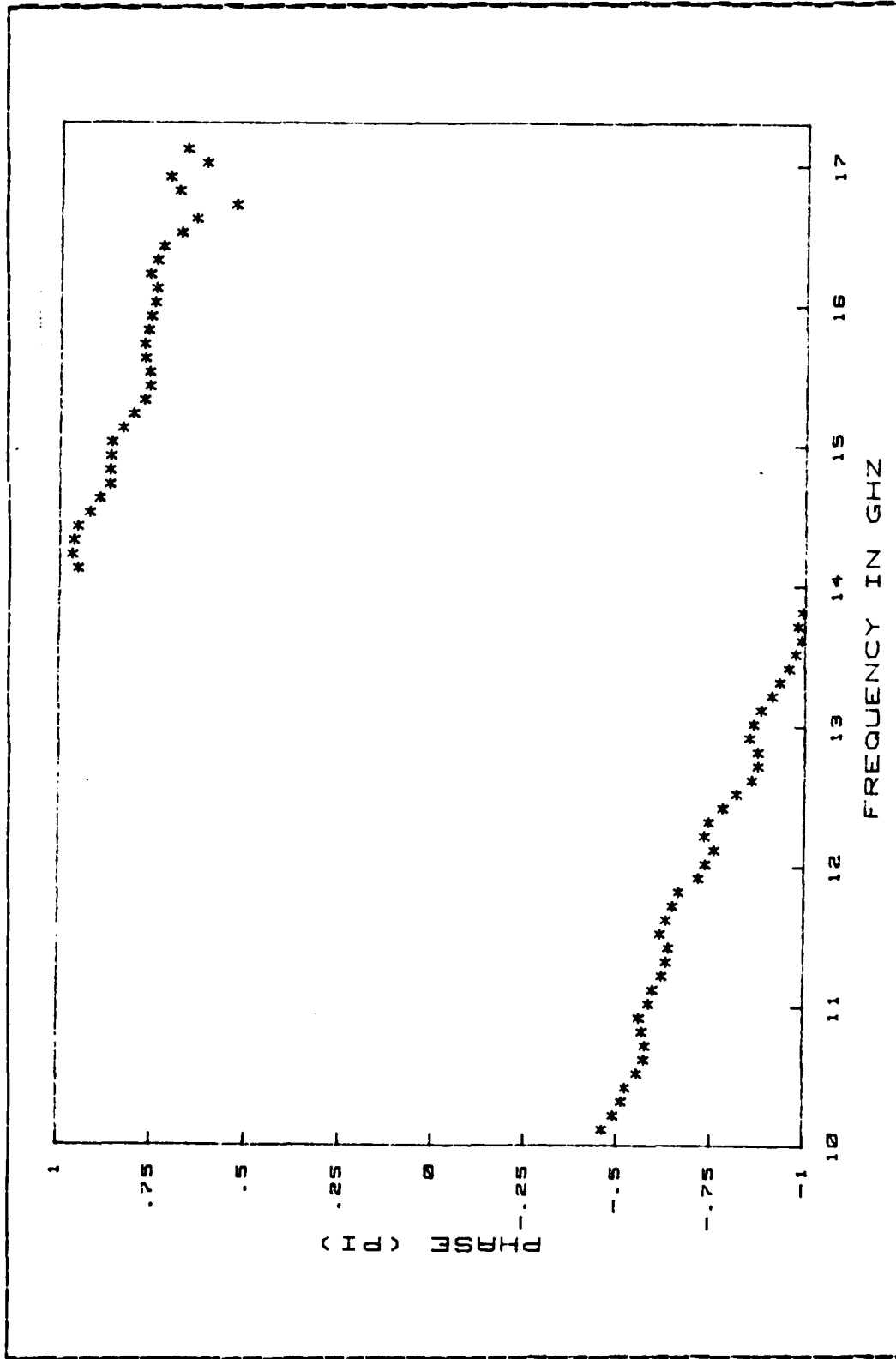


Figure 2.33 Broadside Phase Shift of Cylinder 5.

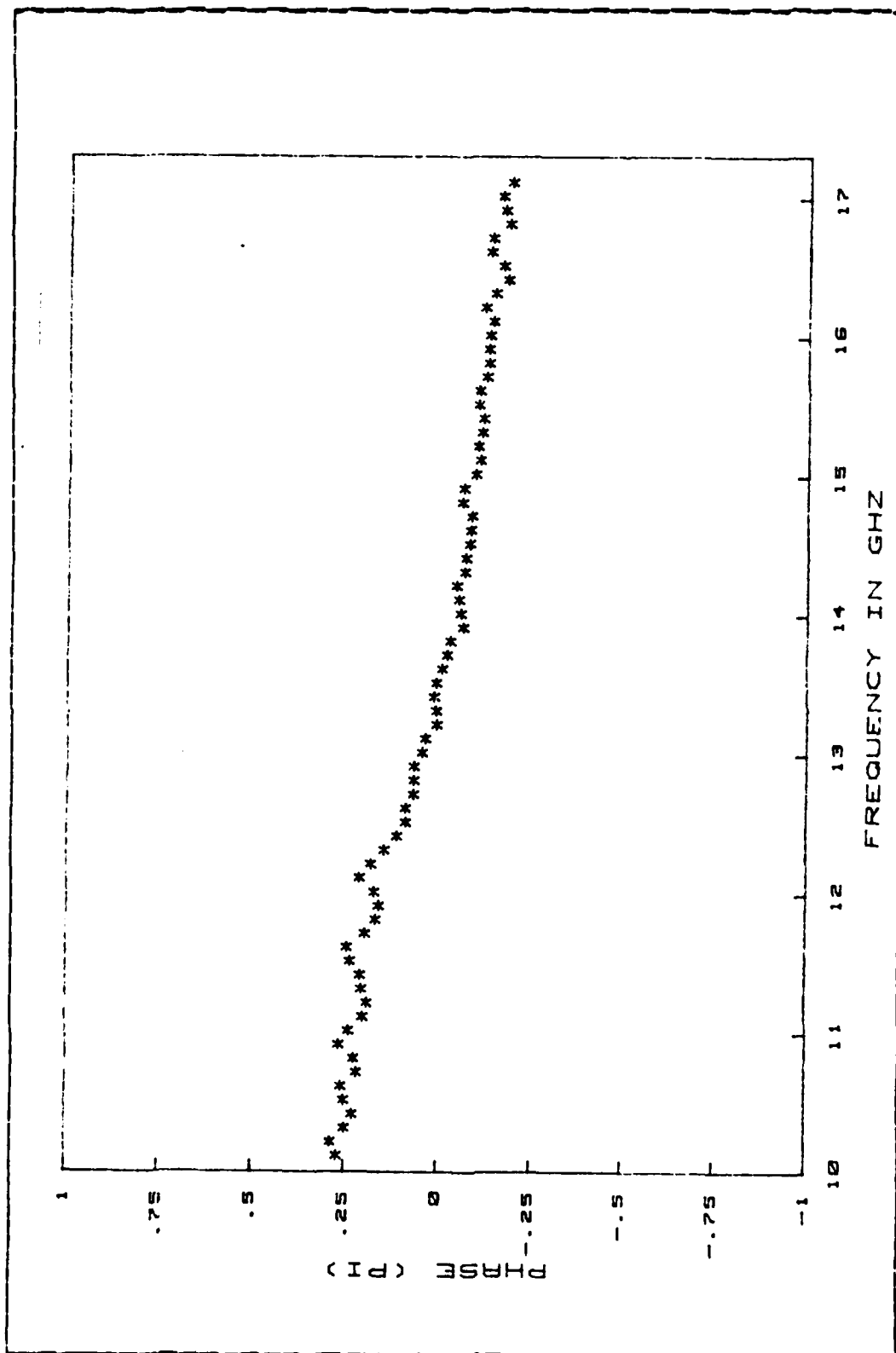


Figure 2.34 Broadside Phase Shift of Cylinder b.

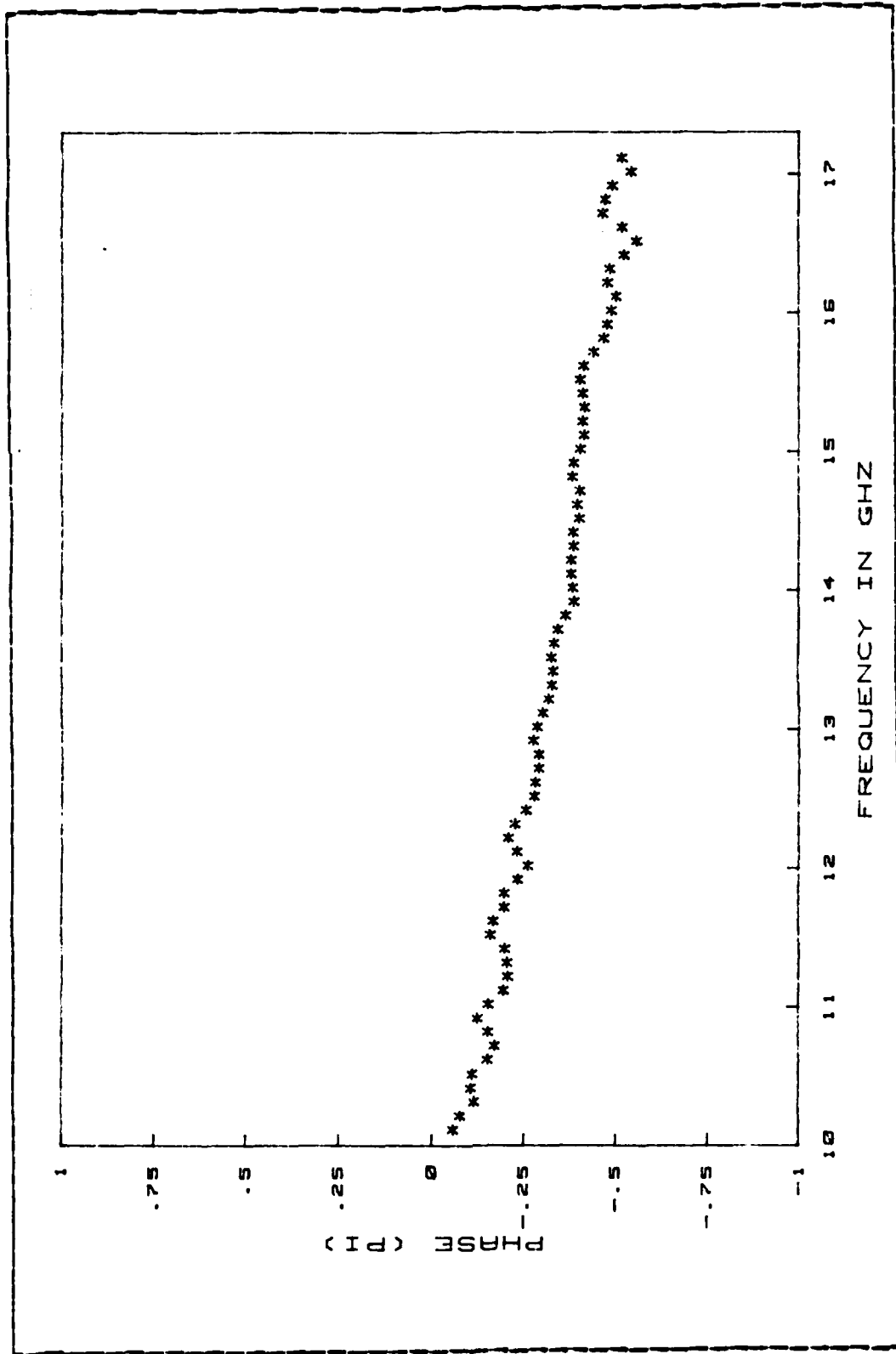


Figure 2.35 Broadside Phase Shift of Cylinder 7.

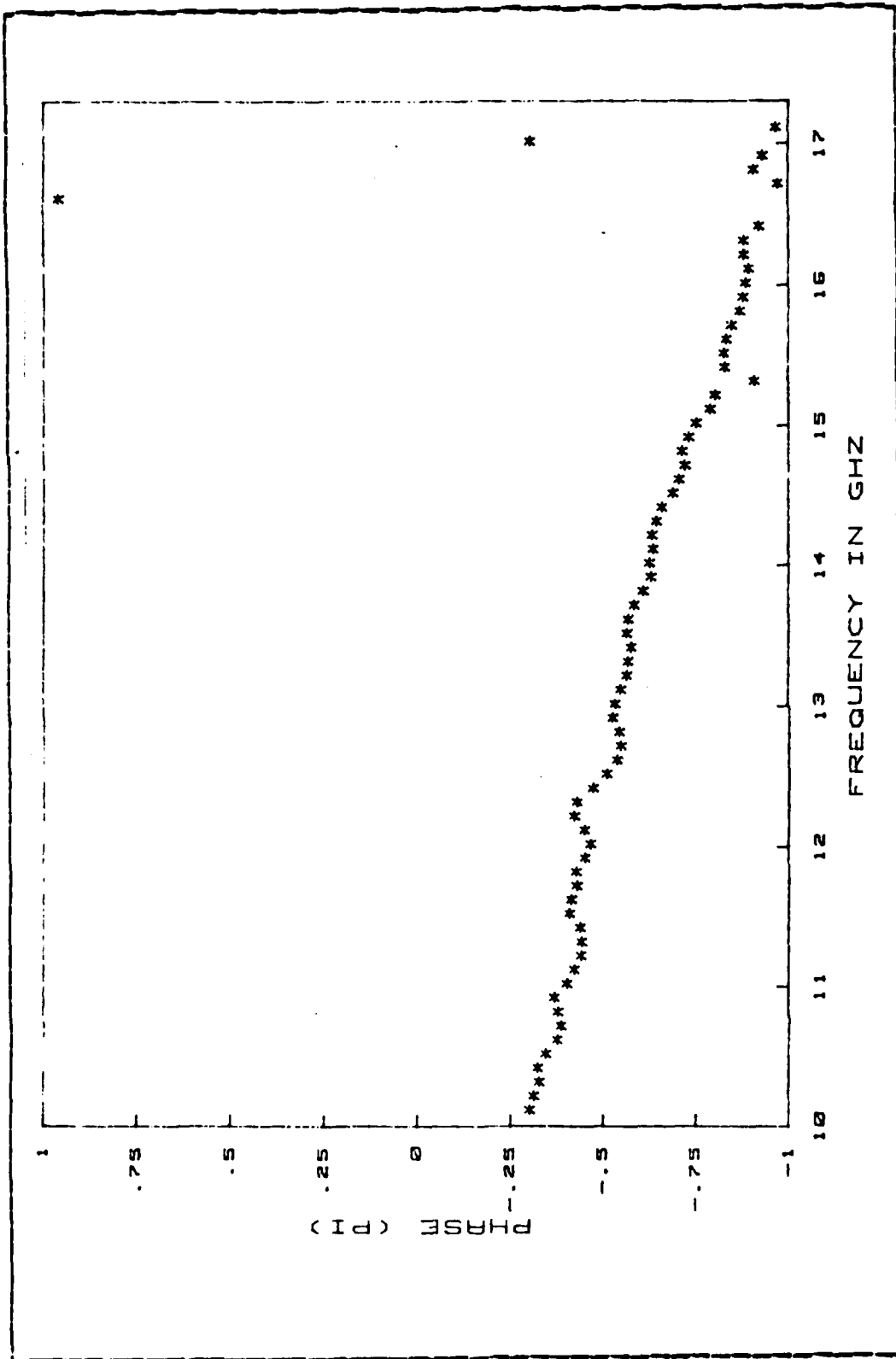


Figure 2.36 Broadside Phase Shift of Cylinder 8.

### III. ANALYSIS OF EXPERIMENTAL DATA

#### A. THEORETICAL BACKGROUND

Data of back scattered electric fields from tubular cylinders were collected and plotted as cross sections and phase shifts versus frequency. The physical meaning of these quantities are discussed in this section.

As shown in Figure 1.1, the wave incident at the target is assumed to be a plane wave and the scattered field of interest is the far field radiated by the target. In terms of the linear polarization vectors  $\hat{i}_1$ ,  $\hat{i}_2$ ,  $\hat{s}_1$ ,  $\hat{s}_2$  of the incident wave and the scattered wave respectively, the incident field at the target center (origin of the coordinate system) is a constant vector and can always be written as:

$$\vec{E}^i = E_1(\hat{k}^i)\hat{i}_1 + E_2(\hat{k}^i)\hat{i}_2$$

The scattered wave, in the far field, can be written as:

$$\vec{E}^s(\hat{r}) = \frac{e^{ikr}}{r} [a_1(\hat{r})\hat{s}_1 + a_2(\hat{r})\hat{s}_2]$$

where  $\hat{r}$  gives the angular dependence of the scattered wave. Note that the choice of  $\hat{i}_1$  and  $\hat{i}_2$  is arbitrary to the extent that  $\hat{i}_1 \cdot \hat{k}^i = 0$  and  $\hat{i}_2 = \hat{k}^i \times \hat{i}_1$ . Similar relations hold between  $\hat{s}_1$ ,  $\hat{s}_2$  and  $\hat{r}$ . Since the polarization of any wave propagating in the  $\hat{k}^i$  direction can be written in terms of linear combinations of the vectors  $\hat{i}_1$  and  $\hat{i}_2$ , these two components can be considered separately. Similarly, in the direction  $\hat{r}$ , the scattered far field can always be written as a linear combination of the vectors  $\hat{s}_1$  and  $\hat{s}_2$ . Thus the cross section and phase shift of the scattered field polarized along the  $\hat{s}_1$  direction is given when the incident wave is polarized along the  $\hat{i}_1$  direction and of unit strength and zero phase at the target center, as:

$$\sigma_{lm}(\hat{r}, \hat{k}^i) = 4\pi |a_l(\hat{r})|^2 \quad \text{and} \quad \delta_{lm}(\hat{r}, \hat{k}^i) = \arg[a_l(\hat{r})]$$

where  $l, m = 1, 2$ . When  $\hat{r} = -\hat{k}$ , the cross section is the back scattering cross section. With the polarization understood, and with discussions concentrated in back scattering, the subscripts and the arguments will be dropped henceforth. The integrodifferential equations governing the surface current distribution can be set up as equations 3.1 through 3.3

$$\begin{aligned} & \left( 1 + \frac{1}{k_1^2} \frac{\partial^2}{\partial z^2} \right) \int_{-1}^1 dz_0 K_{zn}(z_0) G_n(k_1 |z-z_0|, k_2) \\ & + \frac{in}{k_1 k_2} \frac{\partial}{\partial z} \int_{-1}^1 dz_0 K_{en}(z_0) G_n(k_1 |z-z_0|, k_2) \\ & = - \frac{2i}{k_1 k_2 \epsilon_0} E_{zn}^{sc}(z) \end{aligned}$$

(eqn 3.1)

$$\begin{aligned} & \int_{-1}^1 dz_0 K_{en}(z_0) \left\{ \frac{1}{2} [G_{n-1}(k_1 |z-z_0|, k_2) \right. \\ & \left. + G_{n+1}(k_1 |z-z_0|, k_2)] - \frac{n^2}{k_2^2} G_n(k_1 |z-z_0|, k_2) \right\} \\ & + \frac{in}{k_1 k_2} \frac{\partial}{\partial z} \int_{-1}^1 dz_0 K_{zn}(z_0) G_n(k_1 |z-z_0|, k_2) \\ & = - \frac{2i}{k_1 k_2 \epsilon_0} E_{en}^{sc}(z) \end{aligned}$$

(eqn 3.2)

$$E_{zn}^{SC}(z) + E_{zn}^i(z) = 0, \quad E_{\phi n}^{SC}(z) + E_{\phi n}^i(z) = 0$$

for  $-1 < z < 1$

(eqn 3.3)

where  $l_1 = kh$ ,  $l_2 = ka$ .  $2h$  is the length of the cylinder.  $a$  is the radius of the idealized cylinder of zero wall thickness. The components of the surface current are represented as equations 3.4 and 3.5 in which the edge conditions are satisfied term by term in the representation. The computation was carried out by Lee [Refs. 4,5].

$$\begin{aligned} K_z(\phi, z) &= \sum_{n=-\infty}^{\infty} e^{in\phi} K_{zn}(z) \\ &= \frac{1}{\pi} \sum_{n=-\infty}^{\infty} e^{in\phi} \sum_{p=0}^{\infty} K_{zn}^p \sin(p+1)v \end{aligned} \quad (\text{eqn 3.4})$$

$$\begin{aligned} K_\phi(\phi, z) &= \sum_{n=-\infty}^{\infty} e^{in\phi} K_{\phi n}(z) \\ &= \frac{1}{\pi \sin v} \sum_{n=-\infty}^{\infty} e^{in\phi} \sum_{p=0}^{\infty} K_{\phi n}^p \cos pv \end{aligned} \quad (\text{eqn 3.5})$$

It is clear from equations 3.1 and 3.2 that  $(kr)E^\alpha$  depends only on  $l_1$  and  $l_2$  as  $r$  approaches infinity. Hence  $k^2\sigma$ , or equivalently,  $\sigma/\sigma_0$ , is only a function of  $l_1$  and  $l_2$ , if  $\sigma_0$  is a function of the length and the diameter of the cylinder which has the dimensions of area. This property is the basis for frequency scaling of targets in air. In this thesis,  $\sigma_0$  is chosen to be the projected physical cross sectional area of the cylinder along the direction of the incident wave. In what follows, data from head-on scattering of the cylinders will be analyzed. For this case,  $\sigma_0$  equals  $\pi(a^+)^2$

where  $a^+$  is the outer radius of the cylinder. The broadside case will be discussed in Chapter IV. In which case,  $\sigma_c$  is  $4ha^+$ .

#### B. COMPARISON BETWEEN THEORY AND EXPERIMENT

Throughout the following figures,  $2h/\lambda$  is used as the variable. The ordinates are either cross section divided by the projected area or phase shift in units of  $\pi$ . The experimental data are distributed over the  $2h/\lambda$  values from 1.4 to 6.2 for cylinders with  $h/a^+ = 6$  and 1.0 to 4.2 for cylinders with  $h/a^+ = 4$ . Cross sections from different cylinders are represented by different symbols. Experimental data points and theoretical curves for the cross section are plotted together in Figure 3.1 and Figure 3.3. For the head-on case, the agreement is obvious. Theoretical and measured phase shifts are shown together in Figure 3.2 and Figure 3.4. Deviations between measured and theoretical values and between overlapping portions of the measured data from different cylinders are evident. These deviations may be caused by the fact that the heights of the tubular cylinders on the support are different from that of the 8.095 centimeter diameter aluminum sphere used for calibration. Such differences results in different antenna to target distances which contribute to the deviations in phase.

In all the following figures, these symbols, "\*", "o", "x" and "+", were used and they represent cylinders of following diameter 1.9 cm, 1.59 cm, 1.27 cm and 0.95 cm respectively.

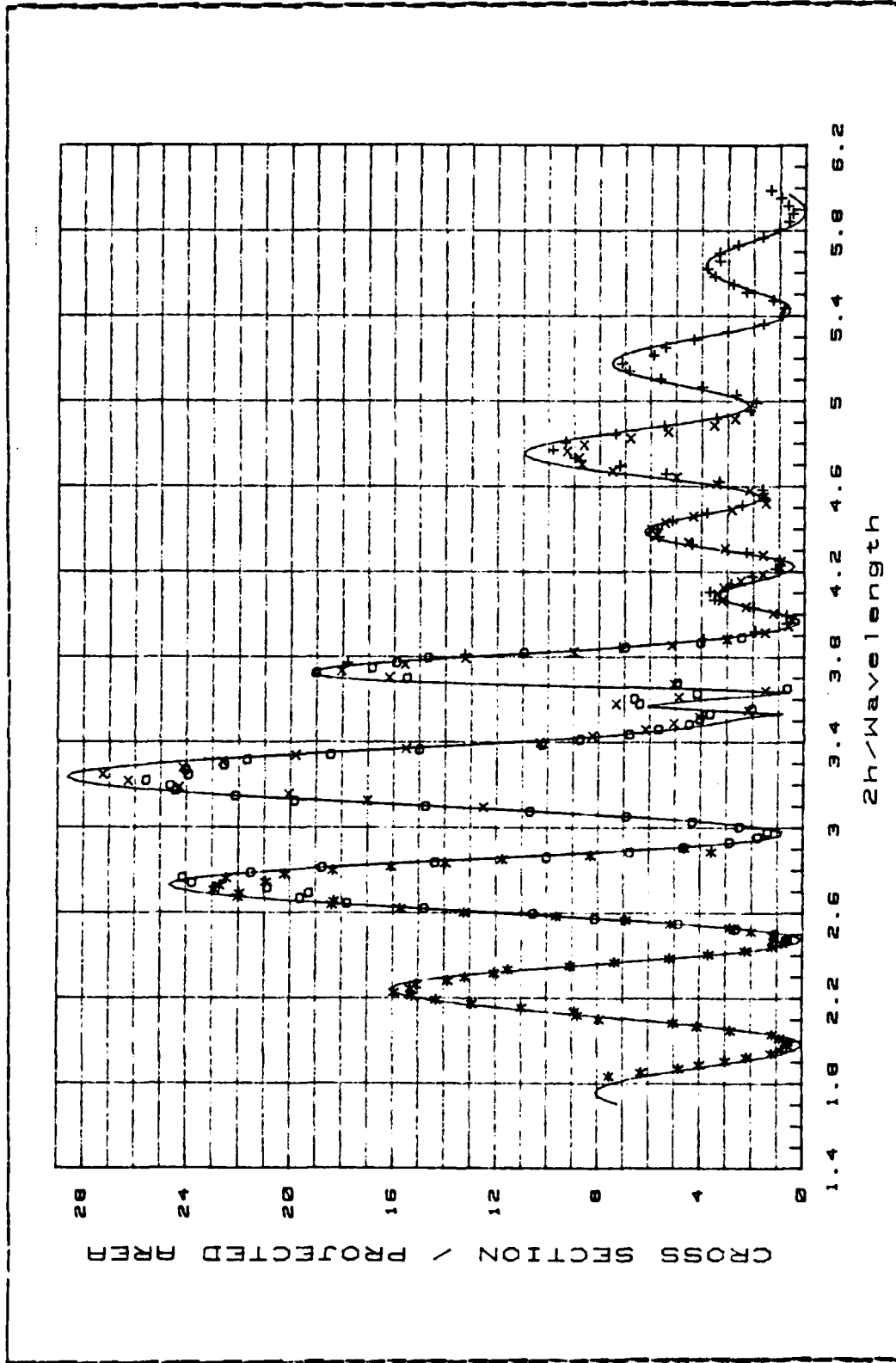


Figure 3.1 Theoretical and Measured Head-on Cross Section ( $b/a = 6$ ).

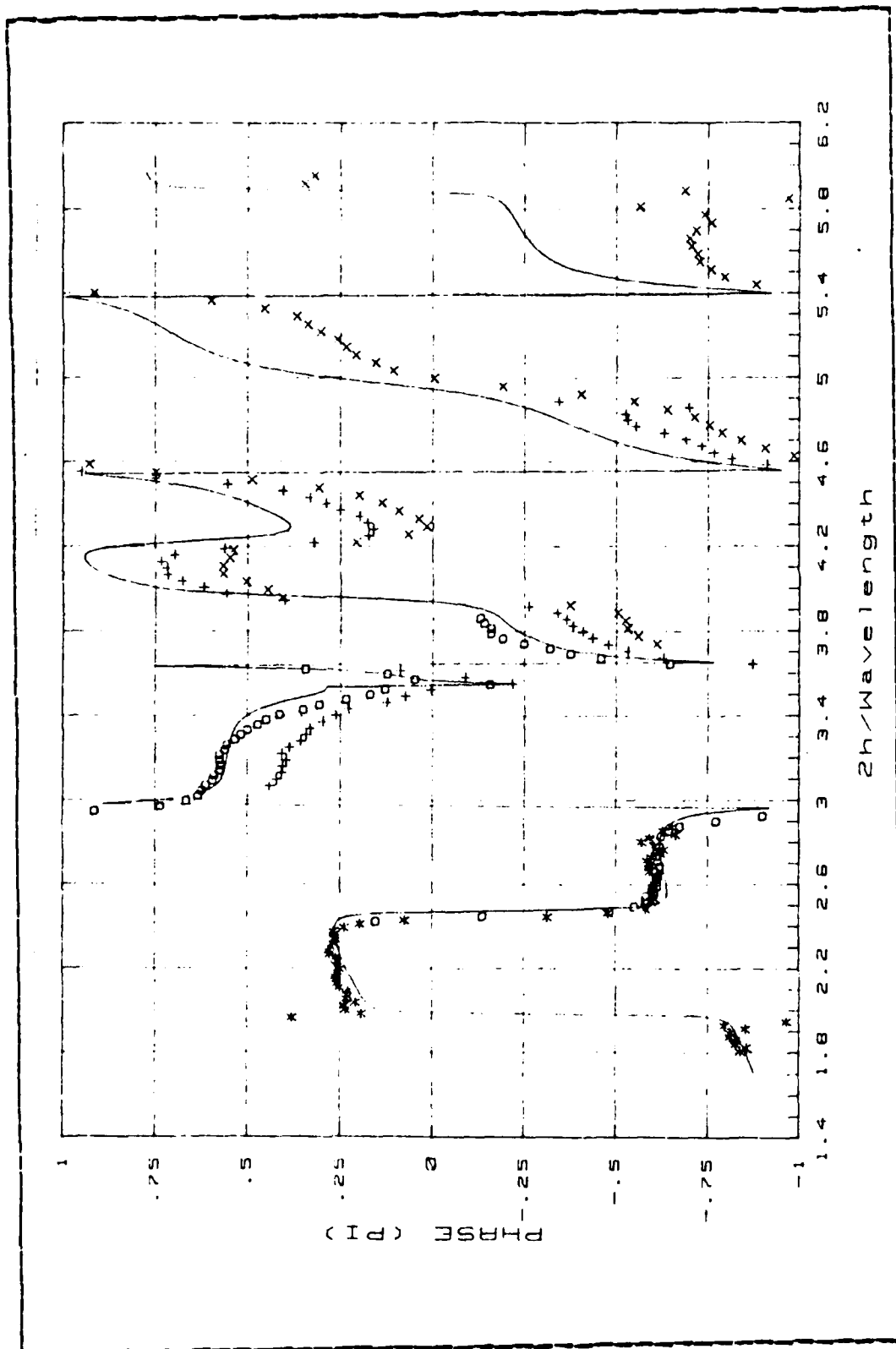


Figure 3.2 Theoretical and Measured Head-on Phase ( $h/a = 6$ ).

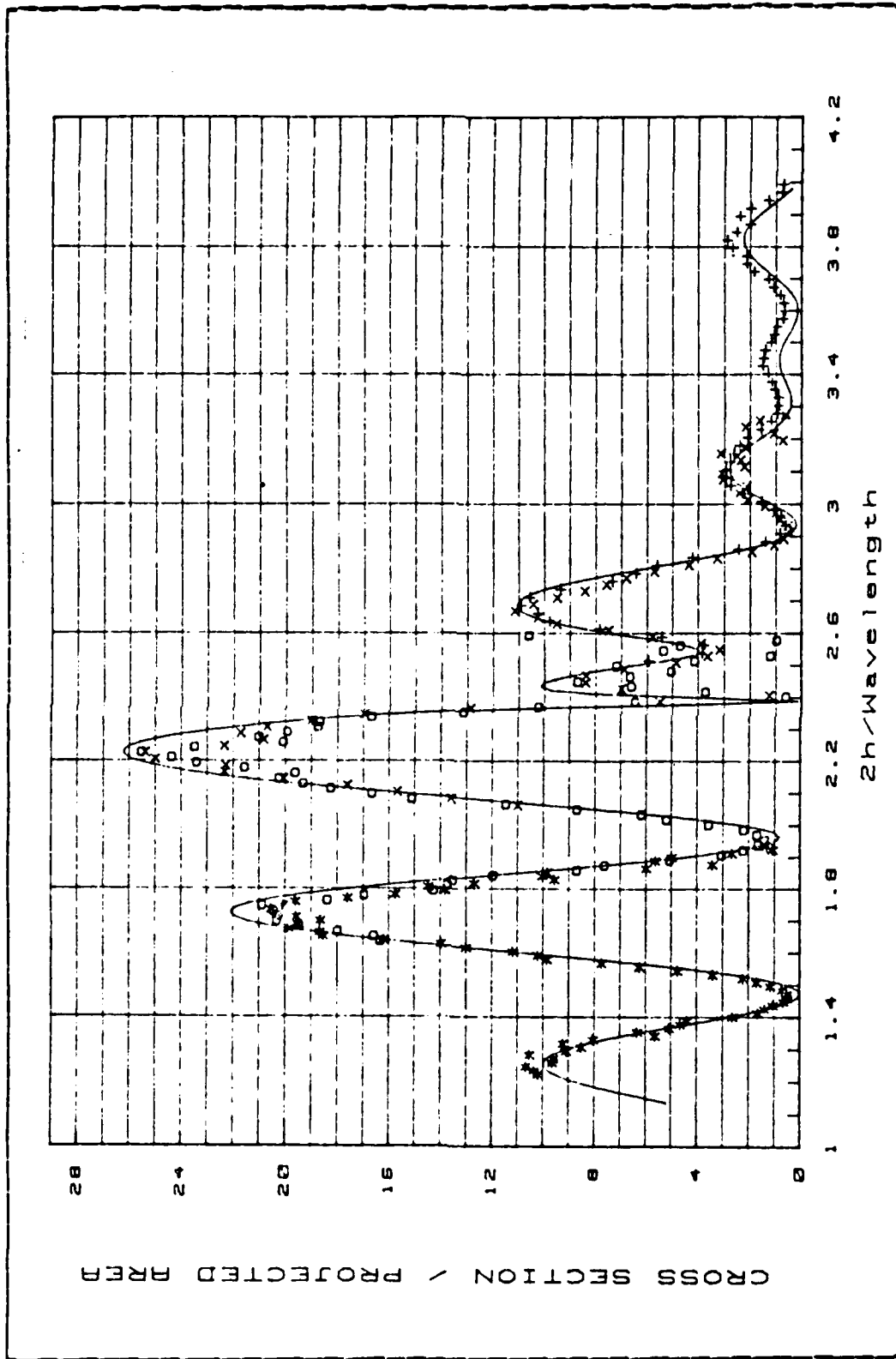


Figure 3.3 Theoretical and Measured Head-on Cross Section ( $h/a = 4$ ).

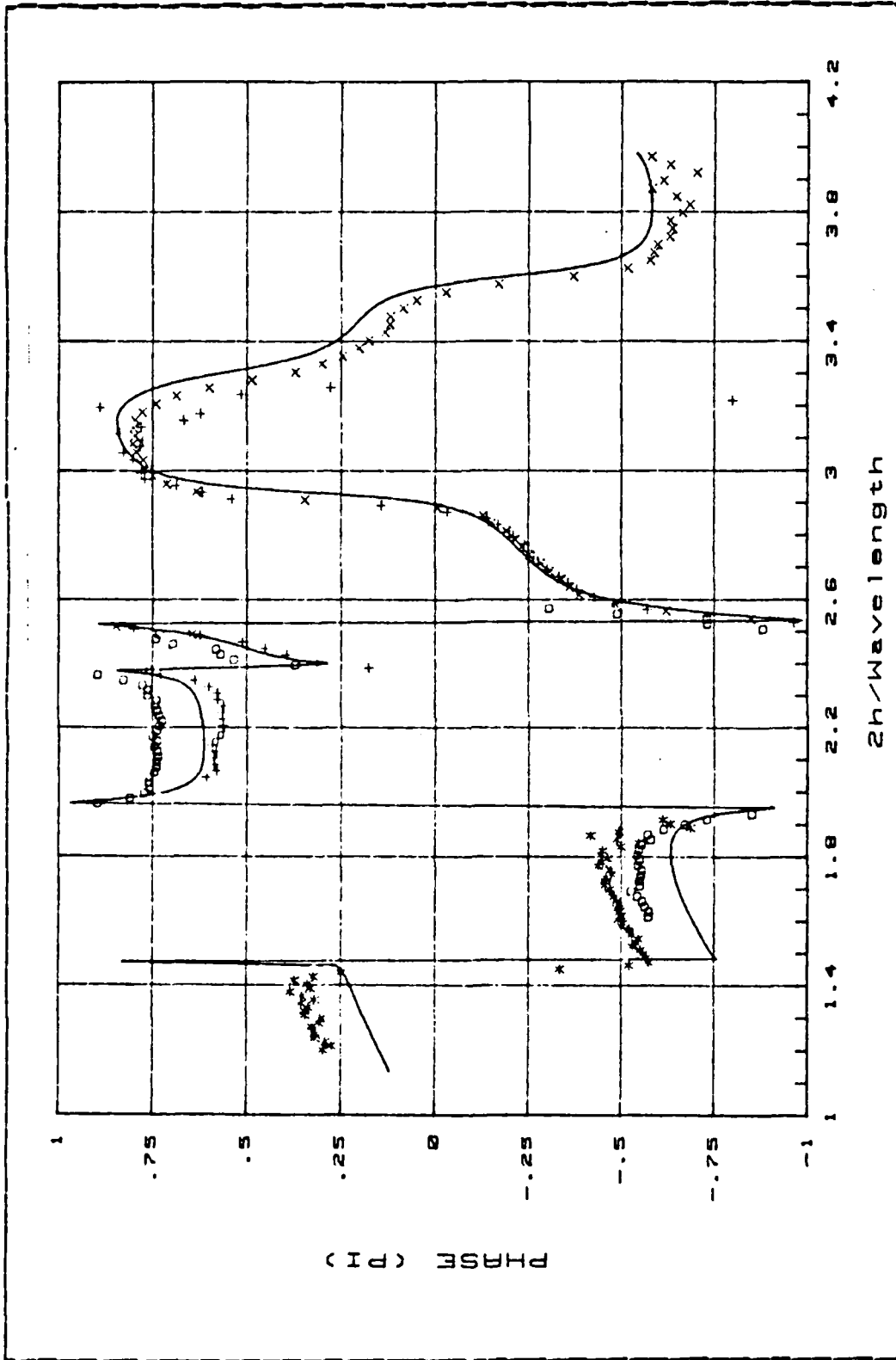


Figure 3.4 Theoretical and Measured Head-on Phase ( $h/a = 4$ ).

### C. COMPARISON BETWEEN NEW AND PREVIOUS RESULTS

Since the wall thickness is much smaller than the other dimensions of the cylinder and the wavelength, it has been assumed that they could be neglected. Geller and Haklay jointly carried out a series of measurements using two sets of cylinders which had length-to-outer diameter ratios of 6 and 4 respectively [Ref. 8]. Their results showed significant deviation from theoretical predictions near the  $H_{11}$  cutoff frequencies of the circular waveguide mode. This discovery caused doubt as to whether or not a theory neglecting the wall thickness could describe the scattering of a tubular cylinder in the vicinities of the waveguide mode cutoff. Because the waveguide modes are determined completely by the inner diameter of the cylinder, scattering from two sets of cylinders having length-to-inner diameter ratios of 6 and 4 are investigated in this thesis.

As shown in Figure 3.5, the target cylinder of the experiment has an inner radius  $a^-$ , an outer radius  $a^+$  and a length  $2h$ . The values  $2h$ ,  $2a^+$ ,  $2a^-$ ,  $h/a^+$  and  $h/a^-$  for each of these sixteen cylinders are given in Table IV. Note that the only difference between cylinder 01 and cylinder 1 is that cylinder 01 is about 6% longer than cylinder 1. Similar relations exist between each pair of the old and the new cylinders, with smaller fractional differences.

The values of  $2h/\lambda$  corresponding to the  $H_{11}$  mode cutoff frequencies of the different sets of cylinders used for the measurements are marked with the vertical solid lines labeled by " $H_{11}$ " in Figure 3.6 through Figure 3.9. In Figure 3.6, the  $H_{11}$  cutoff frequency occurs with data from cylinder 03. Since cylinder 03 has a length-to-inner diameter ratio of 4.19, its  $H_{11}$  mode cutoff frequency corresponds to a  $2h/\lambda$  value of 2.456. In Figure 3.7, the  $H_{11}$  cutoff frequency occurs with data from cylinder 07. Since cylinder 07 has a

**TABLE IV**  
**PHYSICAL PARAMETERS OF THE CYLINDERS**

Cylinder	$2h$ (cm)	$2a^+$ (cm)	$2a^-$ (cm)	$h/a^+$	$h/a^-$
01	3.81	0.9525	0.8915	4.00	4.274
02	5.08	1.27	1.199	4.00	4.237
03	6.352	1.588	1.516	4.00	4.19
04	7.62	1.908	1.849	4.00	4.121
05	5.715	0.9525	0.8915	6.00	6.41
06	7.62	1.27	1.199	6.00	6.355
07	9.525	1.588	1.516	6.00	6.281
08	11.43	1.908	1.849	6.00	6.182
1	3.566	0.9525	0.8915	3.744	4.00
2	4.796	1.27	1.199	3.776	4.00
3	6.064	1.588	1.516	3.819	4.00
4	7.396	1.908	1.849	3.882	4.00
5	5.349	0.9525	0.8915	5.616	6.00
6	7.193	1.27	1.199	5.664	6.00
7	9.098	1.588	1.516	5.729	6.00
8	11.09	1.908	1.849	5.722	6.00

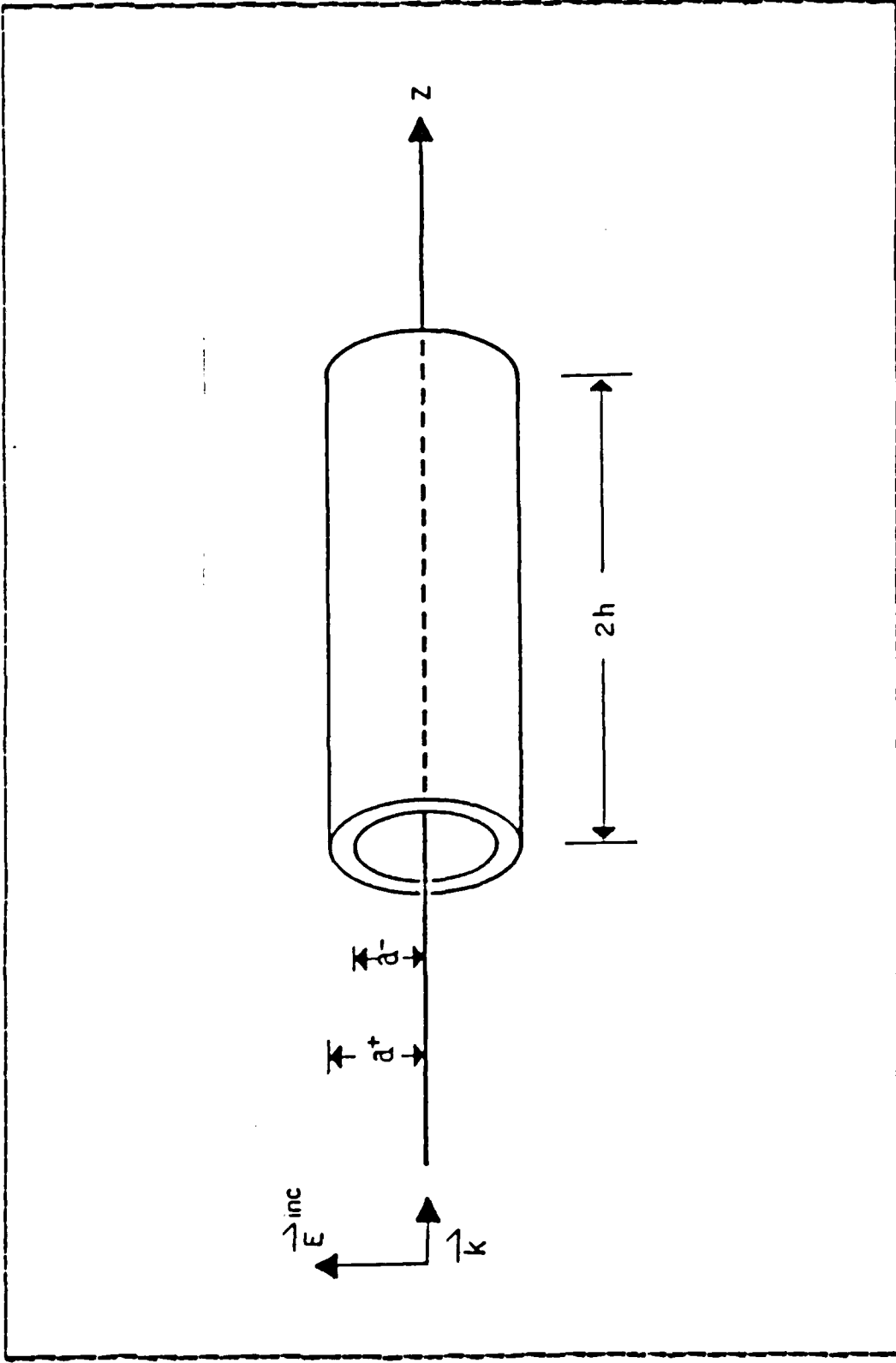


Figure 3.5 Geometry of The Problem.

length-to-inner diameter ratio of 6.281, its  $H_{11}$  mode cutoff frequency corresponds to a  $2h/\lambda$  value of 3.682. The theoretical model, having  $a = a^-$ , has the cutoff  $2h/\lambda$  value equal to those of the new cylinders plotted in Figure 3.8 and Figure 3.9. The  $2h/\lambda$  value equals 2.345 for the set of cylinders with  $h/a^- = 4$  and equals 3.517 for those with  $h/a^- = 6$ . It is clear that the old data are distinctly different from the new data. The data in Figure 3.8 and Figure 3.9 agree with the theoretical curves over the whole frequency range being studied.

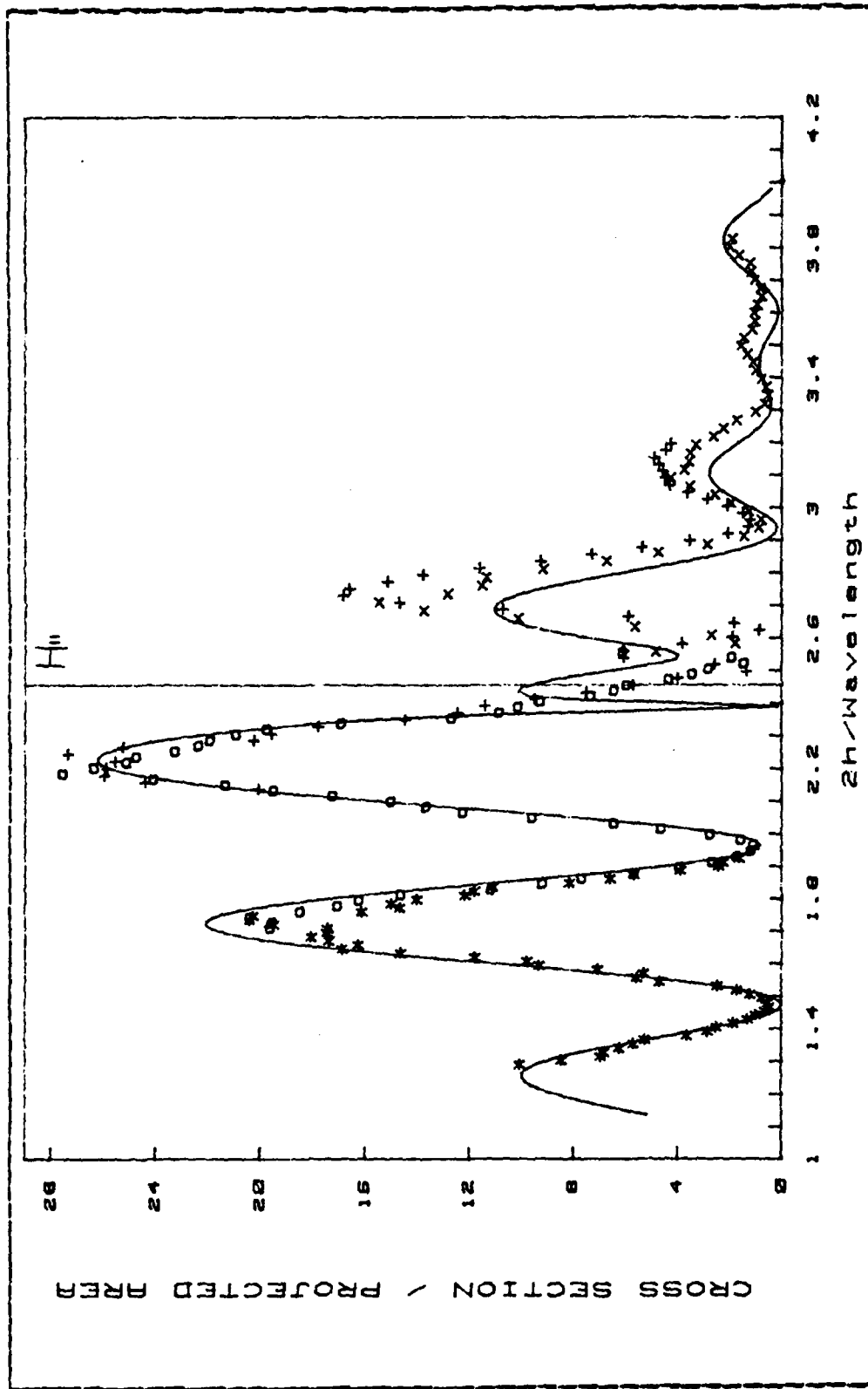


Figure 3.6 Head-on Cross Section and The  $H_{11}$  Cutoff Frequency, Old Results ( $h/a = 4$ ).

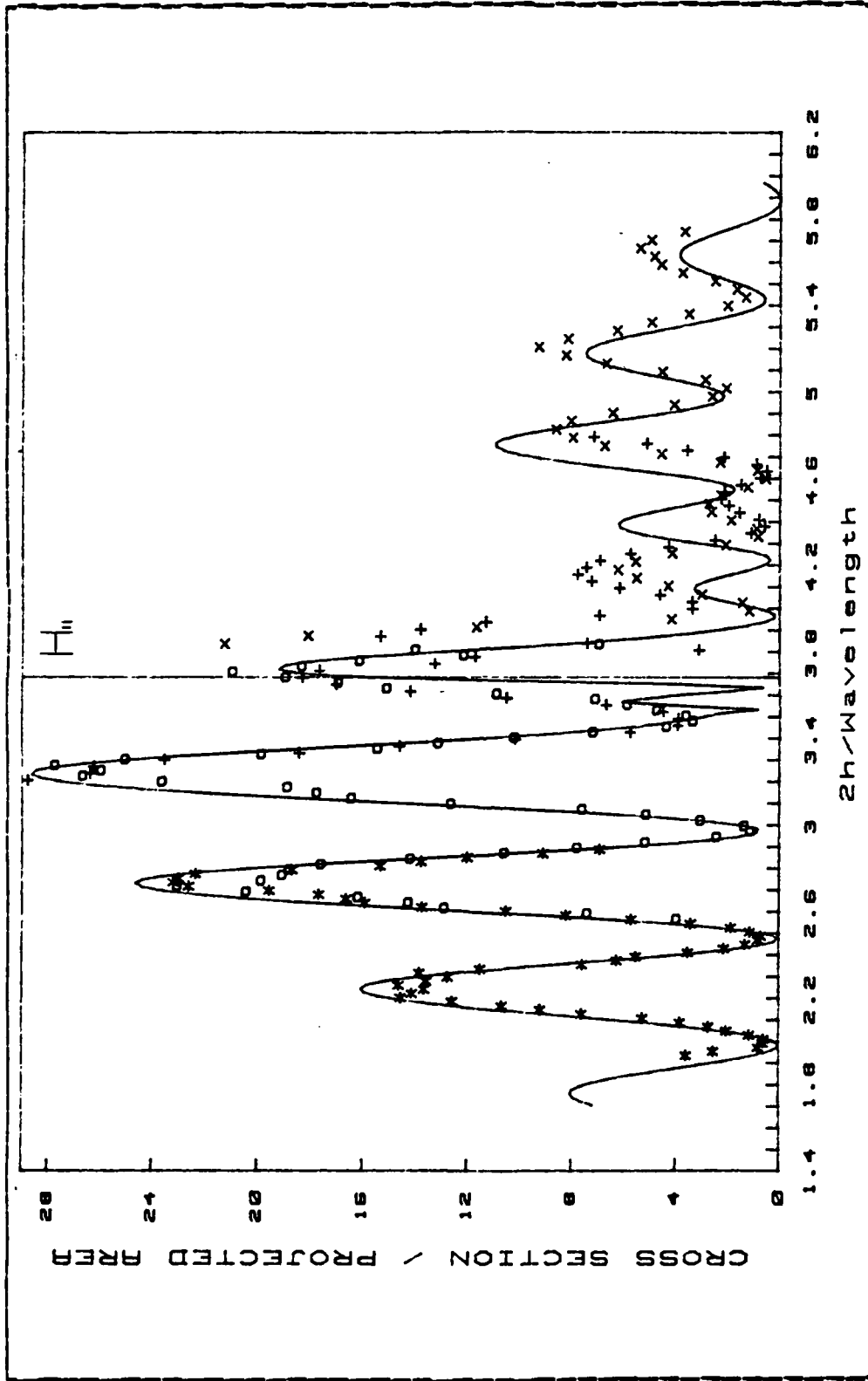


Figure 3.7 Head-on Cross Section and  
The  $H_{II}$  Cutoff Frequency, Old Results ( $h/a^2 = 6$ ).

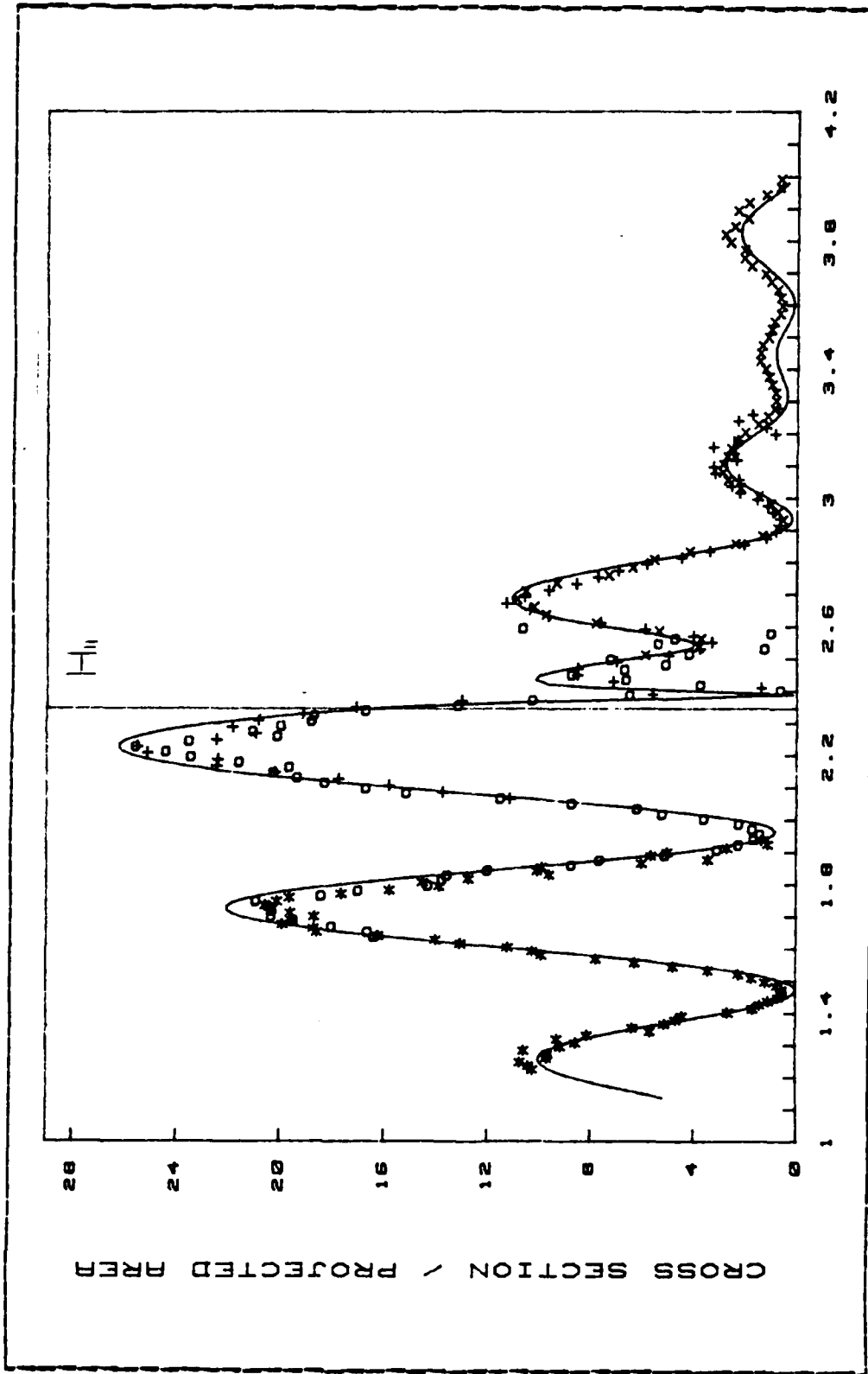


Figure 3.8 Head-on Cross Section and The  $H_{II}$  Cutoff Frequency, New Results ( $h/a = 4$ ).

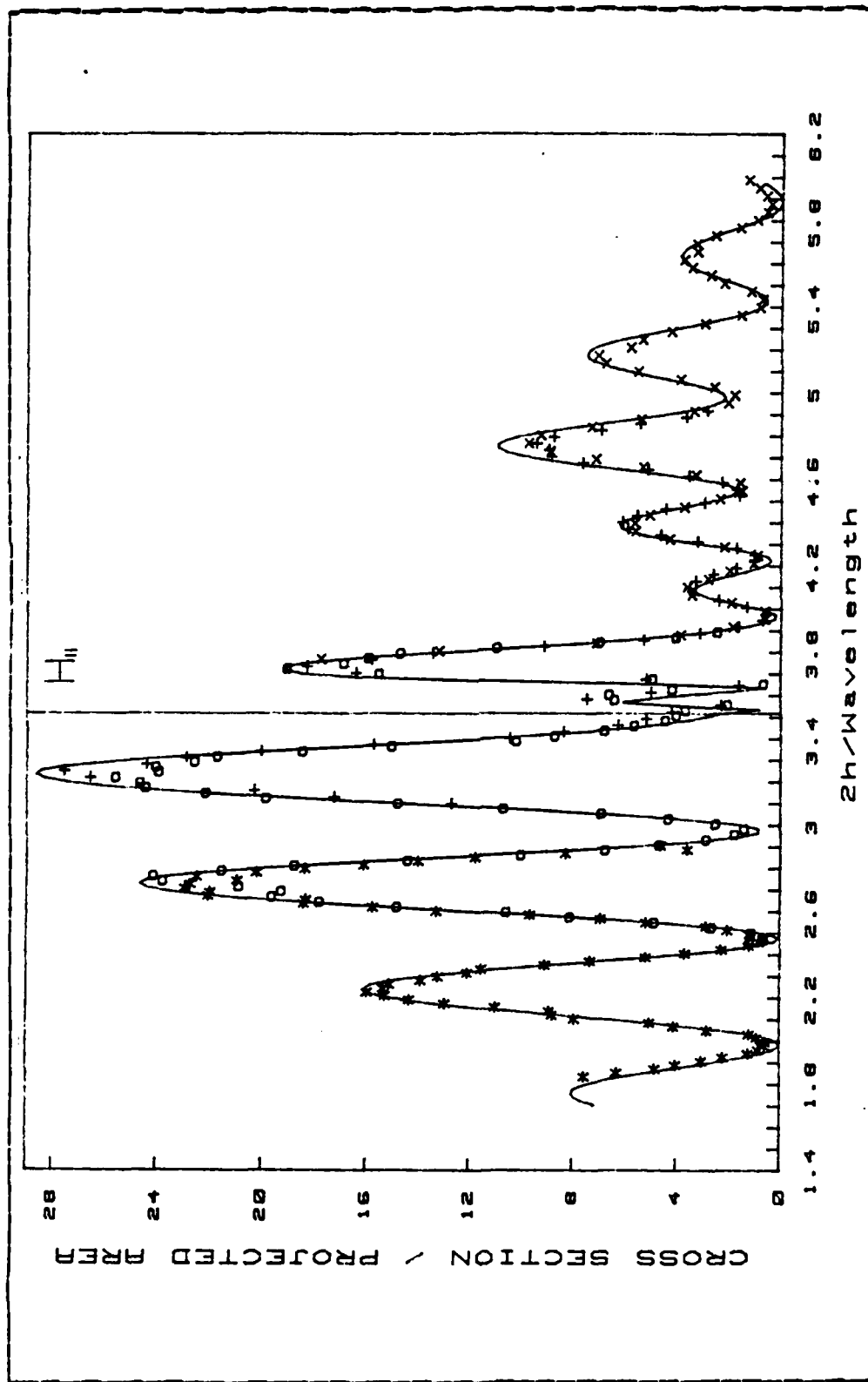


Figure 3.9 Head-on Cross Section and  
The H<sub>11</sub> Cutoff Frequency, New Results ( $h/a = 6$ ).

#### IV. EFFECTS OF COUPLING BETWEEN THE TARGET AND ITS SUPPORT

##### A. RAPID SPECTRAL DOMAIN FLUCTUATIONS IN THE BROADSIDE DATA

When the broadside data are compared to theoretical predictions, the phase shifts agree very well while the overall shape of the measured cross section data is consistent with the theoretical curves. It appears that each set of the cross section data contains a fast fluctuating component superimposed onto the smooth theoretical curve across the frequency range. Several possibilities exist that may cause this problem. One that is investigated in this chapter is the effect of the coupling between the cylinder and the stand.

The measurement procedures call for the subtraction of background from the measured data when the target is present. This subtraction removes almost all unwanted signals except those introduced by the presence of the target. Since the data are taken in an anechoic chamber, the most significant error of this type may come from the coupling between the target and its support.

Even though the agreement between the head-on scattering data and theory suggests that this coupling should be negligible, there is no assurance that the same is true for the broadside case. In order to determine whether this rapid spectral domain fluctuation is caused by the coupling between the target and its support, several supports of different geometry were constructed and tested. The results indicate that this coupling is negligible in this case.

## B. MEASURED RESULTS WITH VARIOUS SUPPORTS

In order to investigate the effect of the coupling between the target and its support, five different supports were constructed. Three views of each of the five different supports, (a) through (e), are shown in Figure 4.1. They are arranged according to the order in which measurements were taken. The left most column shows the front views, the center column shows the top views and the right most column shows the side views.

Two sets of results for each support were obtained. Figure 4.2 and Figure 4.7 show the experimental points and theoretical curves of the cross sections of cylinders with the length to inner diameter ratio of 6. Figure 4.12 and Figure 4.17 show the cross sections of those having the length to diameter ratio of 4 when the support of Figure 4.1, (a) was used. An index list of the various supports used and the measured data is given in Table V.

**TABLE V**  
INDEX TO PLOTTED DATA FROM  
THE USE OF DIFFERENT TARGET SUPPORT

Support	The length to inner diameter ratio			
	6		4	
	Cross section	Phase shift	Cross section	Phase shift
Fig 4-1(a)	Fig 4-2	Fig 4-7	Fig 4-12	Fig 4-17
" (b)	" 4-3	" 4-8	" 4-13	" 4-18
" (c)	" 4-4	" 4-9	" 4-14	" 4-19
" (d)	" 4-5	" 4-10	" 4-15	" 4-20
" (e)	" 4-6	" 4-11	" 4-16	" 4-21

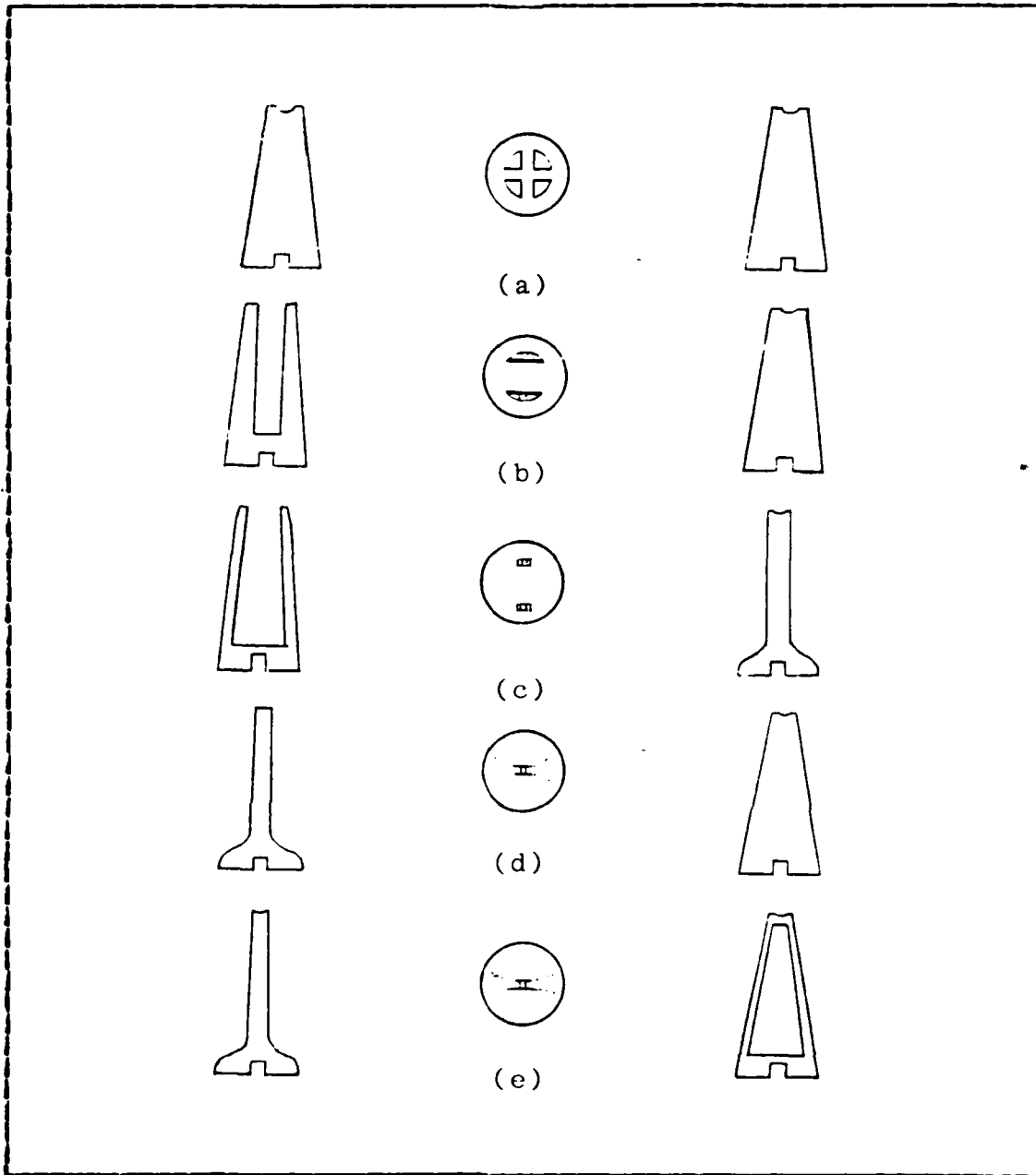


Figure 4.1 Various Types of Support.

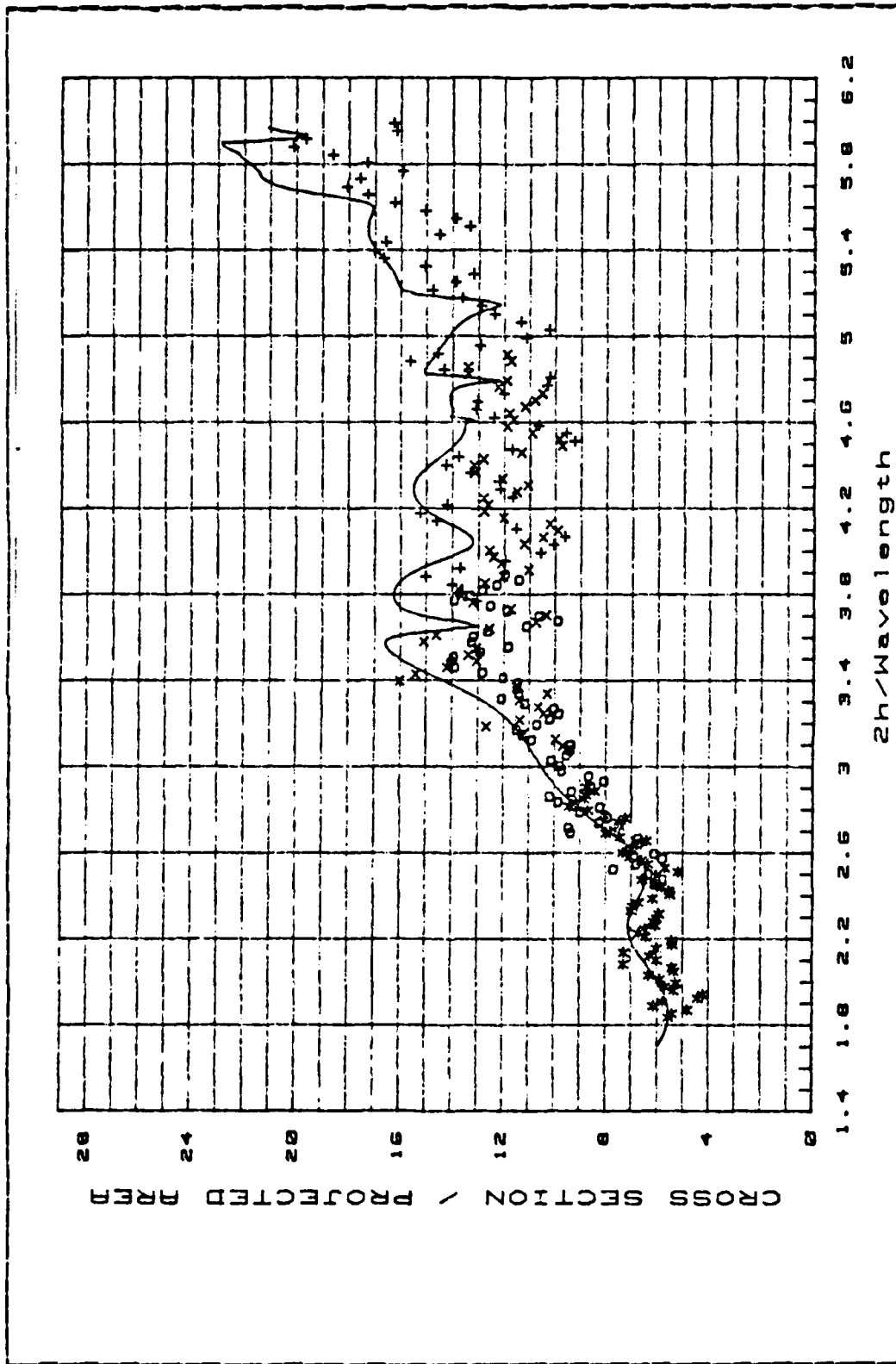


Figure 4.2 Measured Broadside Cross Section ( $h/a = 6$ ) -

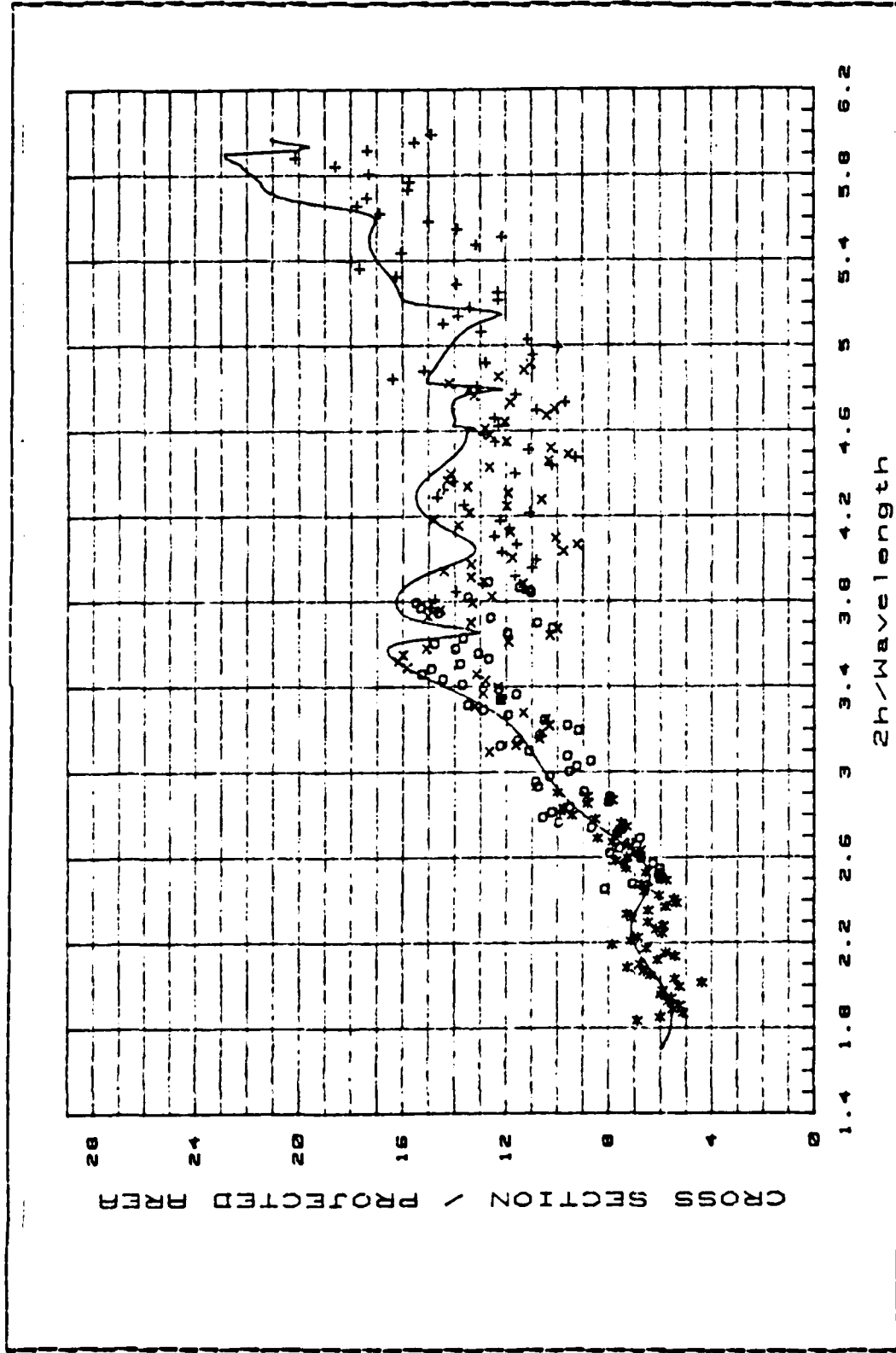


Figure 4.3 Measured Broadside Cross Section ( $h/a = 6$ ).

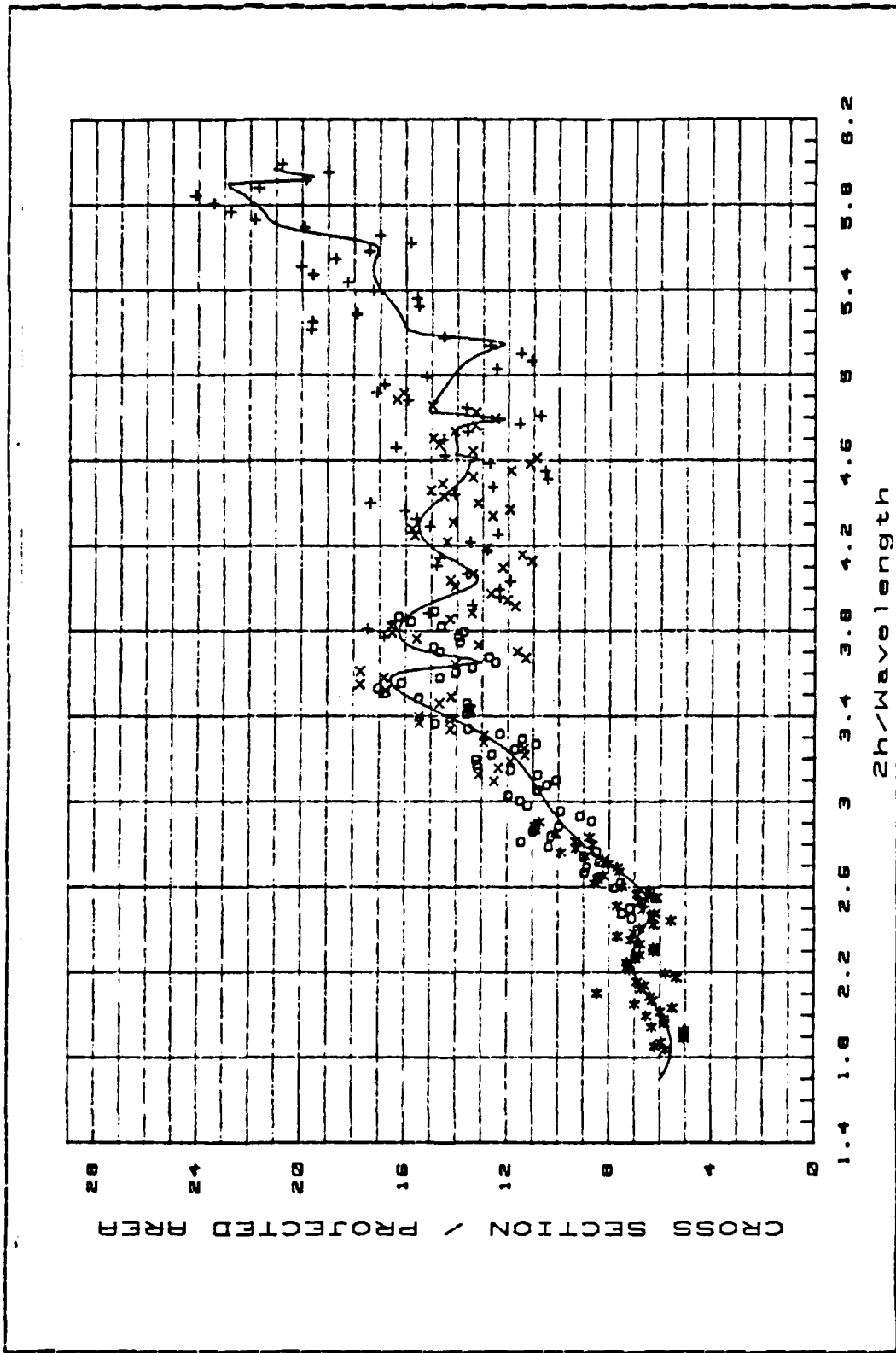


Figure 4.4 Measured Broadside Cross Section ( $b/a = 6$ ).

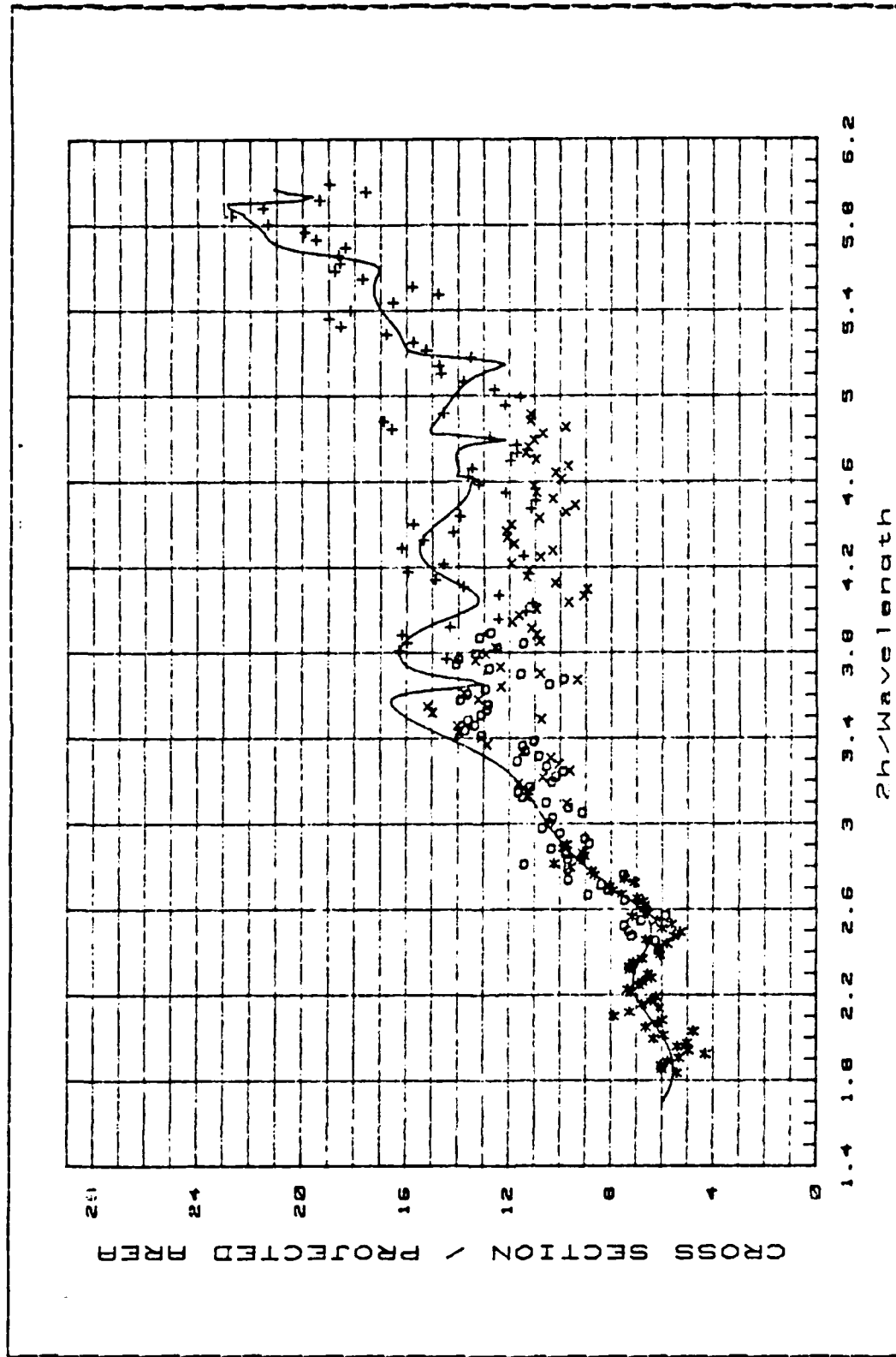


Figure 4.5 Measured Broadside Cross Section ( $h/a = 6$ ).

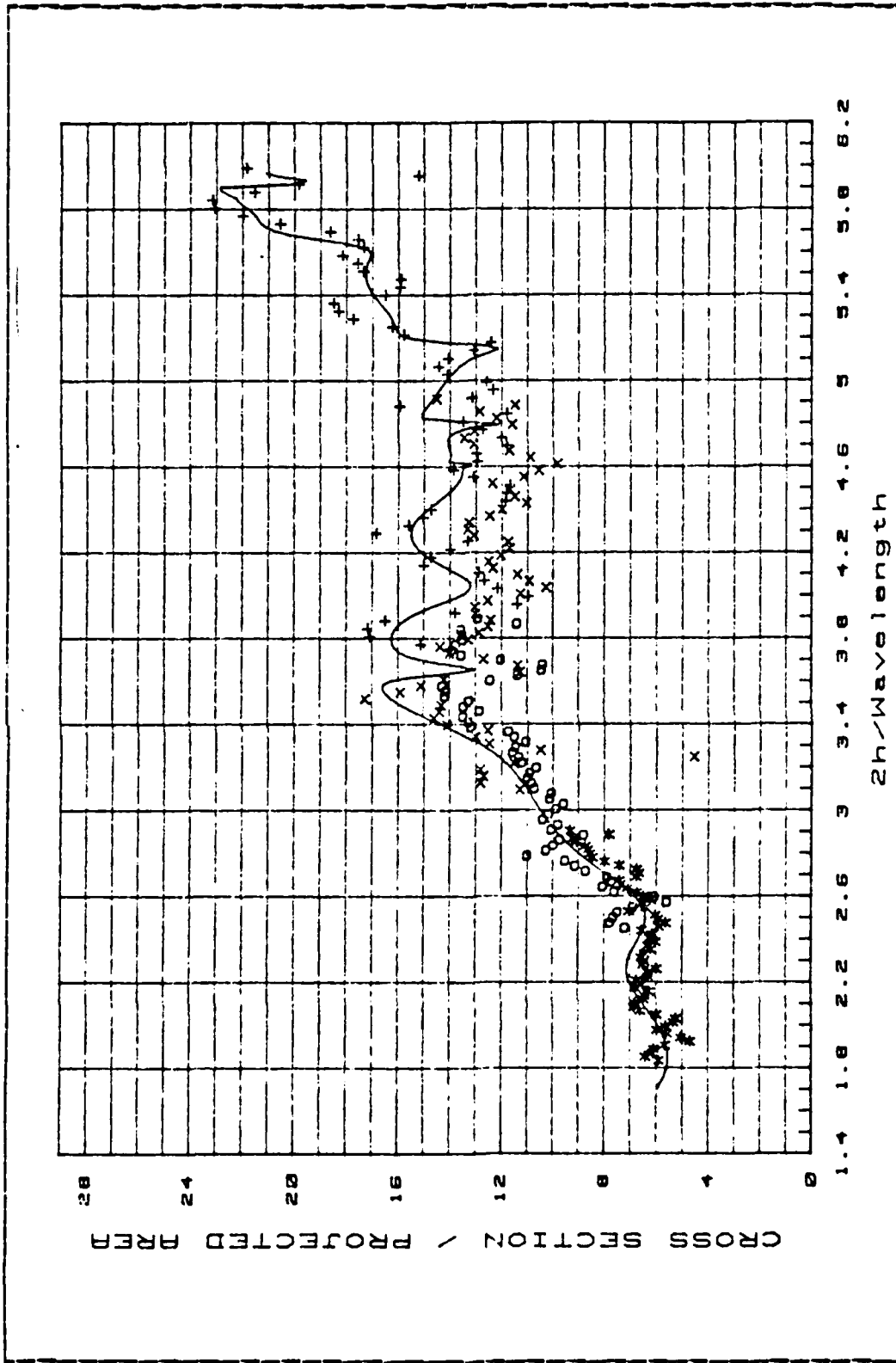


Figure 4.6 Measured Broadside Cross Section ( $h/a = 6$ ) -

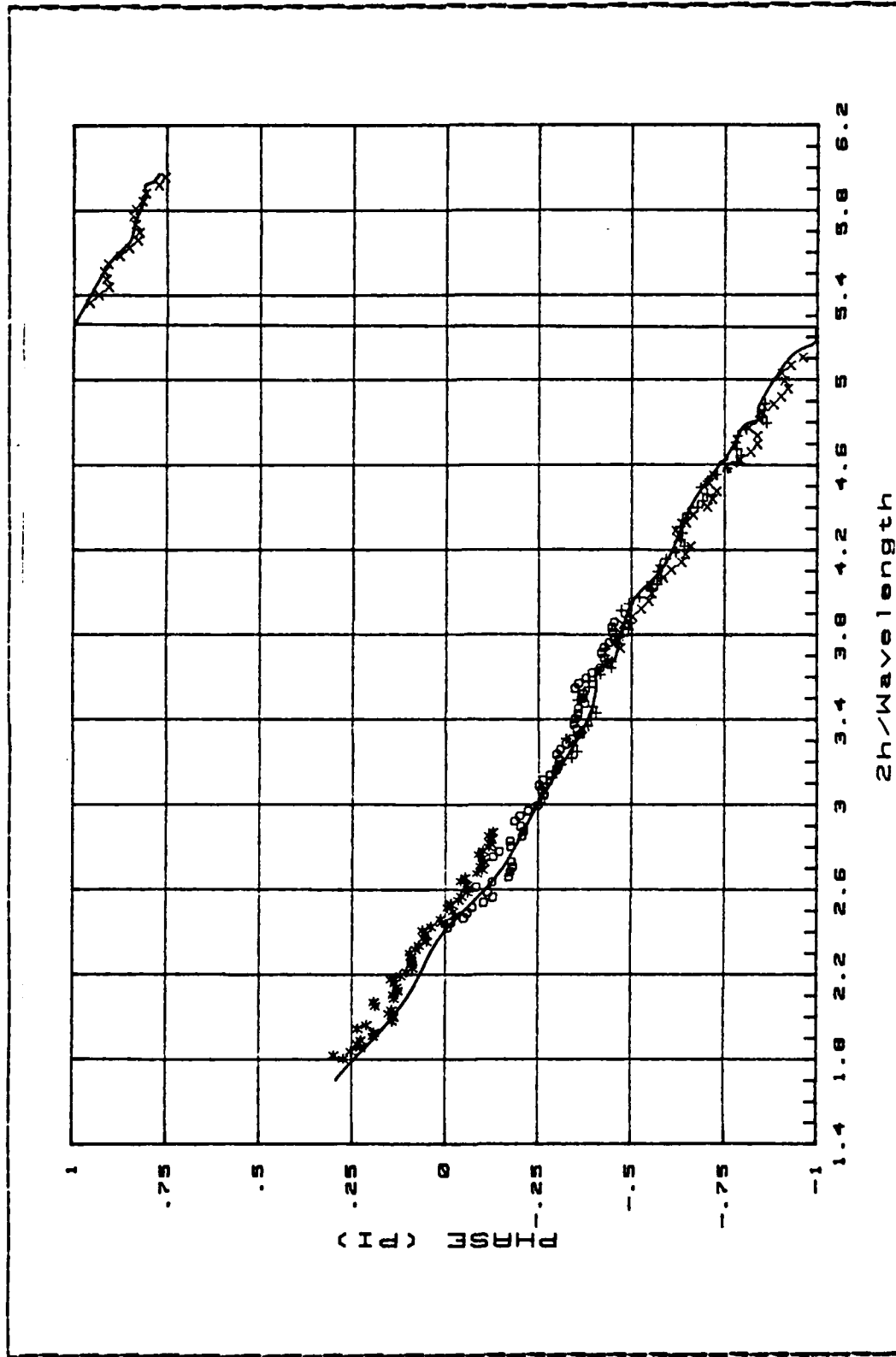


Figure 4.7 Measured Broadside Phase Shift ( $h/a = 6$ ).

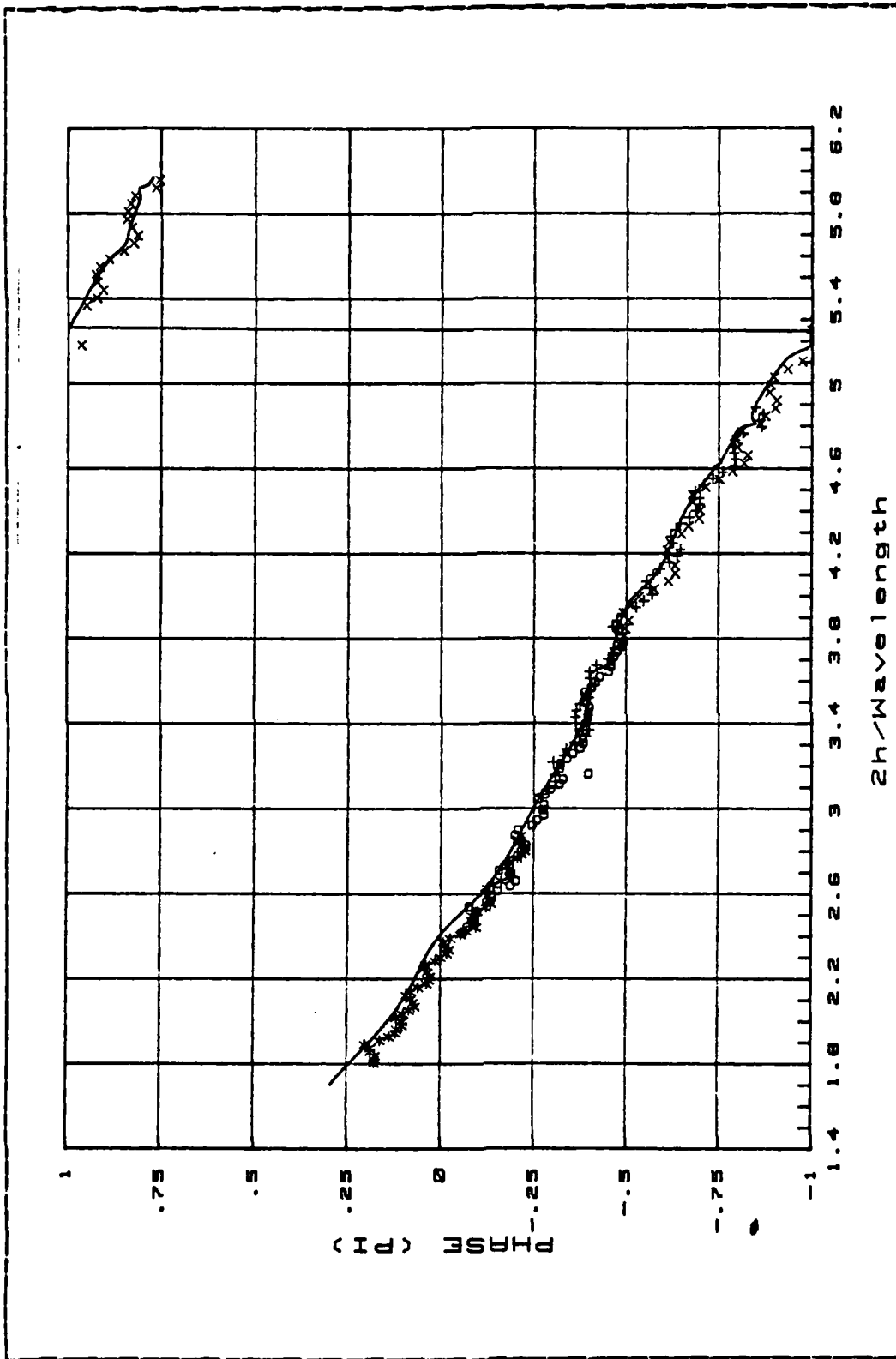


Figure 4.8 Measured Broadside Phase Shift ( $h/a = 6$ ).

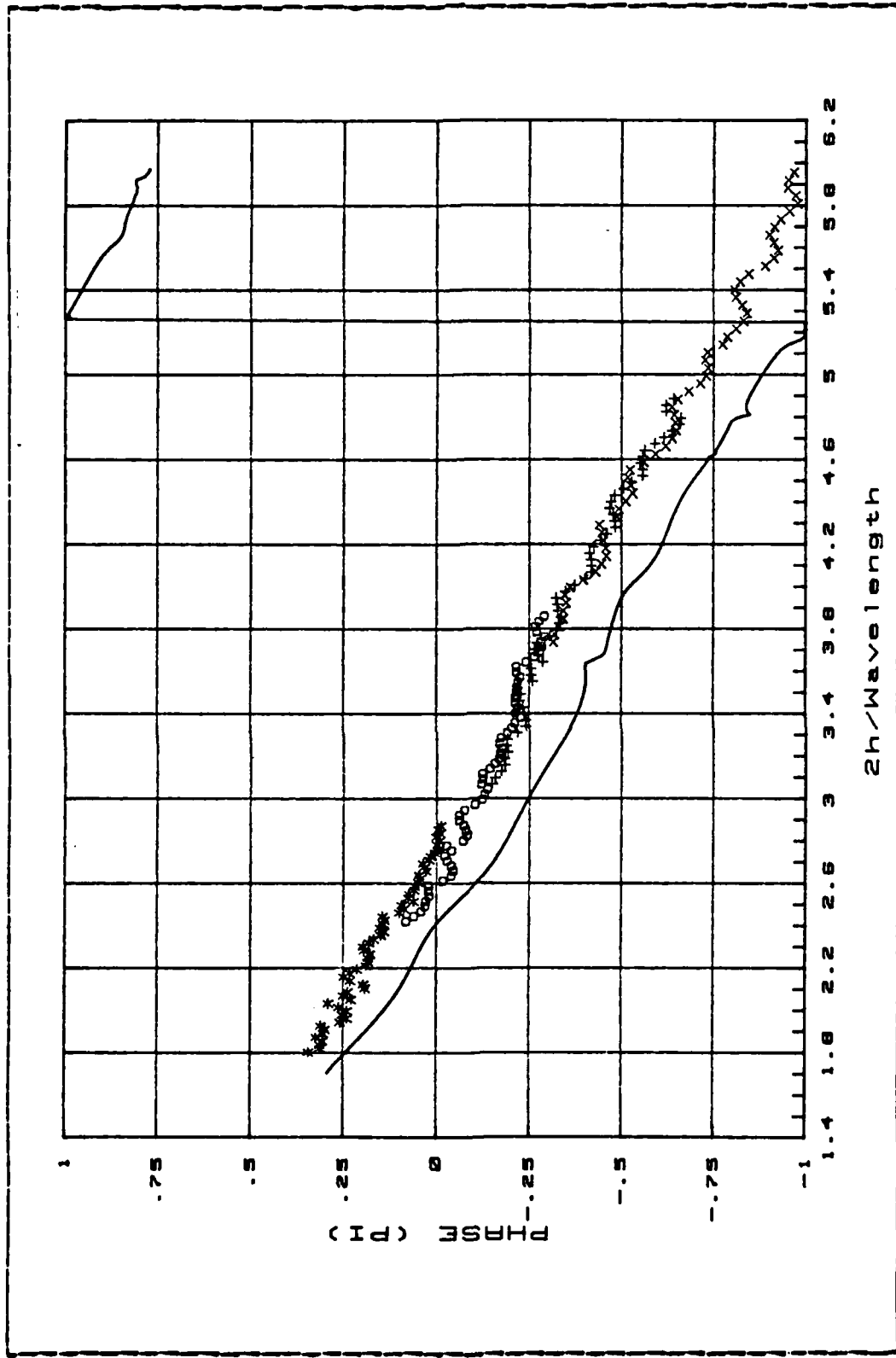


Figure 4.9 Measured Broadside Phase Shift ( $h/a = 6$ ).

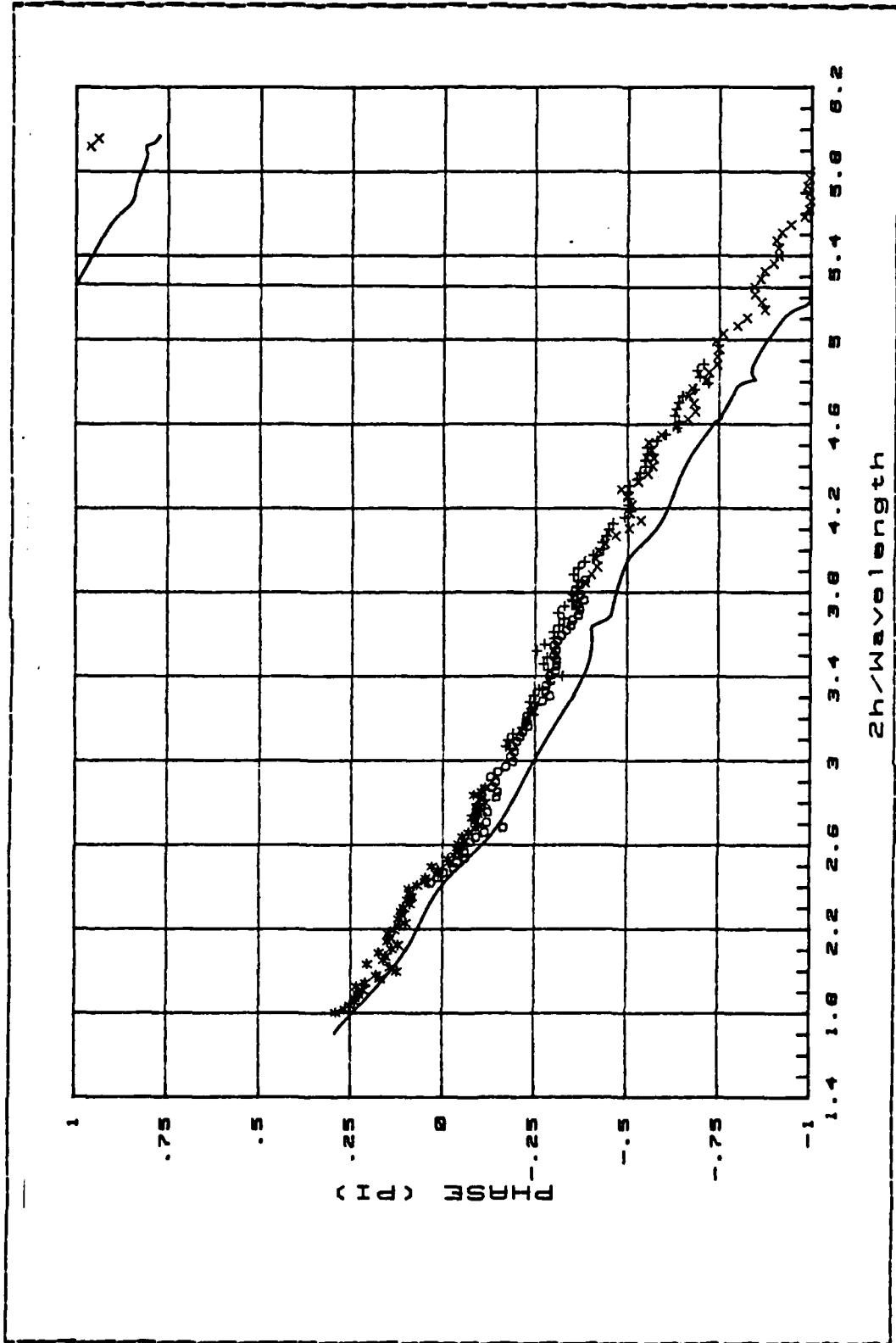


Figure 4.10 Measured Broadside Phase Shift ( $h/a = 6$ ).

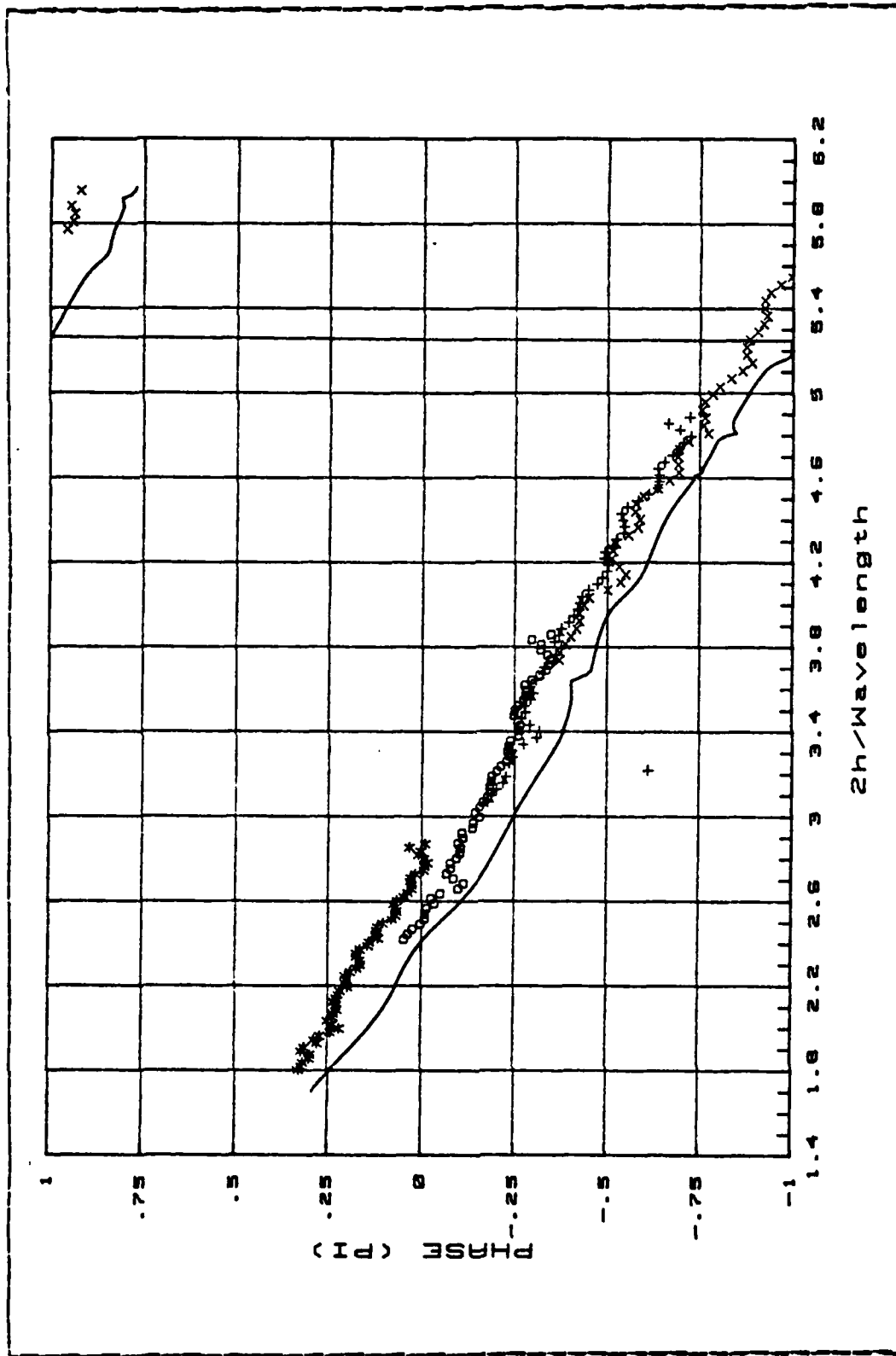


Figure 4.11 Measured Broadside Phase Shift ( $h/a = 6$ )

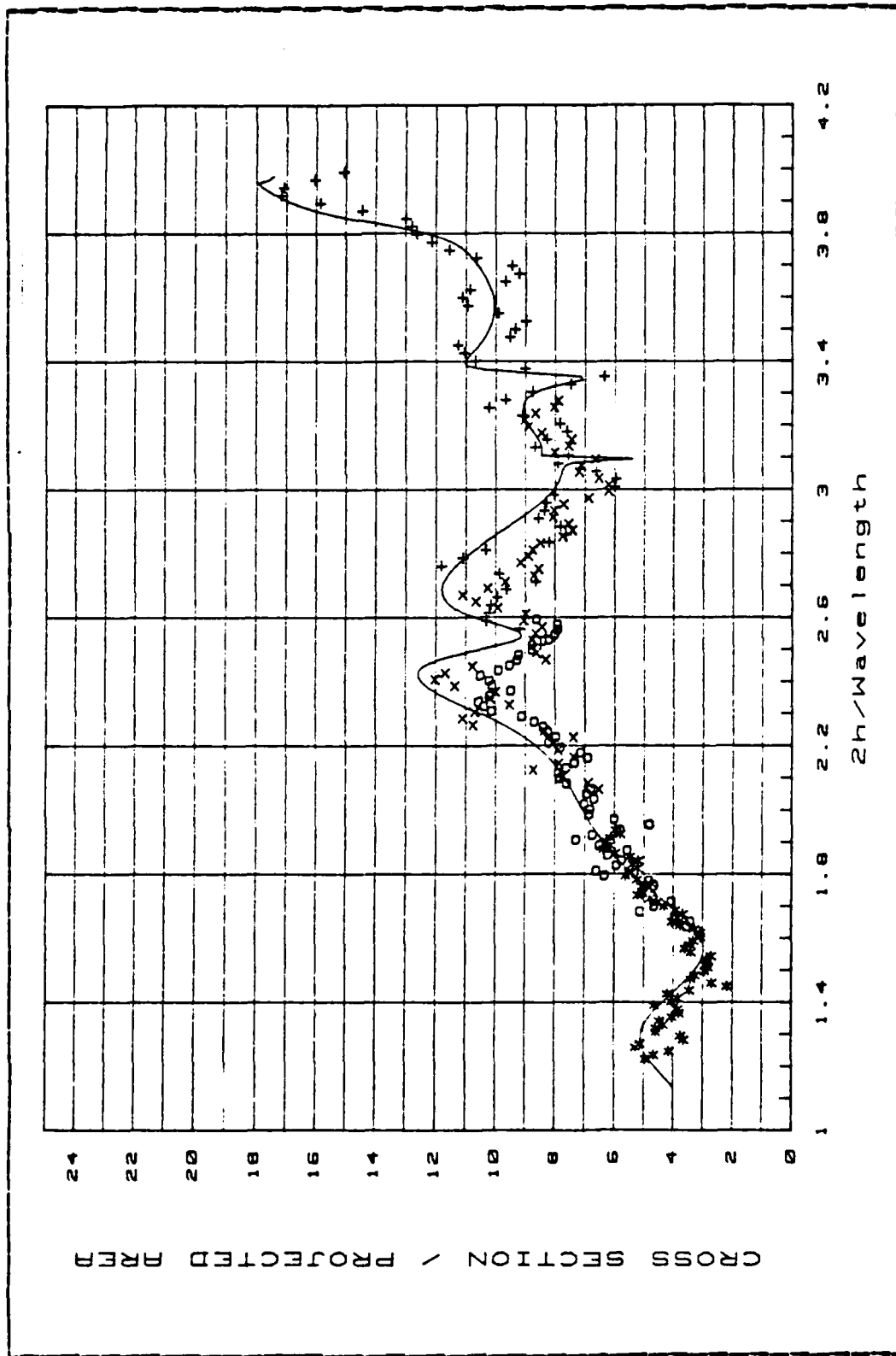


Figure 4.12 Measured Broadside Cross Section ( $h/a = 4$ ).

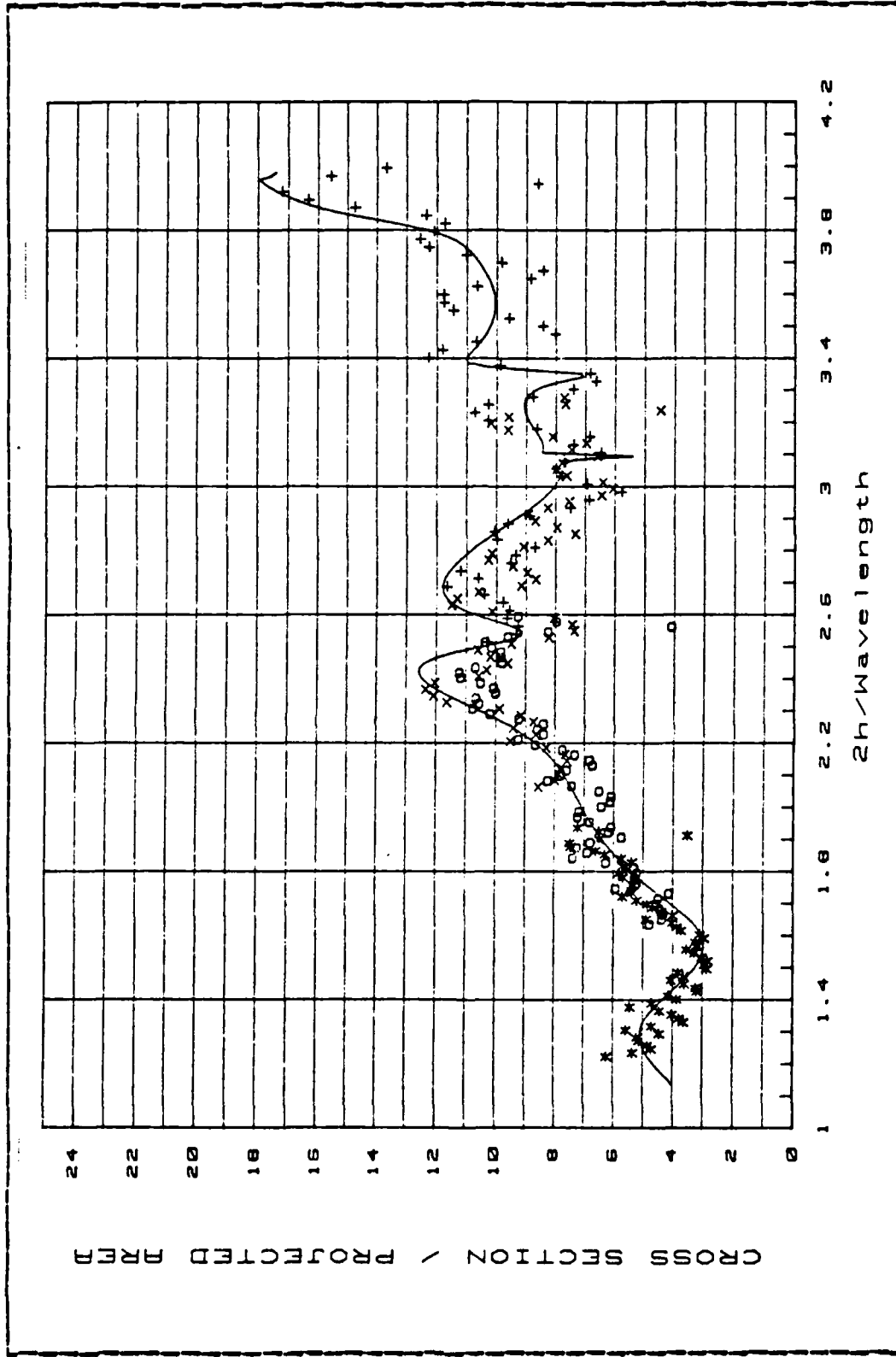


Figure 4.13 Measured Broadside Cross Section ( $h/a = 4$ ).

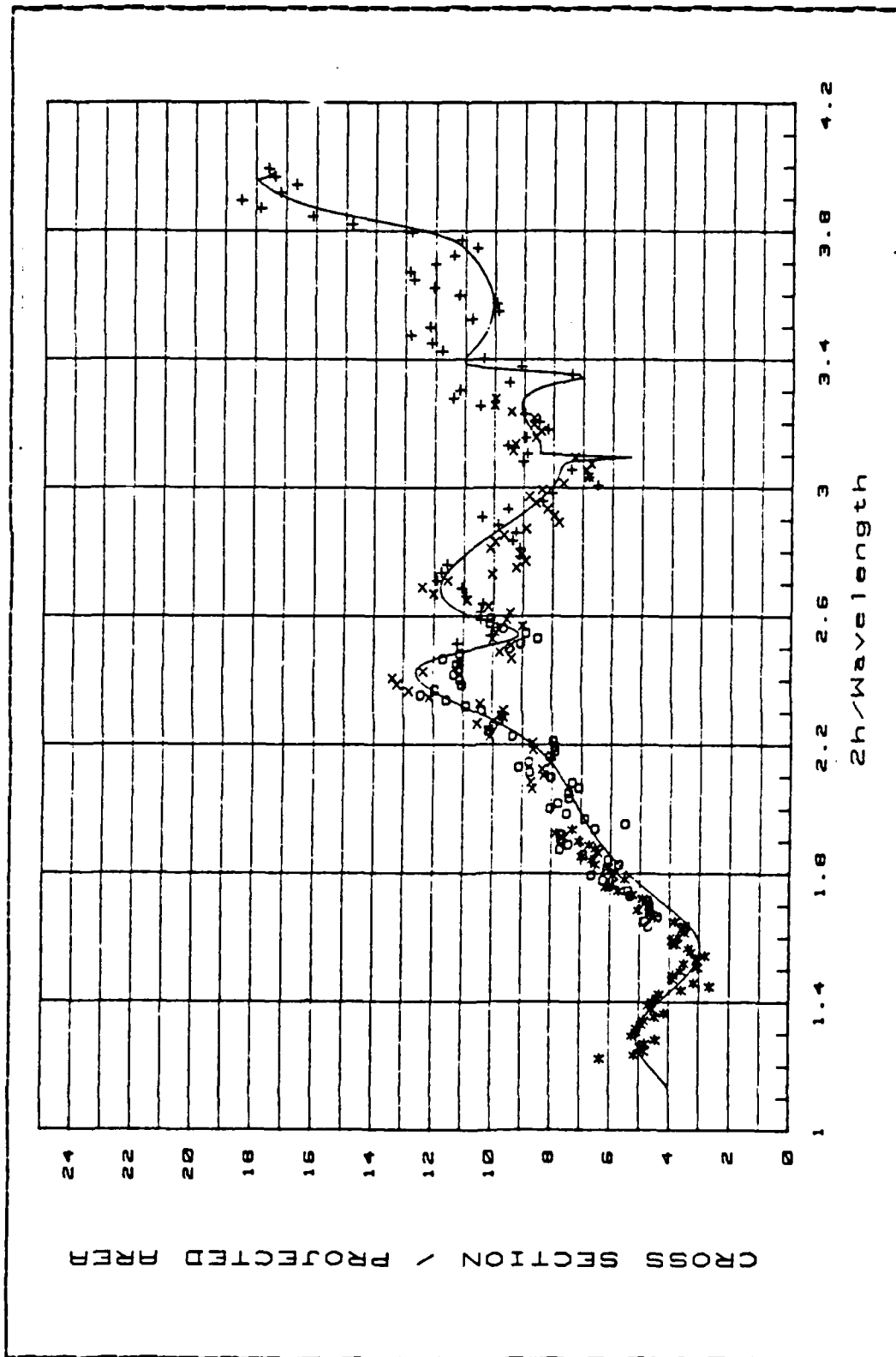


Figure 4.14 Measured Broadside Cross Section ( $h/a = 4$ ).

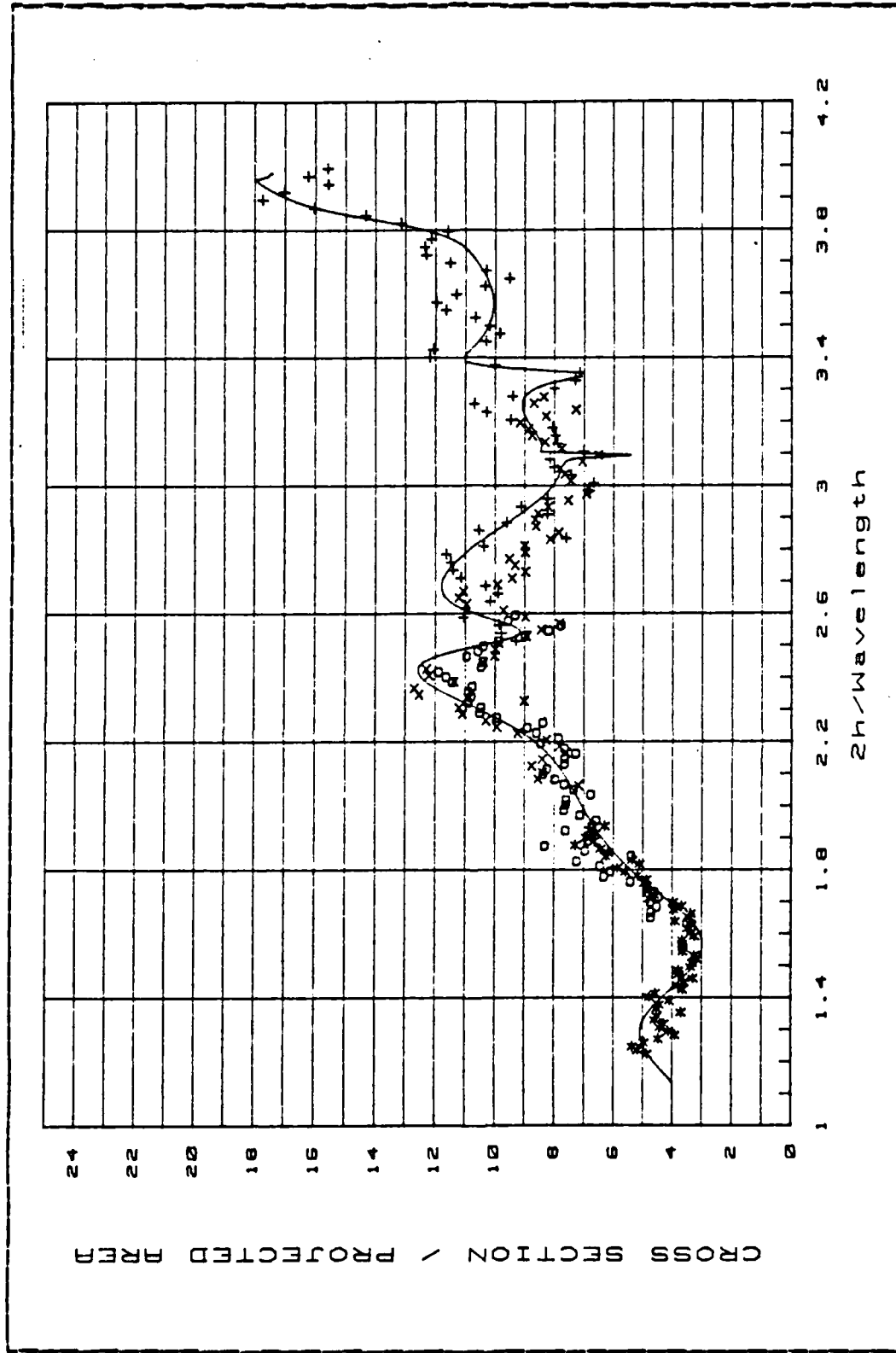


Figure 4.15 Measured Broadside Cross Section ( $h/a = 4$ ).

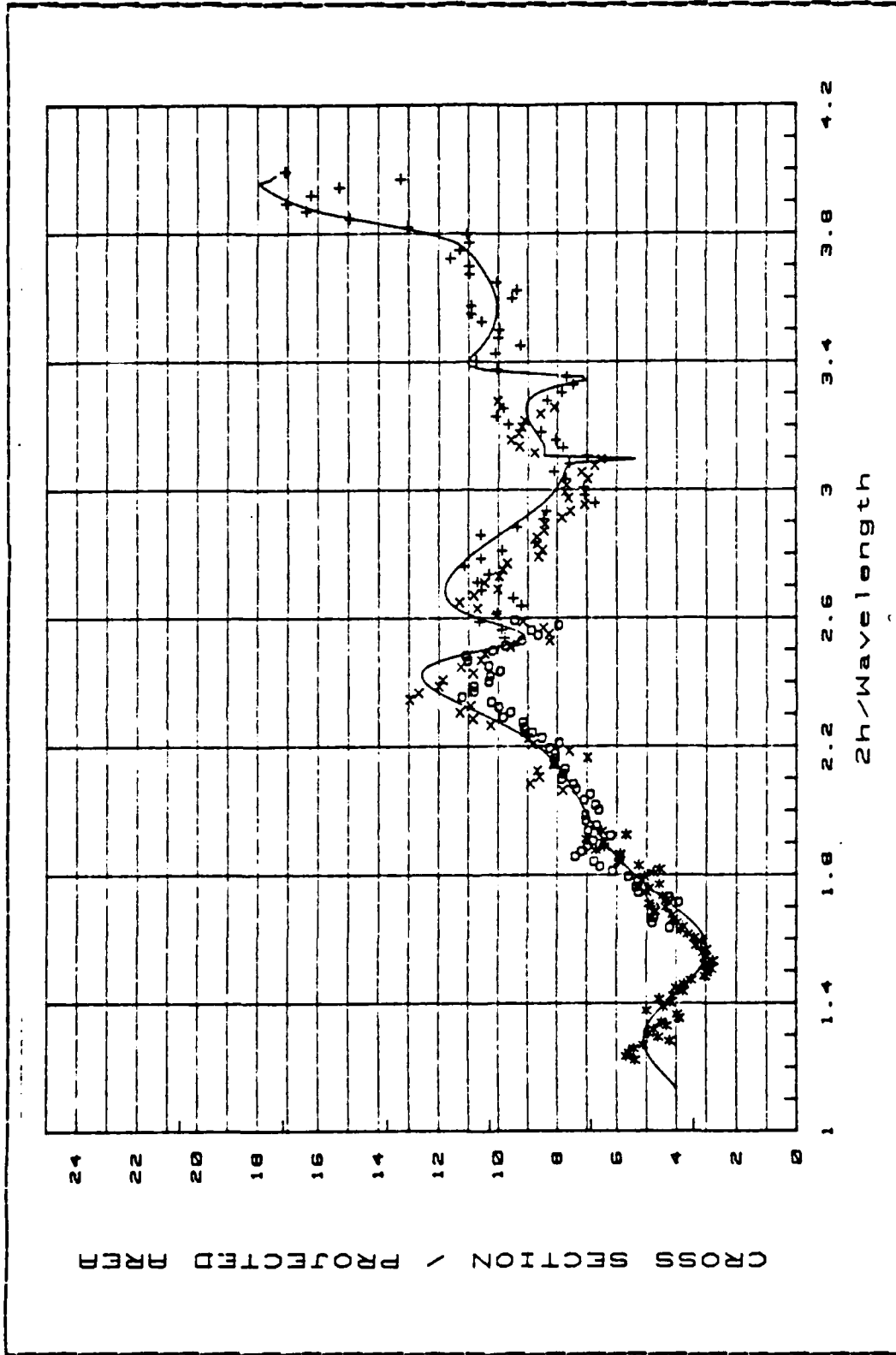


Figure 4.16 Measured Broadside Cross Section ( $h/a = 4$ ).

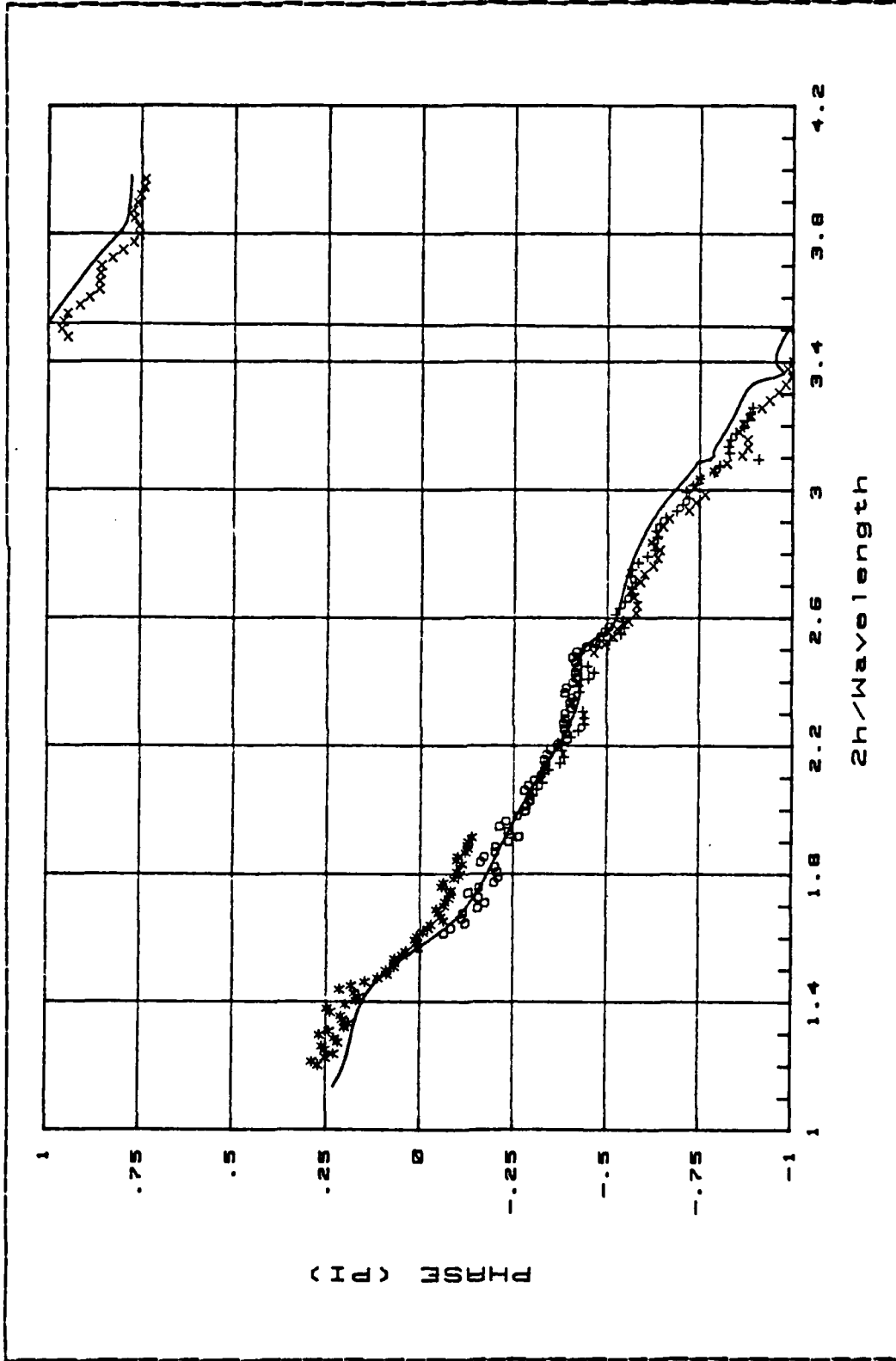


Figure 4.17 Measured Broadside Phase Shift ( $h/a = 4$ ).

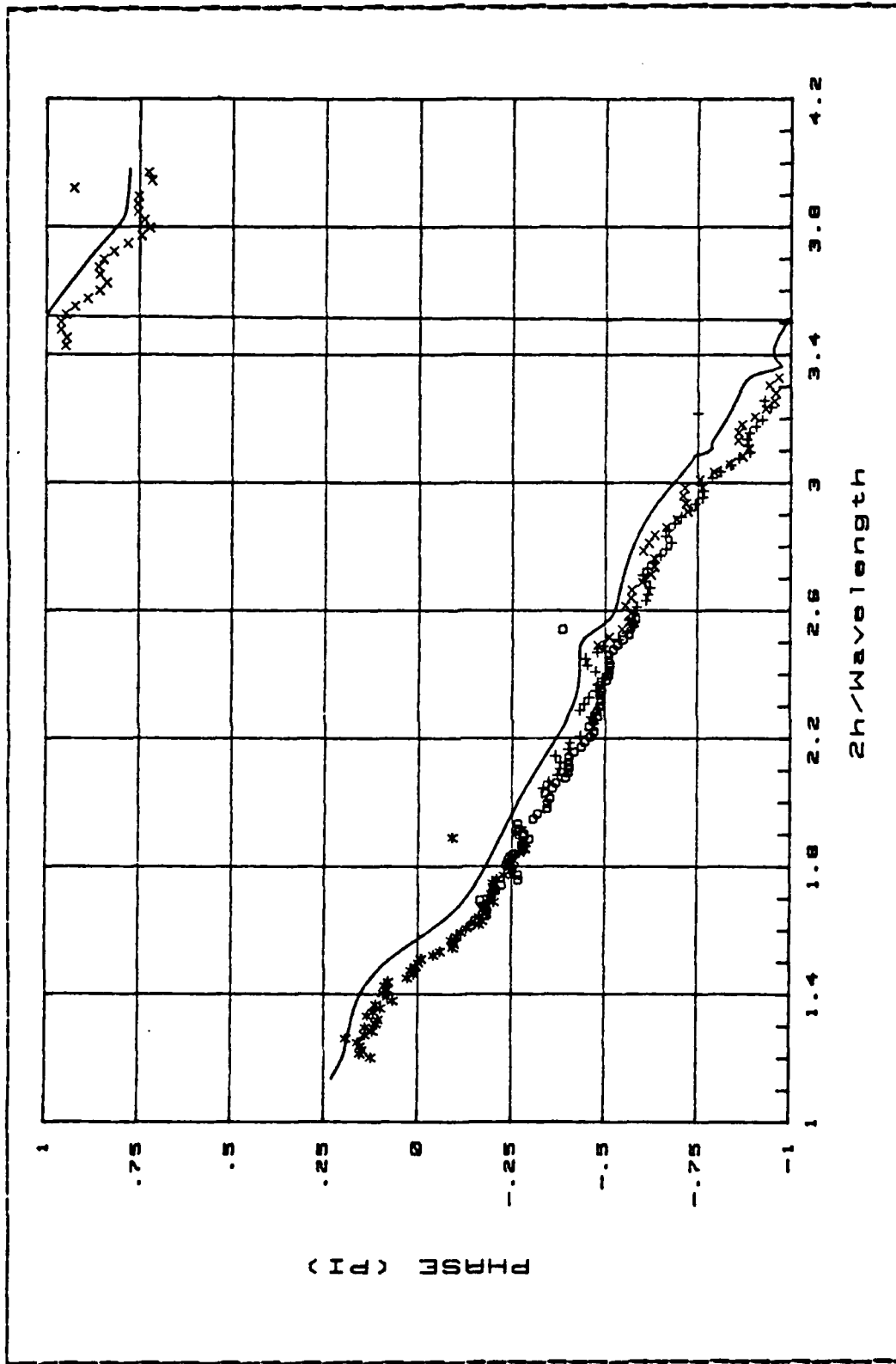


Figure 4.18 Measured Broadside Phase Shift ( $h/a = 4$ ).

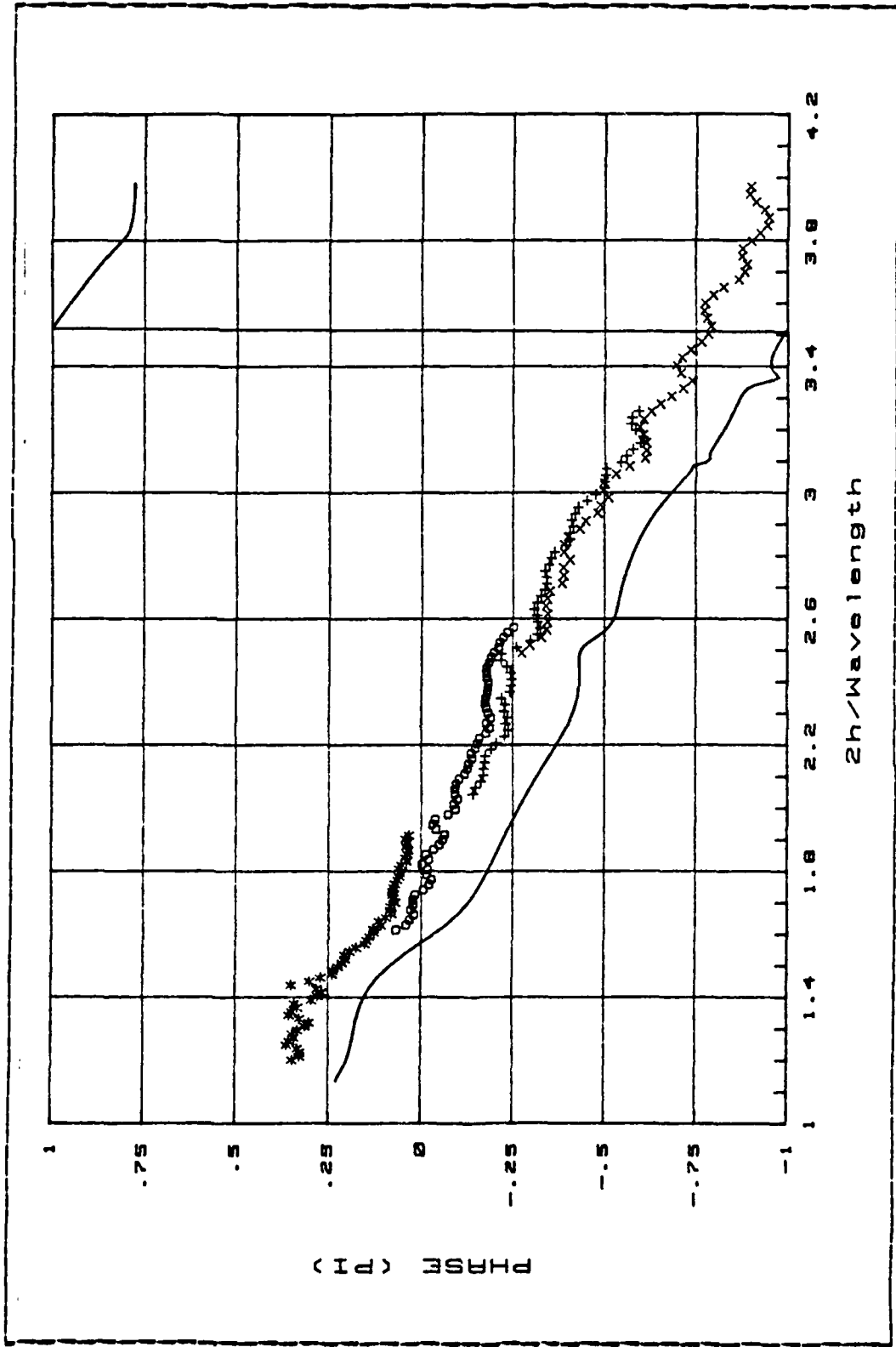


Figure 4.19 Measured Broadside Phase Shift ( $b/a = 4$ )

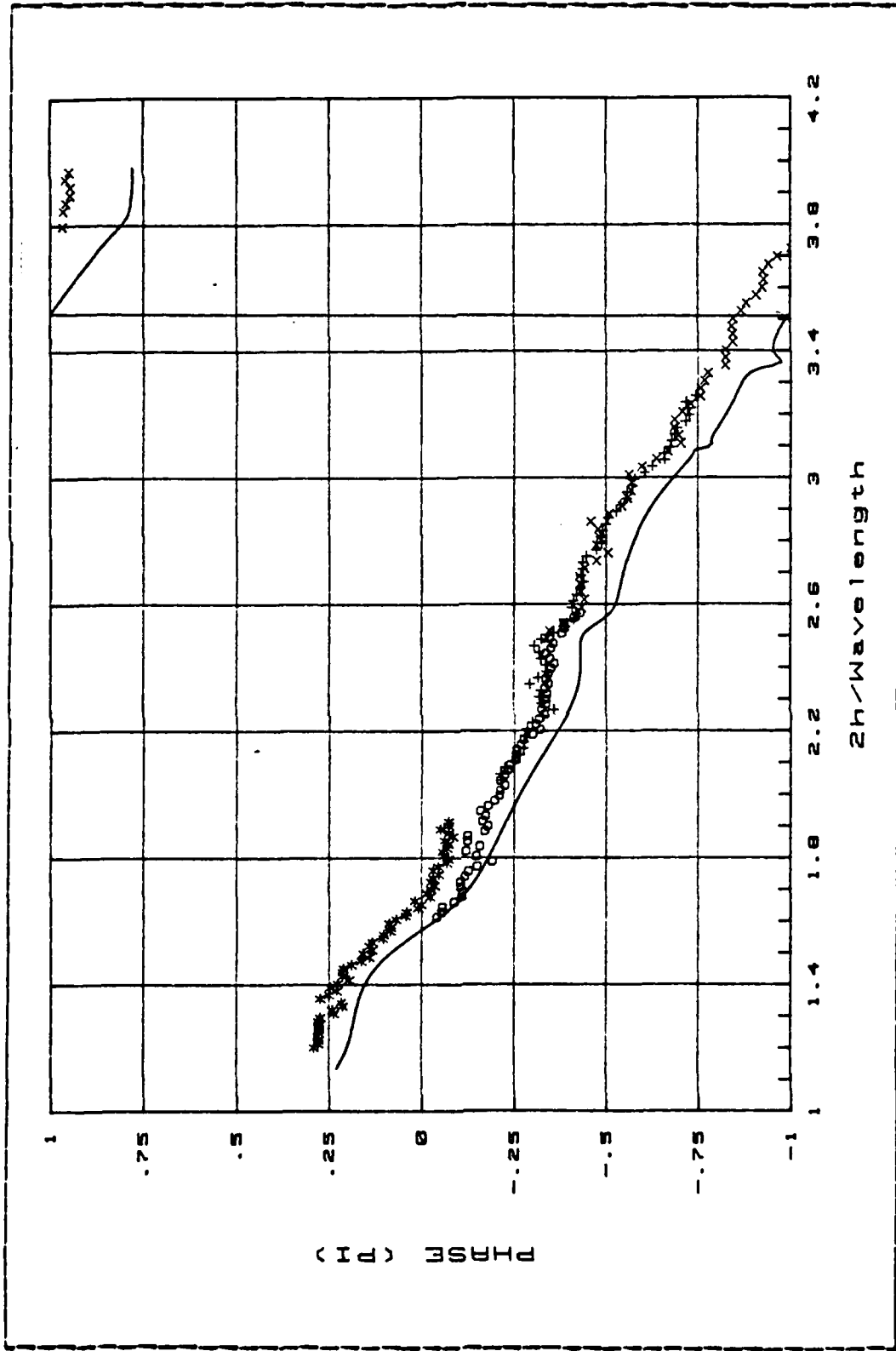


Figure 4.20 Measured Broadside Phase Shift ( $h/a = 4$ ).

AD-A161 500

EFFECTS OF WAVEGUIDE MODES ON THE SCATTERING OF A  
FINITE TUBULAR CYLINDER(U) NAVAL POSTGRADUATE SCHOOL  
MONTEREY CA G P CHUNG SEP 85

2/2

UNCLASSIFIED

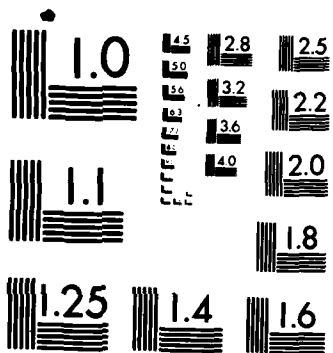
F/G 20/14

NL

END

FORM 1

DTIC



MICROCOPY RESOLUTION TEST CHART  
NATIONAL BUREAU OF STANDARDS-1963-A

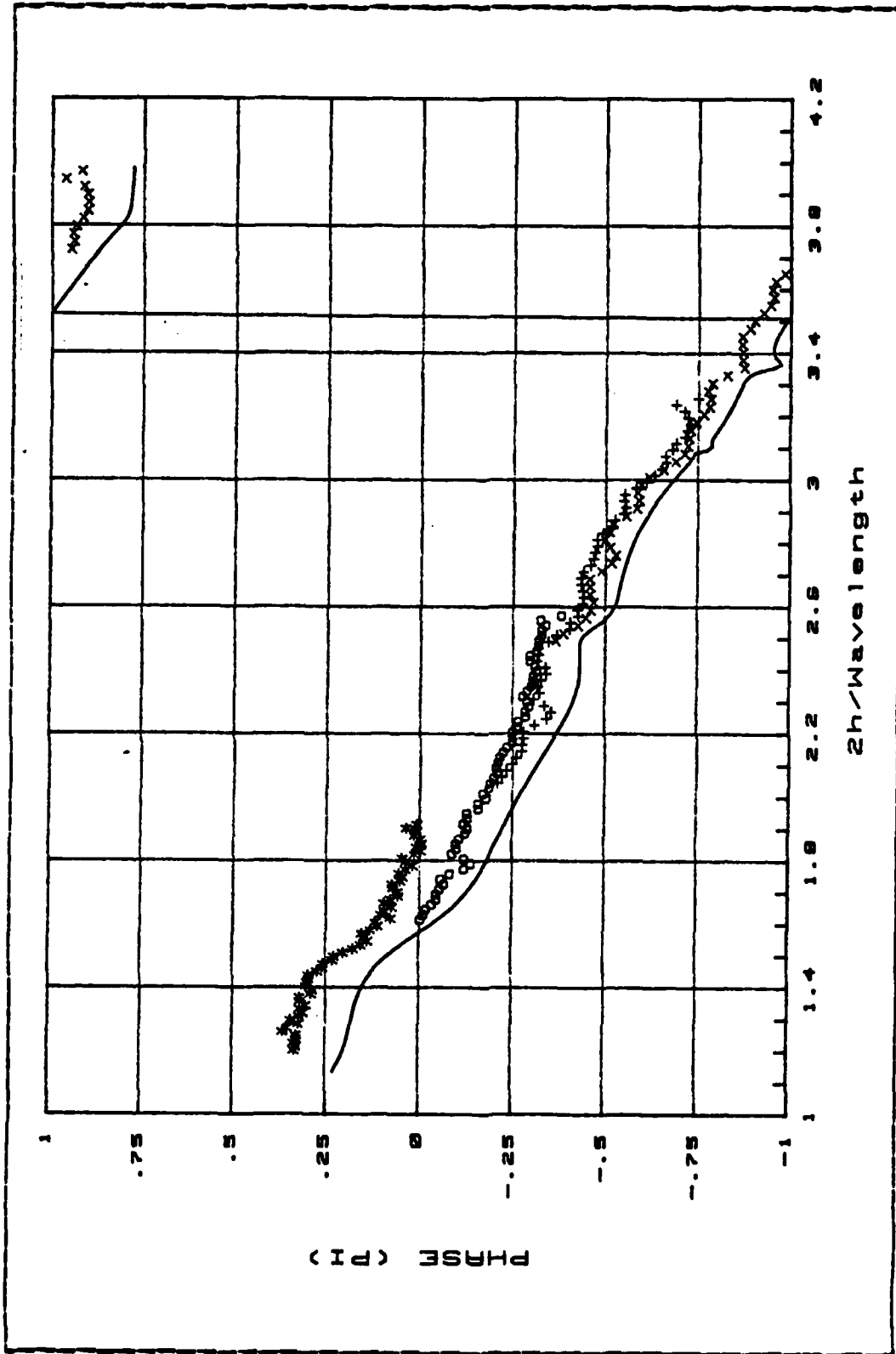


Figure 4.21 Measured Broadside Phase Shift ( $b/a = 4$ ).

### C. CONCLUSIONS

As can be seen from the figures, the measured results vary slightly and not enough to cause the rapid fluctuations over the complete frequency range. Therefore this fluctuation is not caused by the coupling between the cylinder and its support. Experimental and theoretical results show that a small alignment error can not cause this problem either. It appears that the antennas, each capable of cross polarization detection, have lower isolation between feeds. The system calibration standard, a sphere, is not sensitive to the polarization of the output from the transmitting antenna. A cylinder, in the head-on aspect, retains the same symmetry. But for broadside scattering, the change with frequency in the polarization of the incident field will cause problems.

Since the polarization of the output of the transmitting antenna may change with frequency in an unpredictable manner, this effect may introduce the variations observed in the broadside scattering data. Improving the isolation capability of each of the antennas against cross polarization will improve the system performance of the CW step-frequency range.

## V. CONCLUSIONS

The measured scattering data of finite tubular cylinder in head-on and broadside aspects were presented and compared both to the theoretical values and to previously obtained data from slightly longer cylinders.

It is evident that neglecting the wall thickness of the cylinder in the theoretical calculation is a valid approximation. On the other hand, because the waveguide modes depend only on the inner diameter of a finite tubular cylinder, the significant discrepancy between the theoretical values and the old experimental data demonstrates the importance of internal modes on the scattering cross section of a scatterer. Thus, in making the zero wall thickness approximation, the inner radius of the actual cylinder has to be chosen as the radius of the ideal cylinder. With this choice, the thickness of the cylinder is not critical.

Below the  $H_m$  mode cutoff frequency, it can be seen that the locations of maxima and minima of the scattering cross section are determined by the length of the cylinder. A minimum occurs whenever the length of the cylinder equals an integer multiple of one half the wavelength of the incident field. Above the  $H_m$  cutoff frequency, the minima are shifted away from such values. It will require a detailed study of the excited current distributions on the inside and outside surfaces of the cylinder to explain these phenomena.

## LIST OF REFERENCES

1. Bowman, J.J., T. B. A. Senior and P. L. E. Uslenghi, ed. (1969) Electromagnetic and Acoustic Scattering by Simple Shapes. North Holland Publishing Company, Amsterdam.
2. Lee, H. -M., "Double Series Expansion of the Greens Function for a Perfectly Conducting Tubular Cylinder of Finite Length," Radio Science, 18(1), pp. 48 - 56, 1983.
3. Lee, H. -M. "Scattering Theory of the Finite Cylindrical Structure", in preparation.
4. Lee, H. -M., D. Geller, B. Haklay, A. Setiawan and G. P. Chung (1985a), "Back Scattering Cross Section Along the Axis of a Tubular Cylinder of Finite Length," Paper presented at the International Symposium of Antenna and Propagation, Japan at Kyoto, Japan, August 1985.
5. Lee, H. -M., G. P. Chung, D. Geller, B. Haklay (1985b), "The  $H_{11}$  Circular Waveguide Mode and the Back Scattering Cross Section Along the Axis of a Thin Walled Tubular Cylinder of Finite Length," to appear in IEE Proceedings Part H.
6. Mario Iolic, Radar Target Identification Through Electromagnetic Studies, Master Thesis Naval Postgraduate School, Monterey, California, Dec 1984.
7. Boaz Haklay, Broadside Scattering of A Tubular Cylinder for Evaluation of Target Identification, Master Thesis Naval Postgraduate School, Monterey, California, March 1985.
8. David Geller, Head-on Scattering of A Tubular Cylinder of Finite Length For Radar Target Identification Purposes, Master Thesis Naval Postgraduate School, Monterey, California, March 1985.
9. Rome Air Develop Center Tech. AOC Report RADC TDR 64-25 Vol 1 AD 601364 Vol 2 AD 6013365, Radar Reflection Measurements Symposium, April 1964.

### INITIAL DISTRIBUTION LIST

	No.	Copies
1. Library, Code 0142 Naval Postgraduate School Monterey, California 93943-5100		2
2. Defense Technical Information Center Cameron Station Alexandria, Virginia 22304-6145		2
3. Department Chairman, Code 62 Department of Electrical Engineering Naval Postgraduate School Monterey, California 93943-5100		1
4. Prof. Hung-Mou Lee, Code 62 Lh Department of Electrical Engineering Naval Postgraduate School Monterey, California 93943-5100		10
5. Dr. Michael A. Morgan Code 414 Office of Naval Research 800 N. Quincy St. Arlington, Virginia 22217		1
6. Lt. Gyoo-Pil Chung Comm/Elec. Department Navy H/Q Young Deung Po - Gu Seoul 120 Republic of Korea		5

**END**

**FILMED**

---

**1-86**

**DTIC**